The influence of frictional behaviour in the seismogenic zone on large scale deformation in subduction zones: insights from analogue modelling

MSc Thesis

Utrecht University

Job Arts

August 28, 2020

Utrecht University

Department of Earth Sciences

Abstract

Convergent plate boundaries, and in particular the interface between subducting and overriding plates, are responsible for a large quantity of the global seismicity. Deformation at and above the subduction interface can be categorized in different stages, which are part of the so-called subduction seismic cycle. This cycle includes a stress accumulation phase, a seismic event or earthquake, and a subsequent phase of relaxation. An ideal model thus takes tectonic loading, rate dependent friction, and viscoelastic stress relaxation into account.

This study aims at a better understanding of the interaction between frictional behaviour in the seismogenic zone and long term deformation structures. Hence, this study focuses on part of the velocity weakening section of a subduction zone megathrust and the overlying wedge. The approach includes physical analogue modelling of the upper $\sim$10 km of a subduction zone and a quantitative study of frictional behaviour of analogue granular materials at experimental conditions.

Results show the formation of splay faults (linking subduction fault to the surface), frontal thrusts, and backthrusts. The geometry of the accretionary wedge, is determined by the number and the location of faults being (re-)activated. The different models of this study show that loadpoint velocity and frictional properties of the plate interface affect the slip size and size of the force drops. This consequently influences the location of fault (re-)activation and geometry of the accretionary wedge. It therefore implies that overriding wedge geometry could be used to put constraints on the earthquake behaviour at the subduction zone megathrust.

Contents

1 Introduction

Convergent plate boundaries, and in particular the interface between subducting plates and overriding plates, are responsible for a large proportion of the global seismic moment (Scholz, 1990; Pacheco and Sykes, 1992). The observed maximum size of subduction megathrust earthquakes, however, is highly variable worldwide (see figure 1; Brizzi et al., 2018). Although instrumental observation techniques and modelling techniques have improved in recent times, fundamental processes that control the earthquake size and recurrence time are still not well understood. (Brizzi et al., 2020).

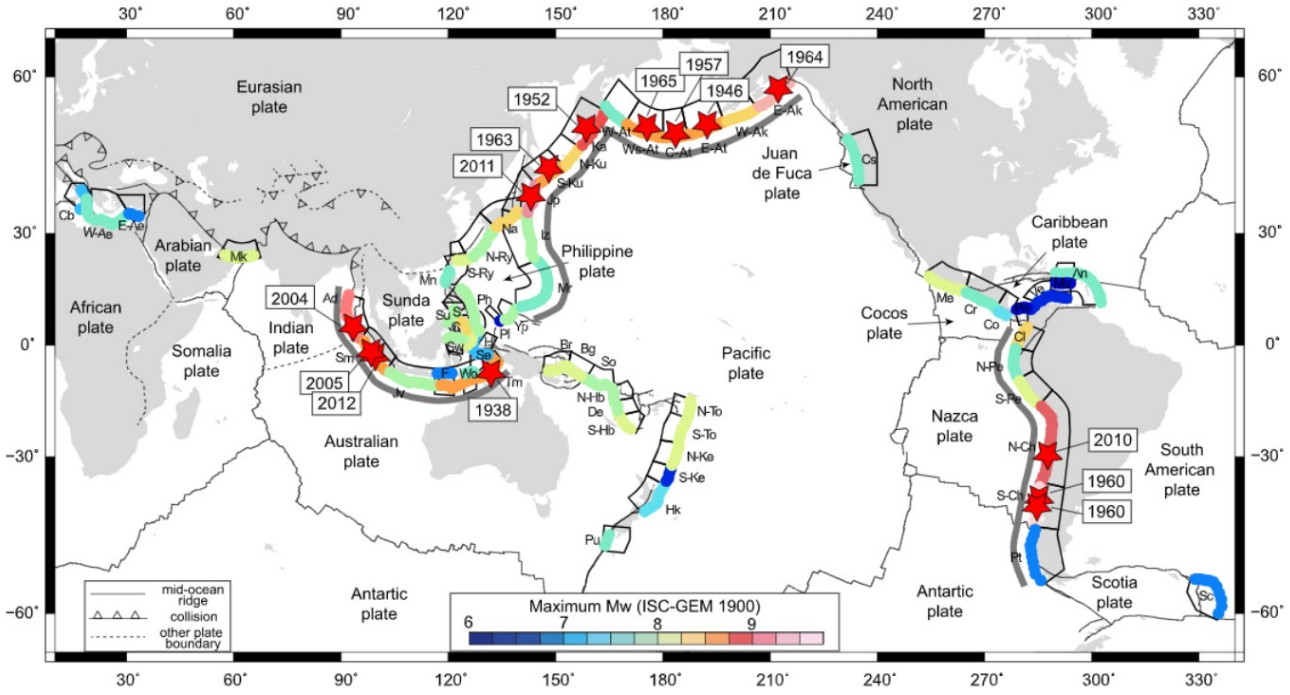

Figure 1: Maximum observed size of megathrust earthquakes according to ISC-GEM 1900 dataset. The black boxes represent sections of subduction zones. Red stars represent recent giant earthquakes ($M_w \geq 8.5$ (Brizzi et al., 2018).

Deformation at the subduction interface and within the overriding plate can be categorized in different stages which are part of the so called subduction seismic cycle (e.g., Wang, 2007). This cycle includes a stress accumulation phase, a seismic event or earthquake and a subsequent phase of relaxation. Afterslip may occur in the shallow part of the megathrust, during the initial postseismic phase (Scholz, 1998). Afterslip may include aftershocks and aseismic slip, depending on the local material properties and the rate of slip (Govers et al., 2018). Another observed phenomenon in most subduction zones is the occurrence of so called 'slow slip events'. Where earthquakes show slip velocities in the order of meters per second and aseismic slip occurs with velocities in the order of millimeters per year, slow slip events show intermediate slip velocities. These events can occur as afterslip, preslip, or during the interseismic period without any clear relation to an earthquake (Schwartz and Rokosky, 2007).

An ideal model of subduction earthquake cycles is able to reproduce all these phenomena, and therefore accounts for tectonic loading, rate dependent friction, and viscoelastic stress relaxation (Wang, 2007). Our knowledge on how these processes influence the geometry of the subduction

zone is limited due to a number of constraints (Corbi et al., 2013): (1) No direct observations on frictional behaviour in the seismic zone can be made; (2) Instrumental seismic records do not go back in time far enough to study the seismic cycle (McCaffrey, 2008); (3) Driving forces, plate boundary fault strength and the link between earthquake cycles and long term deformation are not understood well enough (Wang, 2007).

The aim of this study is to better understand the link between frictional behavior in the seismogenic zone and long term deformation structures in the overlying accretionary wedge. This includes understanding how rate and state friction affects the short term seismic cycle ($< 10^2$ years) and subsequently the deformation at tectonic time scales ($> 10^5$ years). Conversely, it also includes understanding how fault (re-)activation affects frictional behaviour at the subduction zone megathrust. This study focuses on the upper ∼10 km of the continental lithosphere where most internal deformation of the accretionary wedge occurs. The approach includes a detailed quantitative study of frictional behavior of analogue granular materials by springslider experiments and physical analogue modelling of the upper section of a subduction zone. This method has been proven successful in previous studies on deformation and rupture dynamics in subduction earthquake cycles (Rosenau et al., 2009; Corbi et al., 2013; Rosenau et al., 2017).

1.1 Earthquakes and frictional behaviour

Earthquakes originate from sudden displacements along pre-existing faults or plate interfaces. Their behaviour is therefore described as a frictional rather than fracture phenomenon (Scholz, 1998). Based on laboratory observations, Brace and Byerlee (1966) introduced stick-slip frictional instabilities as an earthquake producing mechanisms, where the 'stick' is the interseismic period during which elastic strain accumulates and the 'slip' is the seismic event. Based on experimental studies, constitutive laws of rock friction have been developed to describe stick-slip behaviour. Initial models made a distinction between the static friction coefficient μ_s (ratio of normal stress and shear stress on the slip surface at which sliding starts) and the dynamic friction coefficient μ_d (ratio of normal stress and shear stress during sliding) (Scholz, 1998). Experimental work, however, showed that frictional behaviour of rocks is more complex. The coefficient of friction μ , defined as the shear stress divided by the effective normal stress, evolves with time. If the static contact time t of the contact surface increases, μ increases with the logarithm of t (Dieterich, 1972). When steady state slip occurs at the contact surface, μ evolves, dependent on the logarithm of the sliding velocity V. This dependency can be positive or negative based on rock properties and environmental conditions such as temperature (Scholz, 1998), and the presence of fluids and fault gouge (e.g. Niemeijer and Spiers, 2006). There are several so called 'rate and state' friction laws describing this behaviour. Here we consider the Dieterich-Ruina law, also known as 'slowness' law or 'ageing' law (Scholz, 1998):

$$\tau = \left[\mu_0 + a \ln\left(\frac{V}{V_0}\right) + b \ln\left(\frac{V_0 \theta}{D_c}\right)\right] \overline{\sigma} \tag{1}$$

$$\frac{d\theta}{dt} = 1 - \frac{\theta V}{D_c} \tag{2}$$

Where τ is the shear stress, $\overline{\sigma}$ the effective normal stress, V the slip velocity and V_0 a reference velocity. When $V = V_0$, μ_0 defines the friction coefficient at steady state. a and b are empirical constants. a quantifies the direct rate effect, whereas b is the parameter that describes the evolution or state effect (see figure 2). D_c is the critical slip distance and can be interpreted as the

sliding distance needed to renew the faults contact population. Subsequently, the state variable θ represents the average contact lifetime (Scholz, 1998). The state variable θ evolves with time following equation 2. When contacts are in coupled thermal and mechanical steady state, stable sliding at constant friction occurs. The friction at steady state is given by (Scholz, 1998):

$$\tau = \left[\mu_0 + (a-b)\ln\left(\frac{V}{V_0}\right)\right]\overline{\sigma} \tag{3}$$

This can be rewritten as:

$$(a-b) = \frac{\frac{\tau}{\overline{\sigma}} - \mu_0}{\ln\left(\frac{V}{V_0}\right)} = \frac{d\mu}{\ln\left(\frac{V}{V_0}\right)} \tag{4}$$

The combined (a-b) value is one of the parameters that determines whether a system is stable in terms of friction. This empirical constant depends on a wide range of parameters including slip rate, temperature (Stesky et al., 1974) and the presence of fault gouge (Marone et al., 1990). Frictional stability can be defined as follows: $(a-b) > 0$: velocity-strengthening behaviour, meaning a stable regime. Slips or earthquakes do not nucleate in this regime. Possible propagation of earthquakes will be impeded by strengthening. $(a-b) < 0$: Velocity-weakening behaviour allows the nucleation of slips or earthquakes (see figure 2). At the transition between stable and unstable, there is a conditionally unstable regime which is stable under quasi-static loading, but can become unstable when strong dynamic loading is applied during slip in an adjacent section of the fault (Scholz, 1998). Based on material properties and environmental conditions, the different regimes can be identified for e.g. subduction zones.

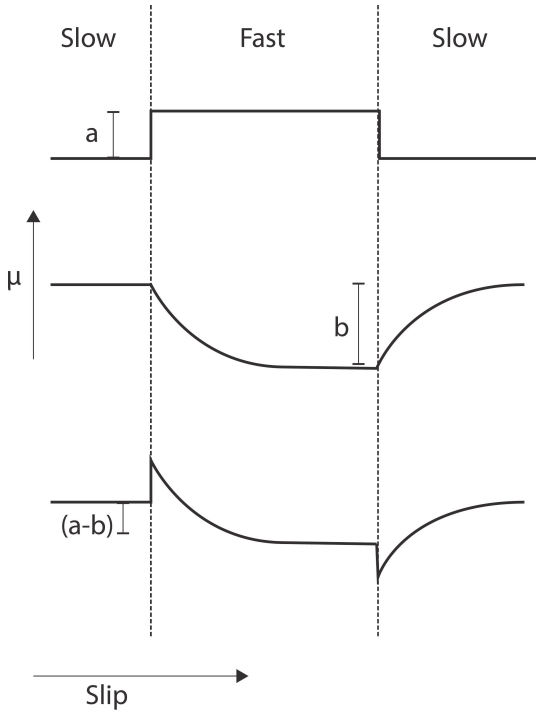

Figure 2: Schematic diagram showing the rate and state dependence of friction μ according to the Dieterich-Ruina law. The diagram shows a velocity stepping test, where the velocity is rapidly increased from 'slow' to 'fast' and back. The upper diagram shows the direct rate dependence a, the middle diagram shows the evolution or state effect b and the lower diagram shows the combined (a-b) value. If $(a-b) < 0$, velocity weakening occurs, allowing the nucleation of slips or earthquakes.

1.2 The subduction zone seismic cycle

Consider a simple 2D model of a subduction zone with an oceanic downgoing plate, overriding plate and an accretionary prism at the plate interface near the Earth's surface (see figure 3). Two transitions between stable and unstable frictional regimes can be identified. The upper transition is believed to be the result of lithification of unconsolidated material. The accretionary prism consists of relatively unconsolidated material resulting in positive (a-b)-values. At greater depth, lithification of this material takes place and (a-b)-values become negative (Marone and Scholz, 1988).The depth at which this transition takes place depends on the thickness of the accretionary prism and is believed to be between ~ 3 and ~ 10 km (Marone and Saffer, 2007; Scholz, 1998).

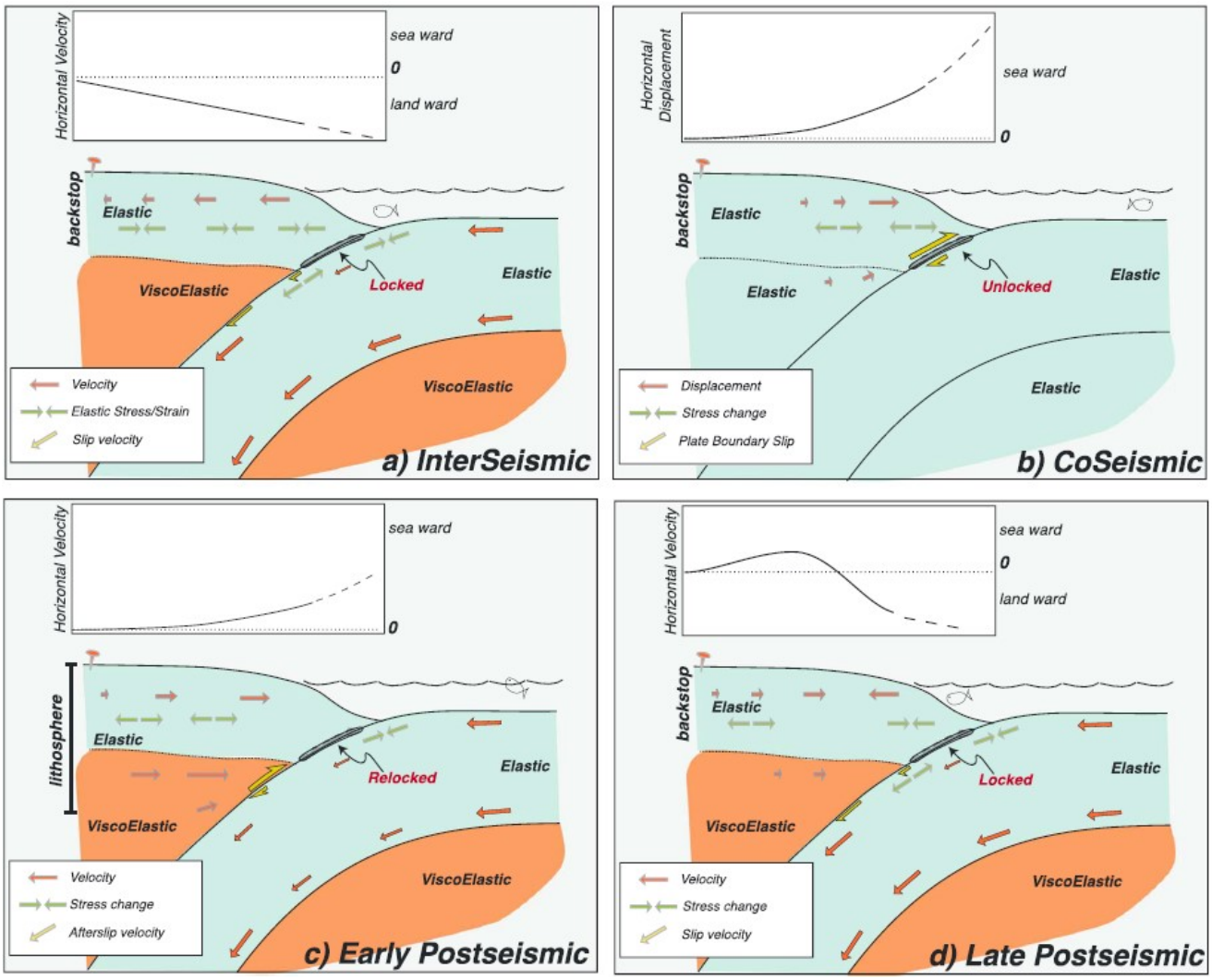

Figure 3: Conceptual model of the stress and deformation history during the subduction seismic cycle, for seismically coupled subduction zones (Govers et al., 2018). (Slip) velocities and stress changes are indicated for (a) the interseismic stage, (b) the coseismic stage, (c) the early postseismic stage, and (d) the late postseismic stage. Horizontal velocities of the overriding wedge are indicated in the white diagrams. The predominant type of behaviour of the rocks surrounding the subduction megathrust is indicated by different colours: orange: visco-elastic behaviour and green: elastic behaviour. For further description, see text. Note that slow slip events are not illustrated in this conceptual model.

The lower transition coincides with the operation of crystal plastic processes such as dislocation and diffusion creep. Due to the low temperature of the downgoing plate, this transition occurs at relatively large depths. The mineral content of the predominantly basaltic downgoing plate requires higher temperatures to become viscous, which consequently amplifies this effect. Therefore the transition to a stable regime can occur at depths up to ~ 45 km (Scholz, 1998). When a large earthquake occurs, it can propagate through part of the lower transition until it terminates. It can also propagate through the upper transition, where it might reaches the Earth's surface. Whether it will propagate all the way to the surface, depends on the width of the accretionary prism and the size of the earthquake (Scholz, 1998). This, of course, has great implications for tsunami-genesis.

The percentage of plate convergence associated with earthquakes can be quantified by the seismic coupling coefficient, which is defined as the ratio between slip rate determined from earthquakes and the total slip rate (seismic + aseismic) (Pacheco et al., 1993). Seismically coupled subduction zones show long time intervals between earthquakes, during which stress is building up. Based on geological and geodetic observations we can distinguish between different stages in the seismic cycle for seismically coupled subduction zones (Scholz, 1998). During the interseismic period (figure 3a), the subduction zone is locked at its unstable section. At greater depth, ongoing subduction by steady slip causes loading and stress build up (Scholz, 1998). GPS data shows that this is often reflected by a landward motion (elastic compression) of coastal areas of the overriding plate (Wang, 2007). In the nucleation phase, prior to the earthquake, slip starts to accelerate, sometimes associated with fore-shocks. Eventually, the instability leads to an earthquake or co-seismic phase (figure 3b). During this phase, slip not only occurs in the unstable regimes, but also penetrates in the stable zones causing stress build up below the lower transition (Scholz, 1998). At this stage all rocks surrounding the subduction zone behave in an elastic way (Govers et al., 2018). GPS-data shows a seaward motion of the overriding wedge, known as the elastic rebound. During the postseismic phase, this stress is slowly released, decaying exponentially with time. This relaxation phase can take from a couple of years up to a decade. Both beneath and above the seismogenic zone, afterslip can occur during the postseismic phase (Scholz, 2019). Based on surface displacements obtained from GPS data, one can distinguish between the early postseismic phase in which only seaward motions of the overriding wedge are observed, and a late postseismic phase in which locking of the seismogenic zone becomes apparent as landward motions near the trench (figure 3c and d). As mentioned in the introduction, slow slip events might occur as afterslip, preslip, or during the interseismic period without any clear relation to an earthquake (Schwartz and Rokosky, 2007).

1.3 Dynamics of subduction wedges

The theory of critically tapered Coulomb wedges has been used successfully to explain deformation in accretionary wedges at convergent plate boundaries (Davis et al., 1983; Dahlen, 1984; Wang and Hu, 2006). This theory, however, requires the assumption that the wedge is in a constant critical state and therefore constantly on the verge of failure. This could be true for subduction zones where only aseismic slip occurs, which is rather rare (Wang and Hu, 2006). The critically tapered coulomb wedge therefore represents one endmember in which slip at the fault contact takes place at constant shear stress. The other endmember is a scenario in which the fault is completely locked in the interseismic phase and slip only occurs during the coseismic phase (Wang and Hu, 2006). The kinematics for most subduction zones lie somewhere between the two end-members and can very over time. Fluctuations of basal stress throughout seismic cycles imply that the wedge cannot always be in a critical state. It is therefore important to consider the mechanics of a stable wedge

as well (Wang and Hu, 2006).

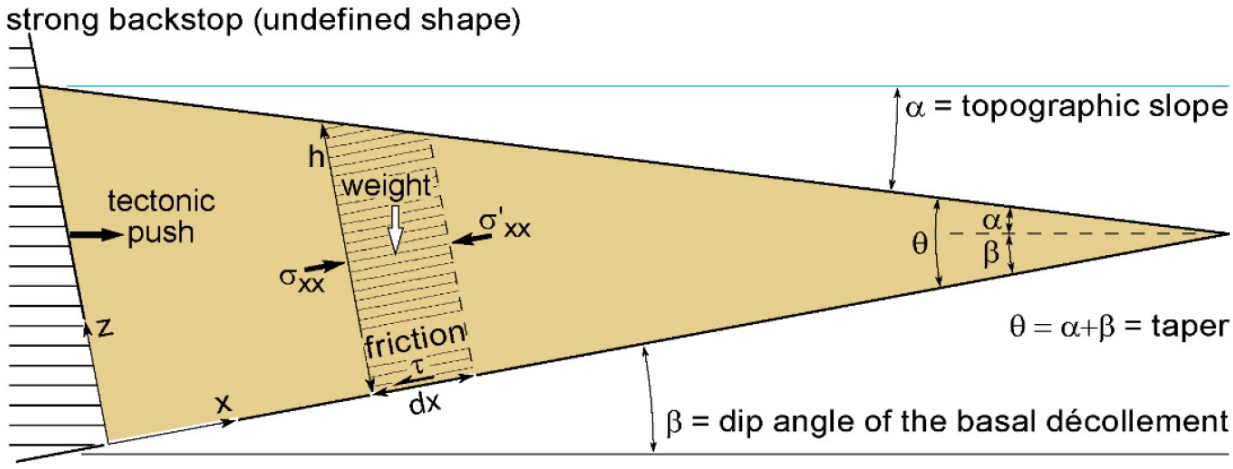

Figure 4: Geometry and important parameters of non-cohesive accretionary wedge model (Burg, 2016)

First, a simple non-cohesive critical taper wedge model based on Dahlen (1984, 1990) is considered. The surface of the wedge is assumed to be planar and has an angle α with the horizontal (see figure 4). The material in the wedge is uniform and has a density ρ. We ignore the the pore fluid pressure and the weight of the overlying column of air or water for that matter. Together, the angle with the basal plane β and the surface slope α form the taper angle θ . A Cartesian coordinate system is chosen, with the x-axis along the basal plane and the z-axis perpendicular to it. A small section of the wedge between x and $x + dx$ is considered (see figure 4). At static equilibrium, the gravitational force as x-component per body length is given by (Dahlen, 1990):

$$F_g = -\rho g z \sin(\beta) dx \tag{5}$$

Where g is the gravitational acceleration and z the local thickness of the wedge. The compressive force acting perpendicular on the side boundaries (x and $x + dx$) of the considered section is given by (Scholz, 1990):

$$F_c = \int_0^z \left[\sigma_{xx}(x, z) - \sigma_{xx}(x + dx, z)\right] \tag{6}$$

Finally, there is a force acting on the base of our small section, resulting form gravity and compression from the rear of the wedge. This force is given in terms of shear stress τ and normal stress σ_n acting on the basal surface (Dahlen, 1990):

$$F_b = (\tau + \sigma_n \sin\theta)\, dx \tag{7}$$

It is assumed that sliding over the base is governed by frictional sliding without cohesion, for simplification:

$$\tau = \mu_b \sigma_n \tag{8}$$

Where μ_b is the coefficient of friction at the base. Substituting equation 8 in equation 7 reduces the basal force to:

$$F_b = \sigma_n \left(\mu_b + \sin\theta\right) dx \tag{9}$$

Balancing the forces in equilibrium gives (Dahlen, 1990):

$$F_g + F_c + F_b = 0 \tag{10}$$

Where F_g and F_c both act in the positive x direction and F_b acts in the opposite direction. By substituting equation 5, 6, and 7 in the force balance and taking the limit as $dx \to 0$, an exact solution can be obtained:

$$\frac{d}{dx}\int_0^z \sigma_{xx} dz = -\left[\rho g z . \sin\beta + \sigma_n(\mu_{base} + \sin\theta)\right] \tag{11}$$

For small angles α and β a number of approximations can be employed to simplify this equations (Dahlen, 1990). These approximations include: $\sin\alpha \approx \alpha$, $\sin\theta \approx \theta$, $\cos\theta \approx 1$, $\sigma_n \approx \rho g z$. This reduces equation 11 to:

$$\frac{d}{dx}\int_0^z \sigma_{xx} dz = -\rho g z(\mu_{base} + \beta) \tag{12}$$

For non-cohesive dry sand, the failure criterion can be written as (Jaeger et al., 1979):

$$\frac{\sigma_1}{\sigma_3} = \frac{1+\sin\phi}{1-\sin\phi} \tag{13}$$

Where σ_1 and σ_3 are the maximum and minimum principal stress respectively (also see the material section below). For narrow tapers at rest, it is assumed that the principle stresses are approximately horizontal and vertical:

$$\sigma_{zz} \approx \sigma_3 \approx -\rho g z \tag{14}$$

and

$$\sigma_{xx} \approx \sigma_1 \approx -\left(\frac{1+\sin\phi}{1-\sin\phi}\right)\rho g z \tag{15}$$

If we assume that $dz/dx \approx \theta$, the traction on the sidewalls in equation 12 simplifies in this approximation to (Dahlen, 1990):

$$\frac{d}{dx}\int_0^z \sigma_{xx} dz = -\rho g z \left(\frac{1+\sin\phi}{1-\sin\phi}\right)\theta \tag{16}$$

Now we can insert equation 16 into equation 17:

$$\theta \approx \left(\frac{1-\sin\phi}{1+\sin\phi}\right)(\beta + \mu_b) \tag{17}$$

This way, an equation is obtained which relates the critical taper angle θ to the angle of internal friction ϕ, and the friction coefficient at the base of the accretionary wedge μ_b.

Note that this simplified relation only applies to non-cohesive wedges, without the presence of pore fluids, and which are in a critical state (i.e. everywhere on the verge of failure). This end-member does not take into account the cyclic stress changes associated with the seismic cycle (Wang and Hu, 2006). It does, however, provide a first order explanation of the geometry of accretionary wedges.

2 Experimental Approach

As mentioned in the introduction, an ideal model of subduction earthquake cycles accounts for tectonic loading, rate dependent friction, and viscoelastic stress relaxation. Most existing models, however, can be subdivided into two groups: 1) Short term (visco-) elastic models. These models focus on the seismic behaviour and assume that the long time scale deformation is superimposed on the seismic cycles. These studies do not include the effect of tectonic processes on the seismic behaviour of the subduction zone (Rosenau et al., 2009; Wang, 2007). 2) Long term plastic models, on the other hand, focus on studying the tectonic evolution and do not take into account the effect of cyclic stress changes due to earthquakes (Rosenau et al., 2009). Bridging the temporal and spatial time scales is complex due to the high non-linearity of processes such as stress loading and relaxation (Wang, 2007) and frictional behaviour (Scholz, 1998). An additional challenge is the resolution of the model: The large spatial and temporal variation in deformation processes requires a model which is large enough in scale to interpret it (Rosenau et al., 2009). Recent analogue studies have been successful in modelling subduction zone earthquakes. These studies include elastoplastic granular wedge set-ups to simulate the subduction megathrust seismotectonic evolution (e.g. Rosenau et al., 2009, 2010), and the Viscoelastic gelatine wedge set-up to study the subduction interplate seismic cycle (Corbi et al., 2013). The models in these studies represent the upper ∼75 km of the subduction megathrust fault and therefore include both the upper and lower transition between velocity weakening and velocity strengthening.

In this study we focus on the influence of frictional behaviour in the seismogenic zone, on the large scale deformation in the wedge above it. Therefore, only the velocity-weakening section of a subduction zone and the overlying wedge is modelled. The transition which coincides with the operation of crystal plastic processes is not considered. This of course results in a simplified model which can not take into account the visco-elastic stress relaxation. However it is believed to be a useful experimental approach to test the plastic and elastic effects during cyclic loading and unloading of the wedge as a result of the earthquake cycle. Our experimental approach involves a detailed quantitative study of frictional behavior of analogue granular materials by conducting springslider experiments. The findings of this frictional property analysis are used for designing a subduction zone earthquake model.

2.1 Springslider experiments

Only a few studies (e.g. Klinkmüller et al., 2016; Rosenau et al., 2016) have performed ring shear tests on granular materials to determine their frictional properties under the very low normal loads operating in analogue models (< 10 kPa). Here we use simple springslider experiments to analyse the frictional behaviour of granular materials, under experimental conditions. The experimental setup (figure 5) consists of a Plexiglass box (8 cm long, 6.8 cm wide and 8 cm high) which is pulled by a rope, connected to a motor. The bottom contact area of the plexiglass walls are covered by a Teflon sheet to reduce the effect of friction caused by the plexiglass box. The loading velocity exerted by the motor is controlled by a gearbox. A tension loadcell is placed between the plexiglass box and the rope to measure the pulling force. By performing a parametric study, the influence of the following variables on the frictional behaviour is tested: Type of material (quartz, feldspar, plastic sand and salt), type of decollement (plastic sheet, sandpaper and glued granular materials), normal load, loading velocity, and spring constant. An overview of the parametric study is shown in table 1. To test the effect of spring constant k, we added different springs between the loadcell and the rope. Spring constants are determined by suspending different known loads from the spring

and by measuring the change in length of the spring x. The spring constant is then calculated based on Hooke's law (1660), which states that the applied force F_p equals the change in length x, multiplied by the spring constant k:

$$F_p = kx \tag{18}$$

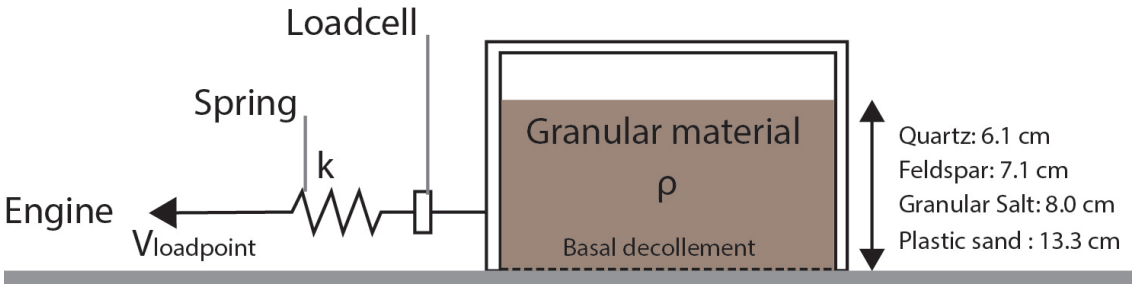

Figure 5: Springslider experimental set-up with tested parameters: loadpoint velocity, spring constant, type of granular material and type of basal contact. Note that the thickness of the layer of granular material depends on the density of the material, in order to keep the normal loads equal for all experiments.

2.2 Subduction zone earthquake model

The subduction zone earthquake model setup (figure 6) consists of a wooden downgoing plate with a length of 80 cm and a width of 13 cm. This plate is placed on top of rollers in order to keep external friction as low as possible. The downgoing plate is confined between plexiglass walls and can therefore only move towards the motor. To reduce friction with the plexiglass walls, a thin layer of felt is placed on both sides of the downgoing plate. Hence, gravitational forces are enough to move the plate when a small vertical load is exerted. A vertical, plexiglass backstop is fixed in order to confine a wedge of granular material on top of the downgoing plate. The lower boundary of the backstop is placed 5 mm above the downgoing plate in order to allow part of the granular material to move underneath it, together with the downgoing plate. This boundary condition forces the development of a decollement within the wedge rather than at the base. The wedge of granular material has a maximum thickness at the backstop. In order to keep the initial normal load at the plate interface as a constant, the maximum thickness of the wedge varies, depending on the bulk density of the granular material. The bulk density depends on e.g. the method of emplacement (Krantz, 1991). Therefore, in all experiments the material is placed by sieving with a 355 μm sieve. The granular material in the wedge is homogeneous in terms of physical properties. However, to visualize structure development, layers of different colour are used.

A motor pulls with a constant loading velocity on small wooden trolley, which is connected to the large downgoing plate by a number of springs. This allows the build-up of elastic strain between the pulley and the downgoing plate. The springs therefore represent elastic behaviour at the transition between velocity weakening and velocity strengthening, which undergoes extension during the interseismic stage and shortening during the seismic event (Govers et al., 2018). In that context, the wooden trolley represents part of the downgoing plate at the velocity strengthening section of the subduction megathrust, which moves aseismically. Note that the transition zone of the natural prototype also shows frictional or viscous behaviour which is not accounted for in this loading mechanism. The elasticity of the transition zone in the model can be modified by using

springs with different spring constants or changing the amount of springs in parallel:

$$k_{eff} = k_1 + k_2 + ... + k_n \tag{19}$$

Where k_{eff} is the effective spring constant. If the force exerted on one of the springs is known, the total pulling force exerted on the large downgoing plate of the model can be calculated:

$$F_p = F_{lc}\frac{k_{eff}}{k_{lc}} \tag{20}$$

Where F_p is the total pulling force (N), F_{lc} the pulling force (N) exerted on the spring connected to the loadcell, and k_{lc} the spring constant of the spring connected to the loadcell. Forces measured by the loadcell are transferred into a digital signal as described in the monitoring and result analysis section. In addition, a displacement sensor is connected to the rear of the downgoing plate, to measure accumulative displacement and coseismic slip velocities.

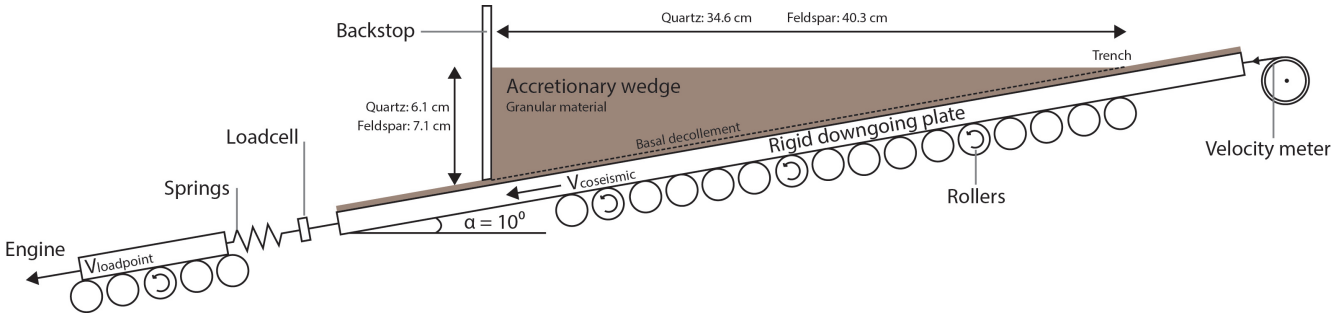

Figure 6: Subduction zone megathrust model set-up. Note that the maximum thickness of the wedge, and consequently its length depends on the bulk density of the granular material in order to keep normal loads at the basal decollement equal.

2.3 Model scaling

Scaling of models to their natural prototype is based on the theory of dynamic similarity, first described by Galileo Galilei (1638). This theory was later applied to physical analogue models of the Earth, taking into account geometric (structures), kinematic (motions) and dynamic (driving fores) similarity (Hubbert, 1937). The first two meet the principles of similarity if the model size and deformation velocity are scaled to nature accordingly (Rosenau et al., 2009). Dynamic similarity requires that the different forces in the model have the same ratios as in the natural prototype. (Rosenau et al., 2009). For the ratio of stresses this means (Brun, 2002):

$$\sigma^* = \rho^* g^* L^* \tag{21}$$

Where * refers to the ratio between model and natural prototype, σ the stress, ρ the density, L the length and g the gravitational acceleration. The latter is equal for the natural example and the scaled model and therefore has a ratio of $g^* = 1$. Since the ratio between gravitational acceleration is equal to 1 and the density difference between natural prototype and analogue material is in the same order of magnitude, the ratio of stresses scales approximately to the ratio of lengths Brun (2002):

$$\sigma^* \approx L^* \tag{22}$$

The Cauchy number Ca is a dimensionless number which relates the elastic forces and inertia (Rosenau et al., 2009):

$$Ca = \frac{\rho v^2}{k} \tag{23}$$

Where v is the local velocity, and k the bulk modulus of the medium, which is a measure for the compressibility of the material. Dynamic similarity requires that the the Cauchy number and its constituents are scaled correctly between natural prototype and scale model (Rosenau et al., 2009):

$$k^* = \rho^* \frac{(l^*)^2}{(t^*)^2} \tag{24}$$

Where l is the length and t is the time.

In the subduction zone models we use quartz sand and feldspar sand with densities of 1510 kg/m^3 and 1300 kg/m^3 respectively (Willingshofer et al., 2005). In nature the accretionary wedge above the subduction megathrust has a density in the order of 2500 kg/m^3 (e.g. Ujiie and Kimura, 2014; Platt et al., 1985; Dahlen et al., 1984). Therefore a density scaling factor of $\rho^* = 0.56$ applies. The models represent the upper 10 km of the lithosphere. Models consisting of a quartz wedge have a maximum thickness of 6.6 cm and a resulting length scale ratio of $l^* = 6.6 * 10^{-6}$. Models with granular feldspar have a maximum thickness of 7.6 cm and therefore a length scale ratio of $l^* = 7.6 * 10^{-6}$. Accordingly, the material in the model has to be weaker with a scaling factor of $\sigma^* = 4.0 * 10^{-6}$. Brittle strength is controlled by the cohesion C and the internal friction coefficient μ. The latter is dimensionless and the cohesion has the same unit as the strength (Pa) and therefore has the same scaling factor: $C^* = 4.0 * 10^{-6}$ (Rosenau et al., 2009). The same scaling factor also applies to the bulk modulus:$k^* = 4.0 * 10^{-6}$. From the Cauchy number and the scaling relationship follows that the scaling factor for coseismic time is given by $t_c^* = 2.5 * 10^{-3}$, if we assume that during the coseismic phase, deformation is predominantly elastic (Wang, 2007). This means that 0.01 s coseismic rupture time in the model represents approximately 4.0 seconds in nature. The interseismic period is highly variable and differs between various subduction zones. If we assume a recurrence time of 100 - 200 years (Kodaira et al., 2000) and we use the same time scale as for the coseismic phase, the interseismic phase would take more than 4 months in the model. However, since inertial forces do not play an important role in the slow tectonic processes during the interseismic phase, a different time scale can be applied (Rosenau et al., 2009; Corbi et al., 2013). Here we use an interseismic time scale of: $t_i^* = 3.3 * 10^{-8}$ such that 100 s in the model is 100 years in nature.

2.4 Materials

The subduction zone models consist of a homogeneous wedge of granular material. Materials tested in the springslider include quartz sand (PURESIL® MAM1ST300, Sibelco), feldspar (Feldspar FS 900 S, Amberger Koalinwerke), plastic sand (Enduro-Grade EG5, Maxiblast inc) and granular salt (MARSEL(R) 0-0.2, Zoutman). The material properties of quartz, feldspar and plastic sand have been measured at GFZ Potsdam by using a Schulze ring shear tester RST-01.pc and by velocity stepping tests at variable normal load and variable shear rate (Willingshofer et al., 2005, 2018). This study includes a quantitative analysis of the frictional properties of the materials under normal loads used in subduction experiments of this study (see results section). In the subduction zone models we distinguish between the megathrust fault (the zone that forms the boundary between overriding wedge and downgoing plate) and the medium of the overriding wedge. The megathrust

fault is a pre-existing structure which is reactivated during the coseismic phase. Its behaviour can therefore be explained by frictional properties (Scholz, 1998). Deformation in the medium of the overriding wedge is elastic (reversible) and/or brittle (irreversible).

2.4.1 Frictional behaviour

Frictional behaviour at the megathrust is described by rate and state friction laws (see section 1.1; Scholz, 1998). Rate dependencies of the quartz, feldspar and plastic sand (Willingshofer et al., 2005, 2018), as well as granular salt (Rosenau et al., 2017) have been determined at GFZ Potsdam, by performing velocity stepping tests under a constant normal load of 2000 Pa. All four granular materials show velocity weakening at the testing conditions. Normal loads and boundary conditions in this study, however, differ slightly. Therefore it is of importance to perform springslider experiments to test frictional stability at the experimental conditions of this study. Springslider experiments are designed to represent experimental conditions of the subduction zone earthquake model, at the location of the backstop. At this location, the wedge has the largest initial thickness and the normal load has a value of 910 Pa at the level of the decollement. The top of the subduction zone earthquake model has an open boundary, whereas velocity stepping tests performed at GFZ Potsdam require the confinement of granular material at all boundaries.

2.4.2 Brittle behaviour

The irreversible deformation of the overriding wedge is an analogue for brittle deformation in the crust. Based on experimental work, Byerlee (1978) found that brittle deformation of rocks occurs according to the Mohr-Coulomb criterion (Coulomb, 1776; Mohr, 1900):

$$\tau = C + (\tan \Phi)\sigma \tag{25}$$

Where τ is the shear stress, C the cohesion, σ_N the the normal stress, and Φ the angle of internal friction. Typical values for the cohesion of natural crustal rocks are in the order of 5 - 50 MPa (Byerlee, 1978; Brun, 1999; Dahlen et al., 1984) and the typical angle of internal friction is 30° (Byerlee, 1978; Brun, 1999). From the scaling relationship follows that the cohesion in the model should range between 20 - 200 Pa, which is in the same order of magnitude as the cohesions measured in ring shear tests at GFZ Potsdam (Willingshofer et al., 2005, 2018). From the geometry of a developing fault, the following relations can be obtained:

$$\sigma_f = \frac{\sigma_1 + \sigma_3}{2} + \frac{\sigma_1 - \sigma_3}{2} \cos 2\theta \tag{26}$$

$$\tau_f = \frac{\sigma_1 - \sigma_3}{2} \sin 2\theta \tag{27}$$

$$2\theta = \frac{\pi}{2} + \Phi \tag{28}$$

$$\tau_f = \sigma_f \tan \Phi \tag{29}$$

Where σ_f is the normal stress on the fault, τ_f the shear stress on the fault, σ_1 and σ_3 the maximum and minimum principle stress respectively. The angle of internal friction Φ is related to the coefficient of friction μ by:

$$\mu = \tan \Phi \tag{30}$$

A relation between the maximal and minimal stress can be obtained from the equations above (Jaeger et al., 1979):

$$\sigma_3 = -\frac{\sin\Phi - 1}{\sin\Phi + 1}\sigma_1 \tag{31}$$

If we assume that the brittle layer is homogeneous in density, the vertical stress σ_v is given by (Brun, 2002):

$$\sigma_v = \rho g Z_b \tag{32}$$

Where ρ is the density of the brittle layer, g the gravitational acceleration and Z_b the depth or thickness of overlying column of rock (or granular material). If no external force is applied (initial stage of the model) the minimal principle stress in compression is equal to the vertical stress: $\sigma_3 = \sigma_v$. If we substitute this in the equation above and fill in a typical value of $\Phi = 30^\circ$ we get the initial maximum principle stress:

$$\sigma_1 - \sigma_3 = 2\rho g Z_b \tag{33}$$

Equation (33) shows a linear relation between the strength of a brittle layer and the thickness of the layer. In the subduction wedge models, the initial strength of the wedge at the depth of the decollement decreases towards the tip (see figure 7).

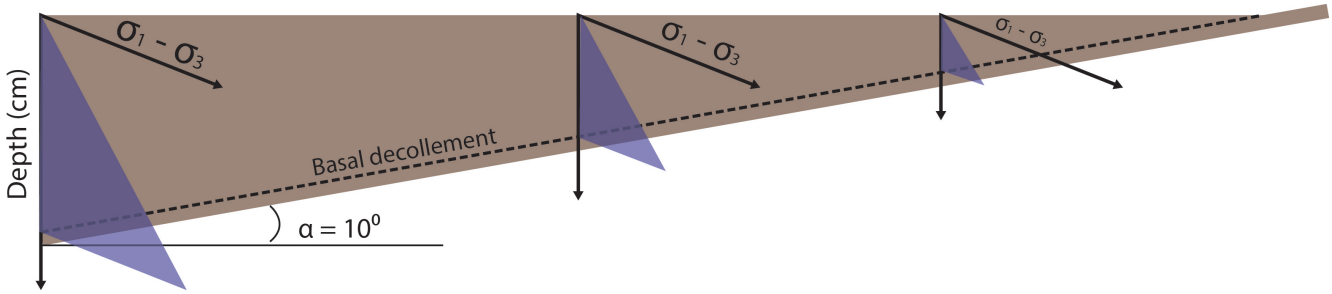

Figure 7: Brittle internal strength of the undeformed wedge. Coloured triangles indicate how differential stress changes with depth. Note that the differential stress at depth of the basal decollement decreases towards the tip of the wedge.

2.4.3 Elastic behaviour

The elastic behaviour of quartz has been tested by Klinkmüller et al. (2016). The Bulk moduli of all tested samples in this study range between 632 and 1829 MPa which is 1-2 orders of magnitude lower than natural rocks. If the appropriate scaling factor is applied, the bulk modulus of the analogue materials should be 6 orders of magnitude smaller (0.1 MPa). Rosenau et al. (2009) has shown that the mixing of a granular material with rubber pallets can lower the elastic moduli. These rubber pellets (Melos EPDM-Granules 0.5-1.5 mm) have linear elastic behaviour for low strains and have a bulk modules of 0.1 MPa. In mixtures with other granular material, the behaviour becomes predominantly elastic when more than 50% of the bulk consists of rubber pallets (Rosenau et al., 2009).

2.5 Monitoring and result analysis

Monitoring of permanent deformation in the model is performed by using two digital cameras, making both top view and side view images of the model. Digital images are taken before and

after individual slips in order to obtain displacements of single events. Therefore the frequency varies between different models, depending on the slip recurrence times. Top view images are analyzed by performing digital particle image velocimetry in PIVlab (Thielicke and Stamhuis, 2014). Direct Fourier transform correlation with multiple passes and deforming windows is used to obtain particle motions between successive images and resultant displacement vector fields. From surface displacement vector fields, 1D coseismic slip displacements over a line transect (running from backstop to opposite model boundary) are calculated (see appendix F).

Seismic behaviour of the model is derived from cyclic variations in loading force and slip displacement. Loading forces are measured by a loadcell of type Omegadyne LCMFL-20N subminiature. The loadcell can measure forces up to 20 N. The force is converted to a voltage, which is displayed on a strain gauge panel meter (Omega DP25B). The loadcell was calibrated by suspending known weights under the loadcell and by plotting the resulting force against the voltage output (see appendix H). The analogue signal of the loadcell is sent to a TiePie Handyscope HS5-530XM digital oscilloscope which converts it to a digital signal with a 16 bit digital resolution. TiePie Multi Channel software is used to process and display the force data. The acquired data is exported as CSV-files containing time data (in seconds) and force data (in volt). A Python script is used to convert voltages to pulling force.

A displacement sensor, consisting of a wire on a spool connected to a potentiometer(in house built at Utrecht University), is attached to the rear of the downgoing plate, to measure accumulative displacement. The analogue signal is converted to a digital signal in a similar way as the force. The acquired data is exported as CSV-files containing time data (in seconds) and displacement data (in volt). A Python script is used to convert voltages into displacement and to calculate coseismic slip velocities.

3 Results

3.1 Springslider experiments

The influence of a range of parameters on the frictional behaviour at experimental conditions is tested, including: Type of granular material, loadpoint velocity, type of basal contact, and spring stiffness. In this section, results are shown for springslider experiments with a constant spring stiffness. The frictional behaviour of quartz sand, feldspar sand, plastic sand and granular salt are tested at different loadpoint velocities (1.0, 2.0 and 4.0 cm/h respectively) and at different basal contacts (plastic sheet, unconsolidated granular material, and granular material glued to a plastic sheet). An overview of the experiments is shown in table 1. A standard notation is used to refer to specific experiments, where the first term denotes 'springslider experiment', the second term the type of granular material, the third term the loadpoint velocity and the fourth term the type of basal contact (example: sp-Qtz-1-ps). A selection of the results is shown in figure 8.

3.1.1 Basal contact dependence

Experiments performed with a plastic sheet as basal contact show very regular stick-slips for every type of granular material at all three loadpoint velocities. Friction coefficients for all materials are very small < 0.4. Peak friction for granular salt (sp-Sal-1-ps) is relatively small with respect to the other materials, whereas that of plastic sand (sp-Pls-1-ps) is relatively high (see figure 8C).

Experiments performed with granular material glued to a plastic sheet are on the other end of

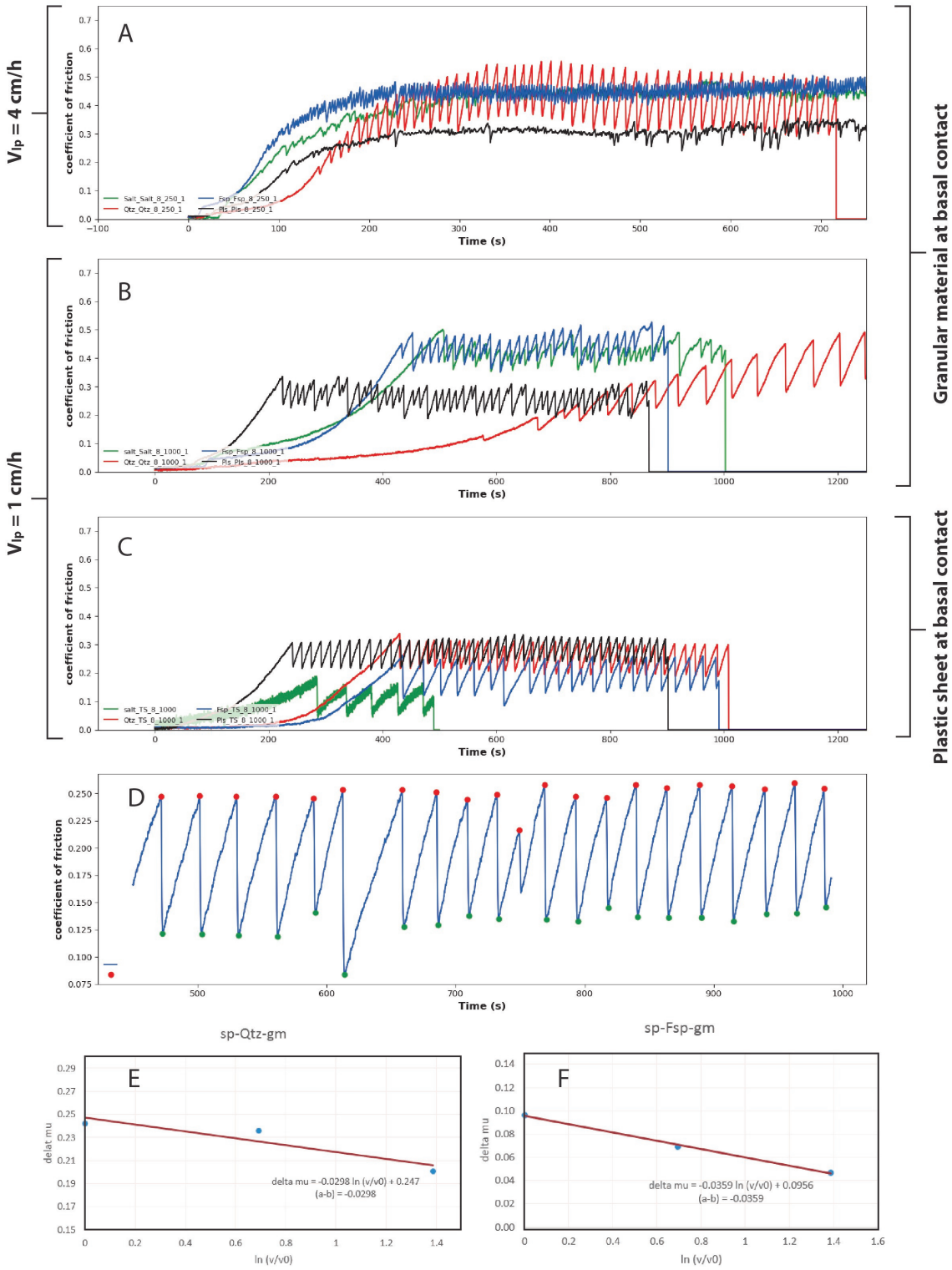

Figure 8: Results of spring slider experiments, showing frictional behaviour of granular materials at (A) $V_{loadpoint} = 4cm/hr$ and granular material at the base, (B) $V_{loadpoint} = 1cm/hr$ and granular material at the base, (C) $V_{loadpoint} = 1cm/hr$ and plastic sheet at the base. The type of granular material is indicated by colours: green = granular salt, red = quartz sand, blue = feldspar sand, and black = plastic sand (D) Identification of peaks and valleys for a representative time interval. (E and F) Linear regression in friction coefficient as function of loadpoint velocity, to obtain (a-b)-values.

	$Loadpointvelocity(cm/hr)$		
Material	1.0	2.0	4.0
Quartz sand	sp-Qtz-1	sp-Qtz-2	sp-Qtz-4
Feldspar sand	sp-Fsp-1	sp-Fsp-2	sp-Fsp-4
Plastic sand	sp-Pls-1	sp-Pls-2	sp-Pls-4
Salt	sp-Sal-1	sp-Sal-2	sp-Sal-4

Table 1: Overview of springslider experiments. 'sp' denotes springslider, the second term denotes the granular material tested and the third term denotes the loadpoint velocity in cm/h. In addition, for every combination of material and loadpoint velocity, different basal materials are tested, including plastic sheet (ps), a 1cm thick layer of unconsolidated granular material (gm), and the same granular material glued to a sheet (gl).

the spectrum and show highly variable behaviour for all materials at all three loadpoint velocities. Only granular quartz (sp-Qtz-1-gl) shows relatively regular stick-slips at low loadpoint velocity. Plastic sand shows stable sliding rather than unstable behaviour, although the friction coefficient varies with time and a drop in friction occurs occasionally. Feldspar sand and granular salt show variable behaviour in both size of the friction drops and height of peak friction.

Unconsolidated granular material as basal contact results in relatively regular stick slips for quartz sand and feldspar sand, whereas granular salt and plastic sand show significant variations in friction drop size and peak friction. This effect is amplified at large loadpoint velocities (see figure 8A and B). Plastic sand (sp-Pls-4-gr) shows stable sliding at a relatively low friction coefficient, with occasionally a large drop in friction. Peak friction coefficients for feldspar and quartz sand are similar, whereas size of the friction drop is larger for quartz sand at all velocities (see figure 8A and B).

3.1.2 Loadpoint velocity dependence

For all types of basal contacts, the following trends are observed: decreasing the loadpoint velocity leads to an increase in size of friction drops and an increase in recurrence time. Granular salt and plastic show more variations in behaviour when the loadpoint velocity is increased. In the latter case, unstable behaviour shifts towards stable sliding when the loadpoint velocity is increased.

(a-b)-values are determined for all four granular materials, in the case of a plastic sheet as basal contact and in the case of unconsolidated granular material at the basal contact, to give quantitative insights in the frictional behaviour. Peak and valley values in coefficient of friction are identified for a representative time interval (See example figure 8D). Mean peak values and mean valley values are calculated and subtracted to obtain the mean drop in friction coefficient for three different loading velocities. These values are then plotted as function of $\ln(V/V_0)$, where V_0 is chosen as 1 cm/hr, such that $\ln(V/V_0) = 0$ for loadpoint velocities of 1 cm/hr. Linear regression is used to obtain a relation between the loadpoint velocity and the size in friction drop. The slope of this relation gives the combined (a-b)-value in accordance with Beeler et al. (2001) and He et al. (2003) (see examples for sp-Qtz-gm and Sp-Fsp-gm in figure 8E and F). The obtained (a-b)-values are shown in table 2.

All materials show negative (a-b) values, indicating velocity weakening. Velocity weakening effects are relatively small when the basal contact consists of a plastic sheet. Salt is an exception and shows slightly larger negative (a-b)-values. Experiments with granular material as a basal decollement show relatively large negative (a-b) values, all in the same order of magnitude. The

velocity weakening effect of quartz sand and granular salt is slightly smaller with respect to feldspar and plastic sand.

Basal contact	Material	(a-b)-value
plastic sheet	Quartz sand	-0.0023
	Feldspar sand	-0.0079
	Plastic sand	-0.0095
	Granular salt	-0.0236
Quartz sand	Quartz sand	-0.0298
Feldspar sand	Feldspar sand	-0.0359
Plastic sand	Plastic sand	-0.0363
Granular salt	granular Salt	-0.0317

Table 2: (a-b)-values for quartz, feldspar, and plastic sand and granular salt for different basal contacts.

3.1.3 Material choice for subduction earthquake models

In theory, all tested granular materials produce unstable behaviour (stick-slips) at the experimental conditions, as long as the loadpoint velocities are sufficiently low. However, to interpret experimental results best, it is of importance that the material frictional behaviour can be predicted as well as possible. Regular stick-slips (e.g. constant recurrence time and size of friction drop) are thus favourable over varying behaviour. accordingly, plastic sheet provides the best basal contact. However, observed friction coefficients for this type of contact are very low and therefore not applicable. When unconfined granular material is used as basal decollement, plastic sand and granular salt show very irregular stick-slips or stable sliding at low loadpoint velocity, which makes their behaviour too unpredictable. Feldspar and quartz sand, on the other hand, still show relatively regular stick-slips at all loadpoint velocities and friction coefficients are significantly larger. The difference in (a-b)-value and size of the drops in friction during slip, makes these materials good candidates for the subduction earthquake models.

3.2 Subduction zone earthquake model

A range of experiments has been conducted in the subduction zone setup as described in section 2. Variables in these experiments are both the granular material and the loadpoint velocity (see table 3). Typical data obtained during the experiments, by the load cell, displacement sensor, and digital cameras, is shown in figure 9.

	Loadpoint velocity(cm/hr)		
Material	1.0	2.0	4.0
Quartz sand	Qtz-1	Qtz-2	Qtz-4
Feldspar sand	Fsp-1	Fsp-2	Fsp-4

Table 3: Subduction zone earthquake models. The first term denotes the type of material in the accretionary wedge and the second term denotes the loadpoint velocity

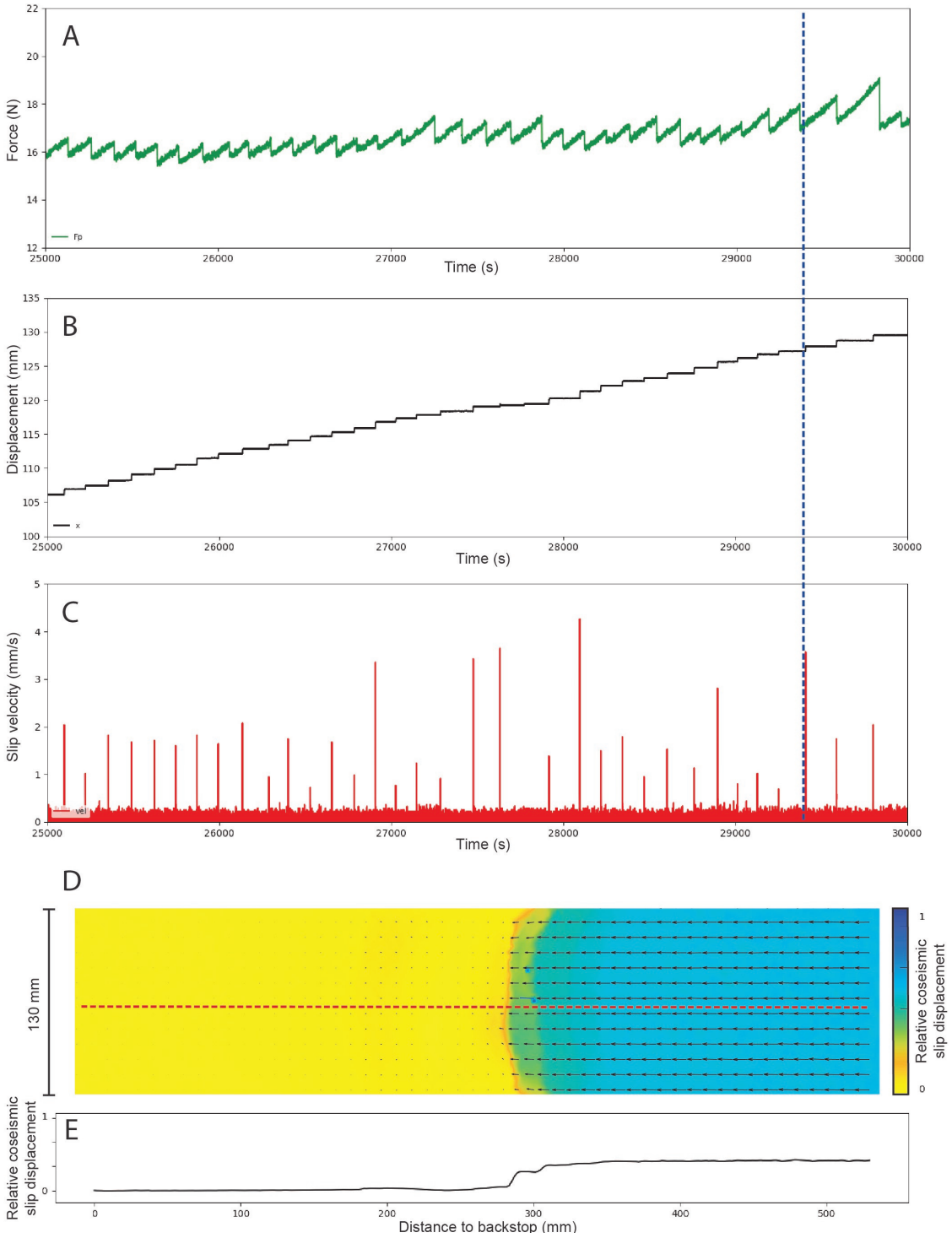

Figure 9: Typical experimental results of subduction zone megathrust models. (A) Loading force measured by the loadcell, as a function of time. (B) Accumulative displacement as function of time, measured by the displacement sensor and (C) the velocity, calculated as time derivative from the displacement.(D) Topview image of the model with relative surface slip displacements indicated by colours. Blue shades indicate relatively large displacements in the x-direction, yellow shades indicate small displacements. (E) 1D surface displacements measured at line transect on the topview image. The location of the 1D transect is shown by the red dashed line on the topview image. The blue dashed line in figure 9A-C indicates the slip that corresponds to the topview image and 1D transect.

3.2.1 Frictional behaviour

3.2.1.1 Drops in loading force

Loading force as a function of time for models Qtz-1, Qtz-2, Qtz-4, and Fsp-1 is shown in appendix B. Zooming in on each of the graphs shows a similar pattern as shown in figure 9A, with relatively long periods of a linear increase in loading force, followed by a rapid decrease in loading force. These periods correspond to a phase in which the subduction megathrust is locked ('stick' phase) and a period in which the subduction megathrust fault slips ('slip' phase) respectively.

Experiments with a wedge consisting of quartz sand all show 'stick-slip' behaviour. The size of the force drops, however, varies with time. The Qtz-1 model shows a gradual increase in stress drop with time or with accumulation of permanent deformation. Model Qtz-2 and Qtz-4 show a more random variation in size of force drop with occasionally a anomalously large force drop (see appendix B). At equal loading velocity, models with a feldspar wedge show larger force drops. Models Fsp-1, Fsp-2, and Fsp-4 show an increase in force drop with time or with accumulation of permanent deformation. Prior to large force drops, the linear increase of loading force is often interrupted by a small force drop. This behaviour is typical for models with a feldspar wedge and is not seen in models with a quartz wedge.

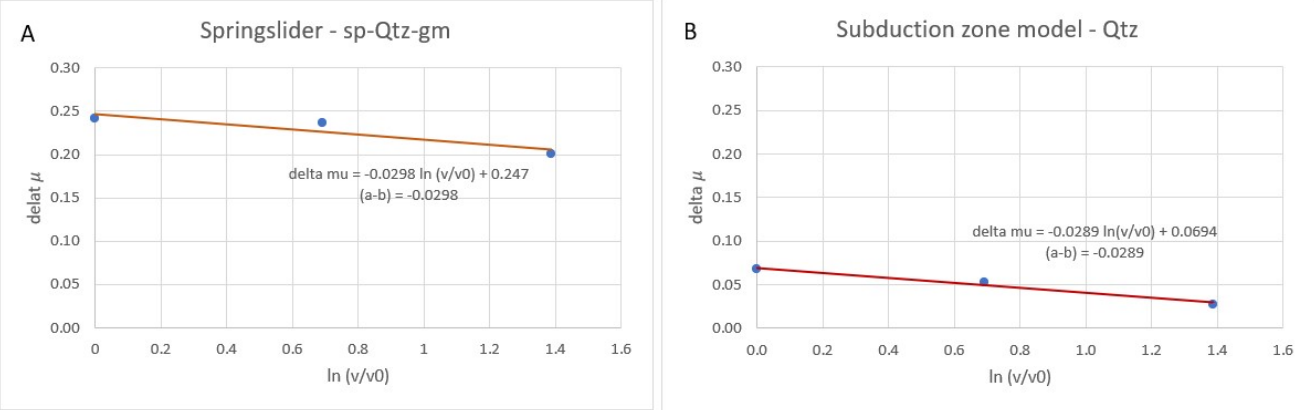

Figure 10: Friction drops (delta μ as function of $\ln(v/v_0)$ for (A) springslider experiment sp-Qtz-gm and for (B) Subduction zone models with quartz sand wedges. Linear regression is applied to obtain (a-b) values (slope of the linear relation).(a-b)-values are indicated on the graphs.

For models Qtz-1, Qtz-2, Qtz-4, and Fsp-1 force peaks and corresponding valleys have been identified with a Python based script. Force drops have been calculated by subtracting valley values from the peak values. Resulting sizes in force drops are plotted in histograms (see figure 12). High load point velocities produce smaller force drops (fig. 12A), whereas low load point velocities produce a wider distribution in force drops (figure 12B and C). The relation between loadpoint velocity and mean force drop is approximately inverse linear, though the standard deviation at small loadpoint velocity is very large (figure 11A). For the quartz sand wedge models, mean drops in friction coefficient are calculated by assuming that slip only takes place at the subduction megathrust fault and by assuming that the slip surface is similar for models with high, intermediate, and low loadpoint velocity (0.0429 m^3). The drops in friction coefficient are plotted as function of $\ln(v/v_0)$. Linear regression is used to obtain a relation between the loadpoint velocity and the size in friction drop. The slope of this relation gives the combined (a-b)-value, similarly as in the springslider experiments. The obtained value for the subduction zone model is very similar to that

of the springslider model (-0.0289 and -0.0298 respectively; see figure 10). At equal load point velocity, models with a feldspar wedge show a wider range in force drop values (see figure 12C and D), which corresponds to the interruption in linear increase of loading force by small force drops (see appendix B).

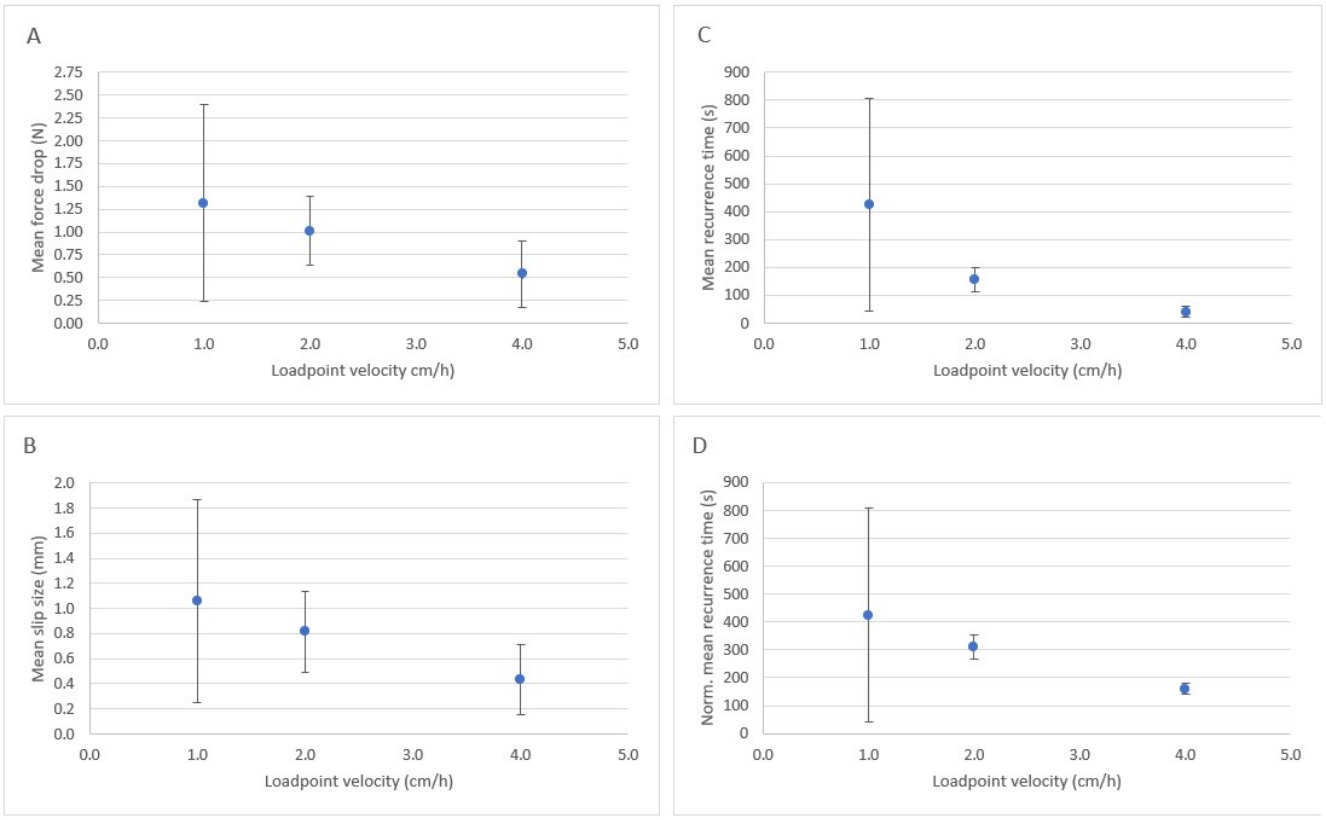

Figure 11: Mean values for (A) force drop, (B) slip size, and (C) recurrence time as function of loadpoint velocity. (D) normalized mean recurrence time, as function of loadpoint velocity. Standard deviations are indicated by black lines and show a increase with decreasing loadpoint velocity.

3.2.1.2 Slip displacement and velocity

Appendix C shows the cumulative displacement of the downgoing plate for models Qtz-4, Qtz-2, Qtz-1, and Fsp-1 respectively. All displacement is accumulated during the 'slip'-phase, resulting in a step-like pattern (see figure 9B). Every slip measured by the displacement sensor thus corresponds to a force drop, measured by the loadcell. From the output signal of the displacement sensor, slips are identified with a Python based script. Cumulative displacements after and before each individual slip are determined and subtracted to obtain the slip size. Slip sizes are plotted in histograms (see figure 13). From the histograms, similar trends as for the force drop distribution can be obtained: a high loadpoint velocity results in small slips (peak between 0.1 and 0.9 mm) and a small variation in slip size. A low loadpoint velocity produces a wider range in slip sizes. Models with a feldspar wedge show a wider distribution in slip size with respect to the quartz models. At a loadpoint velocity of 1 cm/hr, the Fsp-1 model shows slips up to 8 mm (not taking the first anomalously large slip into account), whereas the Qtz-1 model only shows slip sizes up to ~ 4 mm.

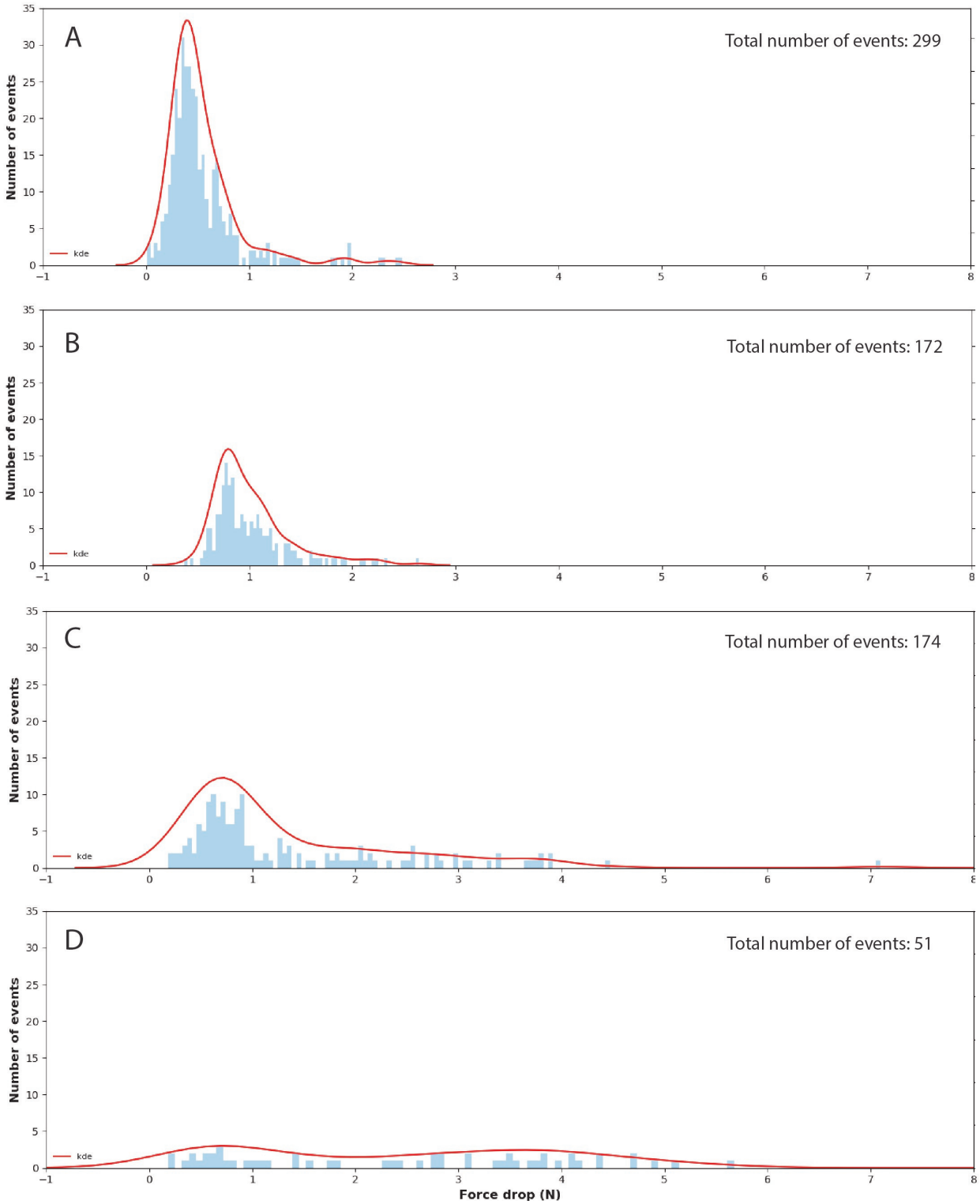

Figure 12: Force drop distribution for (A) model Qtz-4, (B) model Qtz-2, (C) model Qtz-1, and (D) model Fsp-1. The red curve indicates the kernel density estimation (kde) based on the number of events. The total number of measured events is indicated on the top right of each graph. Note that the data-sets of model Qtz-2 and Fsp-1 miss a number of events (also see appendix B - D).

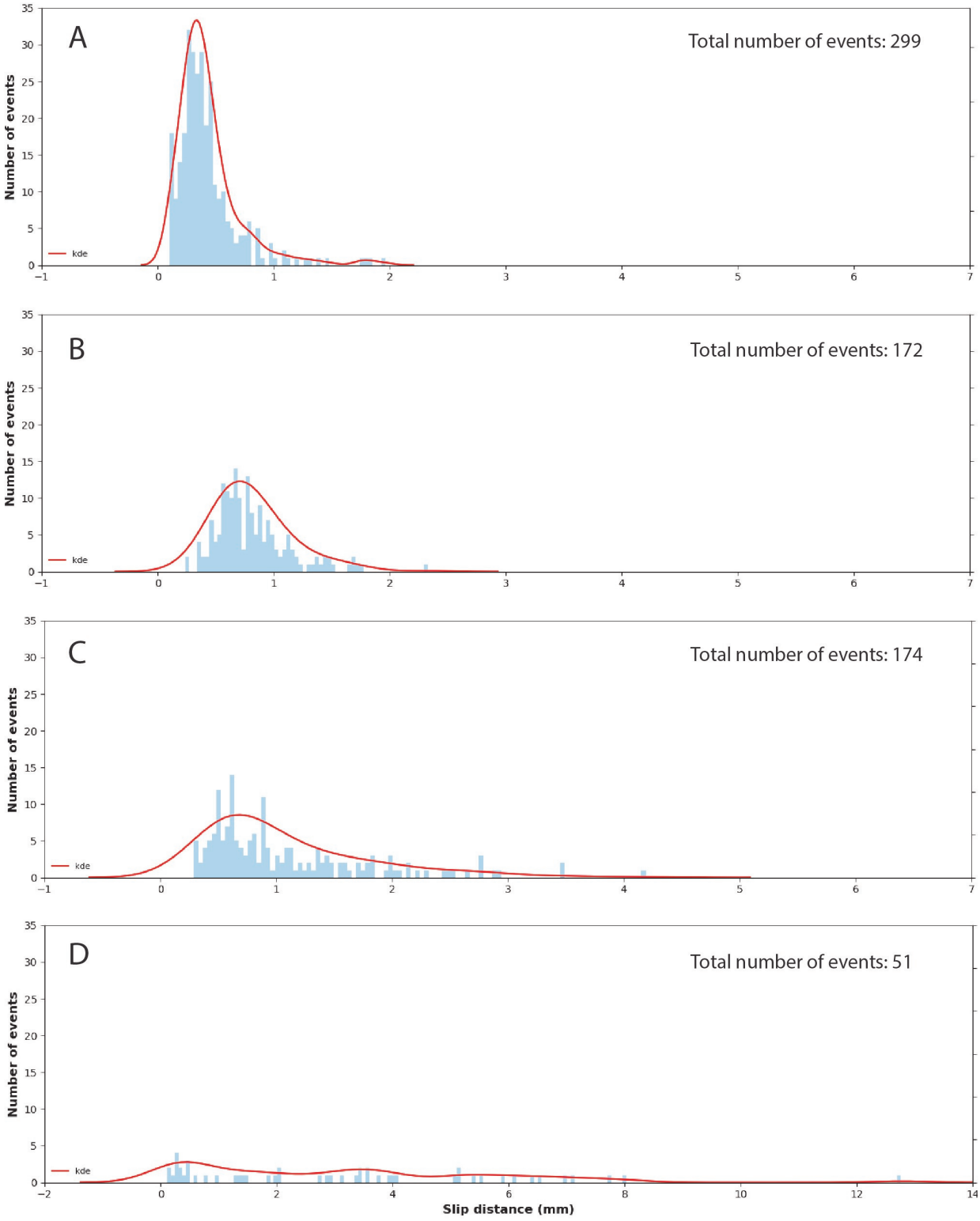

Figure 13: Slip size distribution for (A) model Qtz-4, (B) model Qtz-2, (C) model Qtz-1, and (D) model Fsp-1. Note that the horizontal scale for this model differs from the other models. The red curve indicates the kernel density estimation (kde) based on the number of events. The total number of measured events is indicated on the top right of each graph. Note that the data-sets of model Qtz-2 and Fsp-1 miss a number of events (also see appendix B - D).

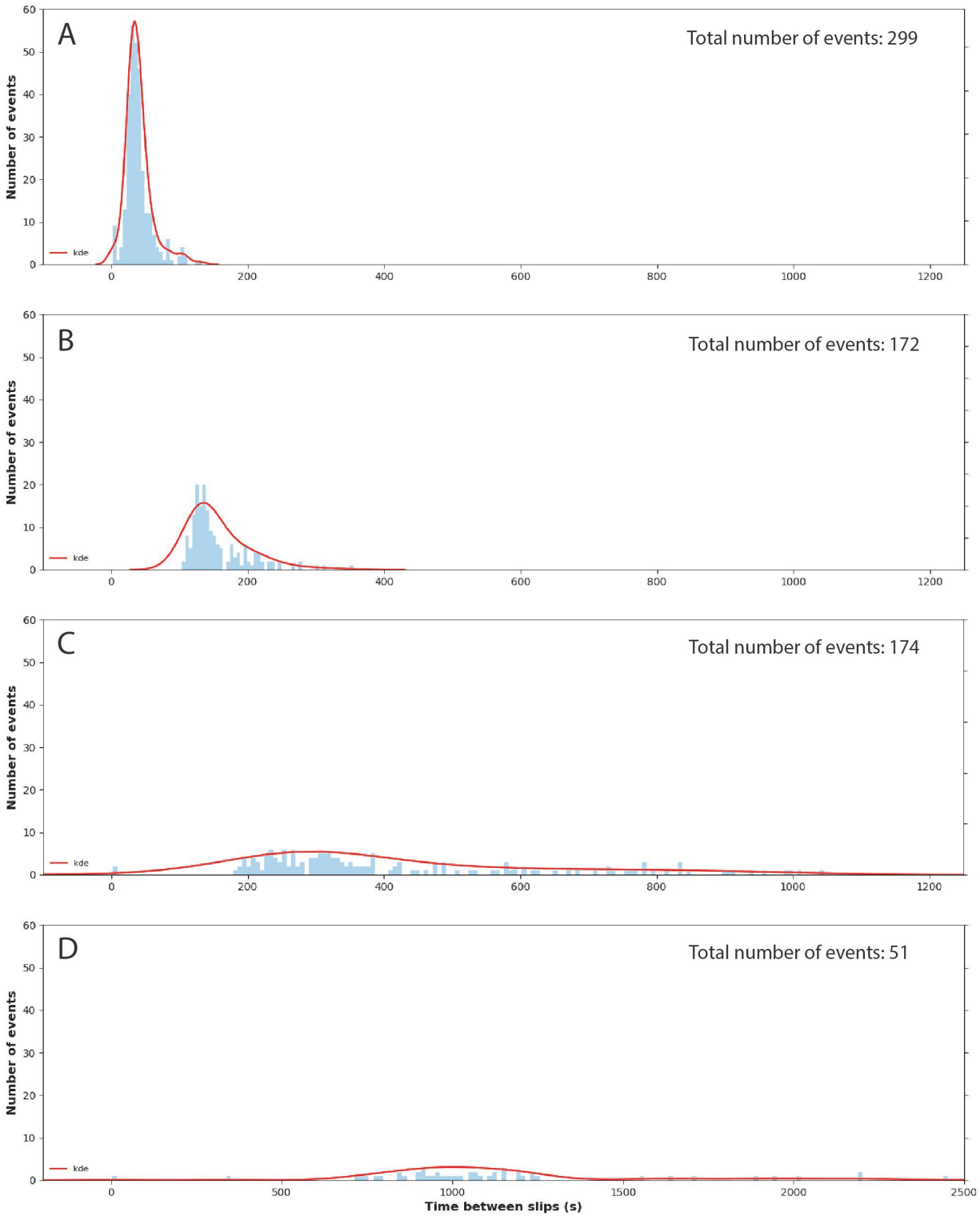

Figure 14: Distribution of time interval between slips for (A) model Qtz-4, (B) model Qtz-2, (C) model Qtz-1, and (D) model Fsp-1. Note that the horizontal scale for this model differs from the other models. The red curve indicates the kernel density estimation (kde) based on the number of events. The total number of measured events is indicated on the top right of each graph. Note that the data-sets of model Qtz-2 and Fsp-1 miss a number of events (also see appendix B - D).

The time derivative of the cumulative displacement gives the displacement velocity of the downgoing plate. Velocities for models Qtz-4, Qtz-2, Qtz-1, and Fsp-1 are shown in appendix D. Each peak in velocity corresponds to a single slip or lab-scale earthquake. High loadpoint velocities produce a larger number of velocity peaks, but a lower mean peak in velocity. At equal loadpoint velocity, models with a feldspar wedge produce significantly less and larger peaks with respect to the models with a quartz wedge.

3.2.1.3 Earthquake recurrence time

From the identified slips in the time-displacement graph, time-intervals between slips are determined. Time intervals between slips are plotted in histograms for models Qtz-4, Qtz-2, Qtz-1, and Fsp-1 (see figure 14. A linear increase in the loadpoint velocity causes a non-linear decrease in the time interval between slips (see figure 11C). If the mean recurrence times are normalized to loadpoints velocities, a linear relation can be obtained. Models with a lower loadpoint velocity, however, show a wider distribution in time interval between slips (see figure 11 and 14).

3.2.2 Large scale permanent deformation

3.2.2.1 Loadpoint velocity dependence

Final geometries of the brittle wedges as function of loadpoint velocity are shown in figure 15, where sections A-C show final geometries for wedges of quartz, deformed at different loadpoint velocities (model Qtz-4, Qtz-2 and Qtz-1). Common characteristics of deformed quartz wedges include: (1) The presence of a basal decollement defined by a zone of 1-2 mm thickness, near the contact between the wedge and the rigid downgoing plate. This zone extends from the backstop to the most updip frontal thrust. (2) All models show the presence of one main splay fault which connects the basal decollement to the surface of the model. This fault is active throughout most of the experiment and accommodates most of the shortening. (3) Several backthrusts develop above the ramp structure of the main splay fault. Backthrusts only show relatively small (< 5mm) amounts of displacement with respect to the main splay fault. (4) The updip section is characterized by an imbrication zone consisting of several thrust sheets. (5) The distribution of strain localization causes uplift of an area bounded by the innermost backthrust and outermost frontal thrust (F4 and F6 respectively in section A, figure 15). The inner part of the wedge shows relatively small amounts of deformation and uplift with respect to the outer part, and therefore forms a basin.

Despite the large similarity between models Qtz-1, Qtz-2 and Qtz-4, there are subtle differences in the characteristics of the final geometry: (1) Models with high loadpoint velocities produce less frontal thrusts, which each accommodate a relatively large amount of shortening each. Imbricated units are relatively long (> 40mm) and are separated by low angle thrust faults. Models with a low or intermediate loadpoint velocity (Qtz-1 and Qtz-2) show a large number of frontal thrusts which define the boundaries of relatively small (< 30mm) imbricated units. (2) At high load point velocity, imbrication dominantly occurs by frontal accretion. In the latter, continuous accommodation of shortening by faults F1 and F6 produces a duplex system, where the roof-thrust is defined by one of these faults (see sections B and C in figure 15). (3) Model Qtz-1 shows strain localization near the backstop during a relatively large portion of the slips (see appendix F), resulting in the formation of an additional thrust. Models with a higher loadpoint velocity show less strain localization near the backstop and no visible permanent deformation in cross-sections (note that high loadpoint velocities lead to smaller coseismic slip velocities).

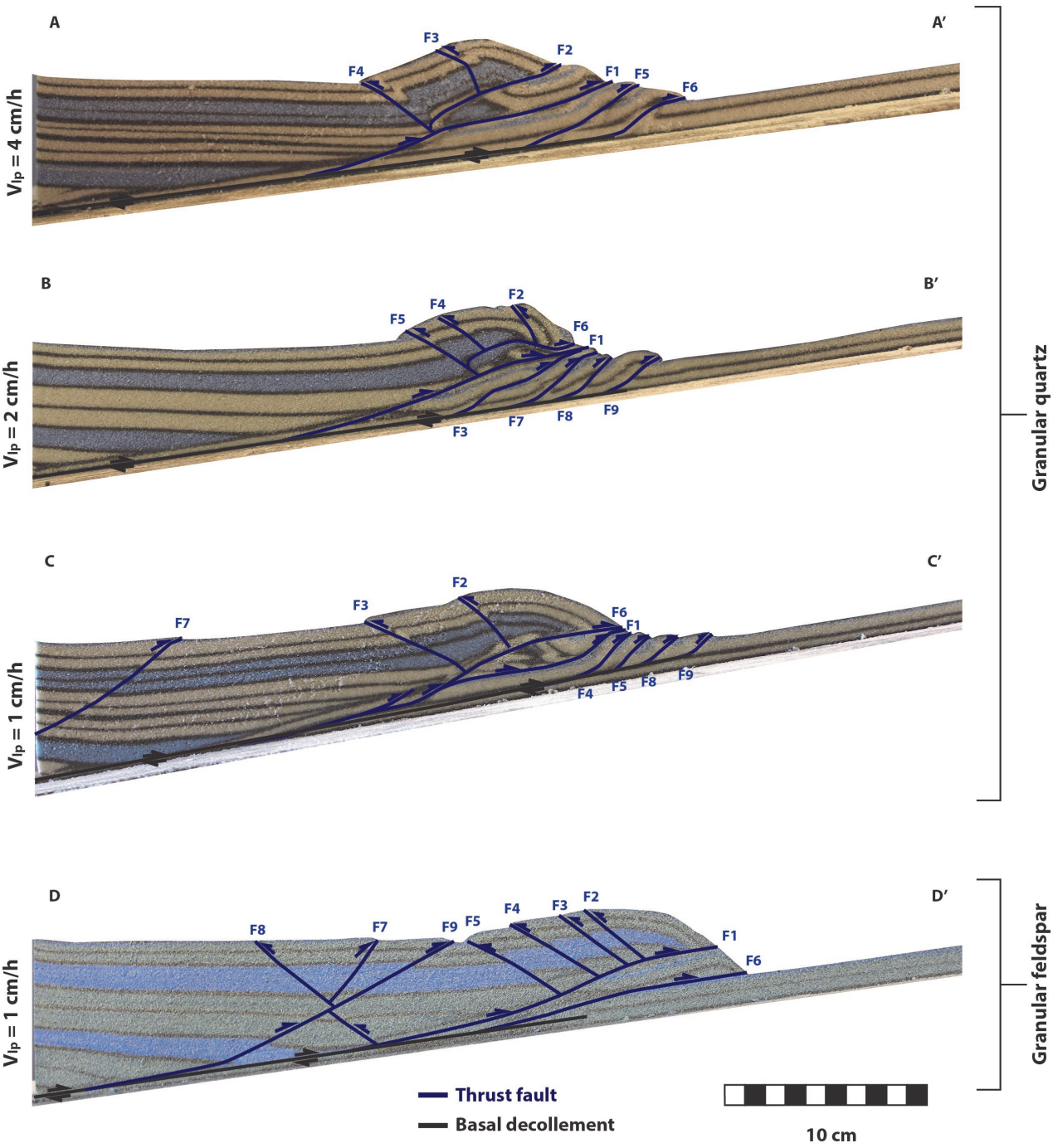

Figure 15: Cross-sections showing final permanent deformation for models (A) Qtz-4, (B) Qtz-2, (C) Qtz-1 and (D) Fsp-1. The upper three sections show the loadpoint velocity dependence, and the lower two graphs show the material dependence.

3.2.2.2 Material dependence

Models with a feldspar wedge show similar common characteristics as the quartz wedge models (see section D in figure 15). Significant differences include: (1) Most of the shortening is accommodated by underthrusting at only two or three frontal thrusts. The number of frontal thrusts is thus significantly lower with respect to the quartz wedge models. (2) The number of backthrusts formed above the ramp structure (F1) is significantly larger in the Fsp-models. The Fsp-1 model shows the presence of a large forethrust (F9) near the backstop which is similar to the thrust fault (F7) in model Qtz-1, although it is slightly further from the backstop and has more complex cross-cutting relationships with other faults (F7 and F8).

3.2.3 Faulting pattern and temporal evolution of frictional behaviour

Faulting (re-)activation patterns are obtained from visually analyzing top view images, played in time-lapse videos. Faulting (re-)activation patterns of different models show small variations. The main sequence in fault formation is, however, similar. In this section, the structural development of model Qtz-2 is described and linked to the frictional behaviour at the subduction megathrust.

Permanent deformation starts with compaction of the entire wedge, accomodating ∼3.5 mm of shortening. Compaction is followed by the formation of a frontal thrust (F1) at the tip of the wedge. This fault forms a flat-ramp-flat structure and remains active during most of the slips since it continues to accommodate shortening. Above the ramp, backthrusts (F2, F4, F5) develop during ongoing activity of the F1 thrust (see figure 15, section B). The location at which fault F1 crops out, slightly translates towards the backstop. During ongoing shortening, new frontal thrusts develop. The main splay fault (F1) remains active during this stage of deformation. Fault slip at the newly formed frontal thrusts does not occur during every seismic event (see section below). The F1 fault, on the other hand, gets re-activated during every slip. After the formation of the F3 frontal thrust, a new roofthrust (F5), develops. This thrust branches from the F1 thrust fault and is deformed by the ongoing activity on the F1 fault and the backthrust (F6) above the ramp structure. From top-view images, a fault nucleation line can be identified, at constant distance from the backstop. Approximately at this distance, new frontal thrusts reach the model's surface after nucleation.

The last 35 slips of model Qtz-2 are analyzed in more detail. Photographs of the model surface prior to and just after each individual slip are analyzed with the use of particle imaging velocimetry (PIVlab). From these photographs, relative coseismic slip displacement in the x-direction are determined, as well as 1D-velocity sections over the entire length of the model (see appendix G). Fault activity is then linked to the size of force drop, slip size and slip velocity for individual events. All 35 slips have been numbered and slip 30 is indicated on the force, displacement and velocity graph (see figures 16 and appendix G).

Events 1 - 27 only show minor variations in force drop and coseismic slip displacement with respect to one-another. Events 28 - 31 show anomalously large recurrence times, resulting in higher peak loading force. Since the size of the force drop initially does not increase, the mean loading force continues to rise until event 30 and 31, which show relatively large force drops and slip sizes. Deformation during these two events is mainly accommodated by the main thrust fault (F1) and frontal thrust F9, as well as frontal thrusts F8 and backthrust F5 (see figure 16D and cross-section C in figure 15). After these two slips, a new mean loading force has established and the size of the force drops becomes similar as prior to the temporal increase in mean loading force.

1D-coseismic slip displacement graphs show the initiation of strain localization of F9 during

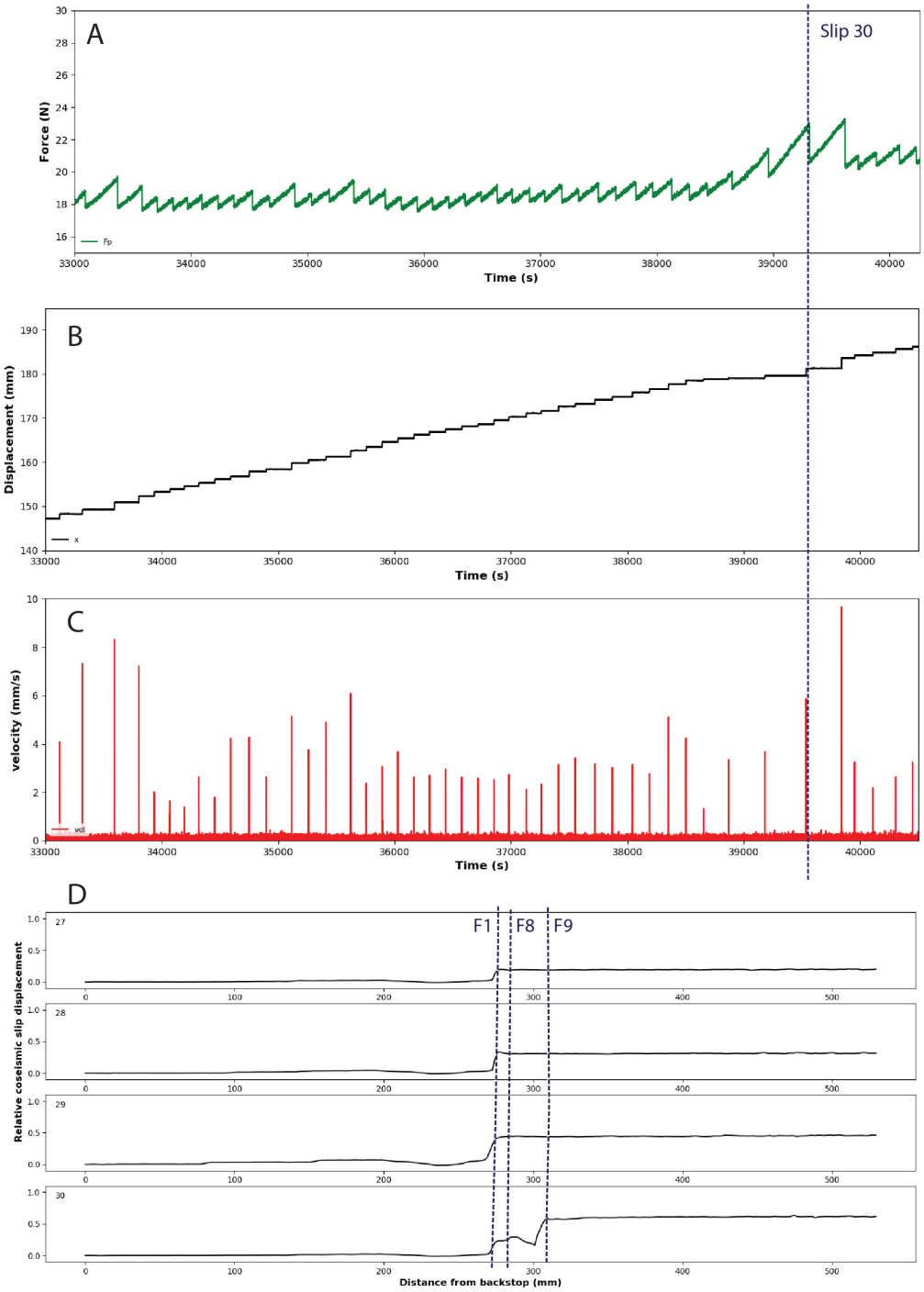

Figure 16: Fault activity during the last 35 slips in model Qtz-2. (A) loading force through time, (B) Corresponding accumulative displacement and (C) velocity of the downgoing plate. Slip 30 is indicated with a blue dashed line and shown in (D) a 1D-velocity section along with slips 27 - 29. 1D coseismic slip displacements for all 35 analyzed events are shown in appendix G.

'event 1' (see appendix G). The same graph also shows re-activation of faults F1 and F8. After the development of the first surface expressions of fault F9, the size of slips and force drops does not change abruptly, as described above. Fault activity in the model is characterized by: (1) re-activation of fault F1 during every event. (2) A somewhat random, but always simultaneous re-activation of faults F8 and F9. Randomness of activation is characterized by intervals in which faults F8 and F9 get reactivated during subsequent slips ('events 7 - 11') and intervals in which they get reactivated once every two slips ('events 12 - 27'). (3) Fault re-activation of faults F8 and F9 occurs mainly, but not exclusively, at relatively large events. (4) Strain localization close to the backstop (0 - 250 mm from backstop) occurs mainly when faults F8 and F9 are not active or during anomalously large slips ('event 30 and 31').

Although changes in frictional behaviour cannot be linked directly to the formation of a new thrust fault, ongoing accretion of material coincides with an increase in slip size and force drop size. Particularly in the feldspar models the temporal change in macroscopic frictional behaviour is apparent. This also applies to the Qtz-1 model whereas the Qtz-2 and Qtz-4 models do show variations in macroscopic frictional behaviour, but no clear trend with time or ongoing accumulation of material for that matter.

4 Discussion

4.1 Frictional behaviour springslider experiments

For quartz sand and feldspar sand, (a-b)-values of the springslider experiments in this study are compared to the values obtained at GFZ Potsdam by performing velocity stepping tests (Willingshofer et al., 2018) (see table 4). In the velocity stepping tests a constant normal stress of 2000 Pa is applied and the initial shear velocity is 180 cm/h. After reaching a plateau of dynamic friction, velocity is decreased in logarithmic steps down to a velocity of 0.6 cm/h. Obtained friction coefficients are plotted against the shear velocity. Rate and state dependency is then calculated from the logarithmic curve through the data points. Velocity stepping tests show the onset of stick-slip behaviour of both quartz sand and feldspar sand at velocities below 6 cm/h. This is consistent with the behaviour of both materials in the springslider experiments performed at 1, 2 and 4 cm/hr. Rate and state dependencies measured in this study have the same order of magnitude as in the velocity stepping tests. Springslider experiments show a slightly larger rate and state dependency of feldspar, whereas velocity stepping tests show the opposite (see table 4).

	GFZ Potsdam		This study	
Material	(a-b)-value	std dev.	(a-b)-value	std dev.
Quartz sand	-0.0504	0.0012	-0.0298	0.0068
Feldspar sand	-0.0127	0.0003	-0.0359	0.0010

Table 4: (a-b)-values for quartz, feldspar obtained by velocity stepping tests in a ring shear apparatus at GFZ Potsdam (Willingshofer et al., 2018), and in springslider experiments in this study

Small differences in the rate and state dependency of experiments conducted in this study and in ring shear tests performed at GFZ Potsdam might be explained by the different boundary conditions. As mentioned in the material sections, velocity stepping tests are performed at slightly higher normal loads (2000 Pa) with respect to the springslider experiments in this study ($\sim$910 Pa). Additionally, springslider experiments have an open boundary at the top, whereas the samples

in velocity stepping tests are confined at all boundaries. Finally, velocity stepping tests include friction coefficient values in a wider velocity range, including velocities up to 180 cm/h.

It is believed that springslider experiments represent the frictional conditions of the subduction zone megathrust models very well (see figure 10). A number of small adjustments of the set-up, however, could improve the quantitative analysis of granular materials in springslider experiments. Friction at the interface between the plexiglass box and the basal material can be reduced by using small rollers over which the box can be transported. Additionally, the friction coefficient should be determined for a larger range of loadpoint velocities to obtain more reliable results.

4.2 Subduction zone megathrust model performance and limitations

In this section, the model frictional behaviour and deformation is compared to previous analogue models and the seismic behaviour and deformation in the natural prototype. This includes recurrence times and slip sizes, transient deformation, and permanent deformation.

4.2.1 Recurrence time and slip size

Several simple deterministic models of stress build-up and release have been proposed to describe cyclicity in earthquakes (Corbi et al., 2013). The simplest of these models is the so-called characteristic earthquake model (Reid, 1910) which hypothesizes that faults rupture at regular intervals and with similar size (see figure 17a). More complex, non-characteristic models distinguish between time-predictability and slip-predictability (Shimazaki and Nakata, 1980). Time-predictable models are based on the assumption that a fault ruptures at a constant threshold strength (see figure 17b). This implies that a large slip causes a larger reduction in shear stress, and therefore results in a longer interseismic period, with respect to a small slip (Corbi et al., 2013). Slip-predictable models, on the other hand, require the assumption that during the seismic event, shear stress reduces to a fixed value (see figure 17c). A longer interseismic period consequently results in a larger stress-drop, assuming that shear stress increases with time in a constant linear manner.

The models in this study show a large variation in both recurrence times and in slip sizes. Therefore it is not possible to fit the slip data to the time-predictable model nor the slip-predictable model. This is consistent with previous analogue models of subduction zones (e.g. Rosenau et al., 2009; Corbi et al., 2013). These studies assign the non-characteristic, non-predictable behaviour of subduction zone models to the number of degrees of freedom. Simple spring-block models and ring shear tests are able to produce more characteristic behaviour, if fixed loading rates and energy-release conditions are applied (Rosenau et al., 2009; Corbi et al., 2013). Subduction zone models, however, have varying rupture size, as well as loading conditions due to accretion and deformation of the wedge, adding a degree of freedom. The models in this study additionally show that decreasing the loadpoint velocity, causes an increase in variation in slip size and recurrence time. Consequently, the earthquake predictability decreases. Models with a feldspar wedge show a similar wider distribution with respect to quartz wedge models at similar loading velocities, and hence have a lower predictability. This material dependency is further discussed in section 4.2.4.

Recurrence predictability is, of course, time-scale dependent. The models in this study as well as other studies (e.g. Rosenau et al., 2009) show time-predictable, slip-predictable, or even characteristic behaviour at short time intervals. This pinpoints the problem in predicting earthquake behaviour in natural complex subduction zones. Based on the short instrumental seismic record and geological indicators, a distinction in behaviour between global subduction zones is made. A paleoseismic analysis on beach-berm crests (Bookhagen et al., 2006), for example, shows that the

Chile subduction zone shows quasi-periodic earthquake behaviour since the Holocene. A similar analysis shows that the Nankaido subduction zone in Japan shows time-predictable behaviour since the Holocene. The Cascadia subduction zone, on the other hand, shows more complex behaviour which can not be described by the time-predictable, nor the slip-predictable model (Satake and Atwater, 2007). All paleoseismic studies have data on a limited amount of earthquakes. As the models in this study show, any sort of predictability obtained from paleo-data does not guarantee continuation of this behaviour in the future.

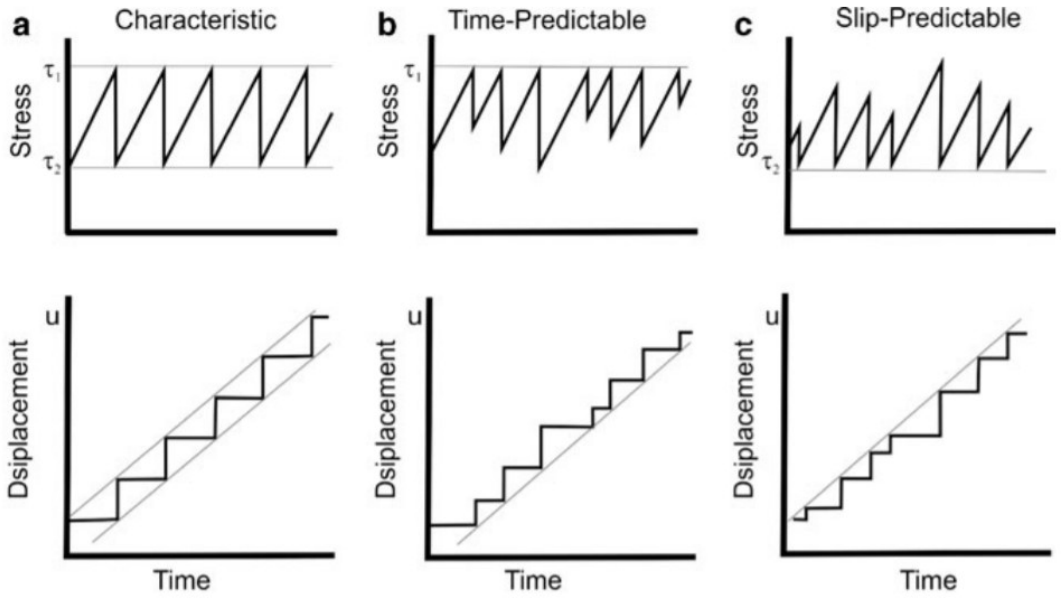

Figure 17: Earthquake recurrence models (Beer et al., 2015). The upper panel shows the temporal change in stress and the lower panel shows the accumulative slip displacement for (a) the characteristic model, (b) the time-predictable model, and (c) the slip-predictable model

A length scale ratio of $l^* = 6.6 * 10^{-6}$ is applied to the Qtz-models in this study. 1 mm in the model thus represents ∼150 m in nature. Model Qtz-4 produces a maximum amount of slip in the order of ∼300 m during individual events, if scaled to nature. This is one order of magnitude too large with respect to what is estimated for single events in nature (e.g. in the Nankai subduction zone; Hamada et al., 2015). Quartz sand models at lower loadpoint velocities, and feldspar sand models produce even larger slips during individual events. In future studies, slip size of the model might be reduced by increasing the loadpoint velocity or by increasing the stiffness of the loading mechanism. Smaller events however also require a higher monitoring resolution.

4.2.2 Transient deformation

The models in this study do not take viscous relaxation into account. Therefore we only make a simple distinction between the seismic phase and the interseismic phase to discuss transient motions. As described in the introduction, GPS-data shows seaward motions of the overriding wedge during the seismic event, and landward motions when the seismogenic zone is locked (Wang, 2007; Govers et al., 2018). These motions are attributed to elastic loading and unloading of the overriding wedge. The models in this study are not able to reproduce this behaviour and only show landward motions during the seismic event. This discrepancy in behaviour between nature and our model can be explained by the elasticity of the material we use. The Bulk modulus

of granular quartz ranges between 632 and 1829 MPa (Klinkmüller et al., 2016), which is 1-2 orders of magnitude lower than natural rocks. If the appropriate scaling factor is applied, the bulk modulus of the analogue materials should be 6 orders of magnitude smaller (0.1 MPa). The high bulk modulus of the models in this study prevents the wedge from deforming elastically. Instead, deformation in the wedge is predominantly brittle. This problem can be resolved by adding rubber grains to the wedge (Rosenau et al., 2009). Adding rubber however also changes the internal frictional properties. In this study, we did not change the frictional properties of the material and accept the compromise that elasticity is not scaled correctly. It would be useful to run models with a predominantly elastic wedge and compare the results.

4.2.3 Permanent deformation

Permanent deformation in all models accumulates in a number of faults which are interpreted as splay faults, backthrusts, and frontal thrusts. Deformation in fold-and-thrust belts of accretionary wedges is classically explained by the critical taper theory (Davis et al., 1983; Dahlen, 1984; Dahlen et al., 1984). This theory is based on the assumption that the overall mechanics of accretionary wedges are analogous to that of a wedge of snow in front of a bulldozer. When the wedge has a critical angle (critical taper), it is on the verge of failure everywhere, including at the basal decollement. A wedge smaller than the critical taper will not slide over the decollement but will deform internally, resulting in an increase in angle. On the other hand, a wedge larger than the critical taper will slide over the decollement while frontal accretion occurs, resulting in a smaller taper angle. The angle of the critical taper depends, amongst others, on the friction along the decollement and the internal strength of the wedge. Increasing the basal friction leads to an increase in the critical taper, whereas an increase in internal strength leads to a decrease in critical taper angle (Davis et al., 1983; Dahlen et al., 1984). In terms of strain localization, accretionary wedges with different basal frictions behave in a different way. Accretion of material in a wedge with high basal friction occurs by underthrusting. The wedge grows by imbrication of typically long tectonic units, bounded by low angle thrusts (Malavieille, 2010). This structural style of deformation is seen in the models of this study where loadpoint velocities are relatively high (Qtz-4) and when the wedge material consists of feldspar (see figure 15). Wedges with low basal friction typically show frontal accretion by imbrication of typically small tectonic units. During frontal accretion, the basal decollement propagates forward (Malavieille, 2010). Models in this study show a similar structural style of deformation when loadpoint velocities are relatively low, and when the wedge consists of quartz (Qtz-1 and Qtz-2).

Differences in structural behaviour between feldspar models and quartz models can be explained by the critical taper theory. The coefficient of reactivation friction of feldspar is slightly higher than that of quartz (0.6 and 0.5 respectively; Willingshofer et al., 2018). This implies that feldspar models have slightly higher basal friction. The critical taper theory, however, requires the assumption that acceleration is negligible, and that basal friction has a constant value over the entire basal decollement. In addition, the assumption is made that all the material in the wedge is constantly on the verge of shear failure. This might be applicable in only a small number of subduction zones where only aseismic slip takes place (Wang and Hu, 2006). The other end-member scenario would be a subduction zone where slip takes only place during the coseismic stage, and in the interseismic period, the megathrust fault is locked (Wang and Hu, 2006). The latter applies to the models in this study. This scenario requires that acceleration, rate and state friction, and cyclic variations in shear stress are taken into account. The dynamic Coulomb wedge concept (Wang and Hu, 2006) includes these processes to explain deformation in subduction wedges. Exact stress solutions have

been determined for the end-member case.

According to the dynamic Coulomb wedge concept, different structural styles apply to the inner wedge (landward) and the outer wedge (seaward). In the end-member case, basal friction is similar in both sections of the wedge, and increases during elastic loading of the wedge. The stress level increases until fault failure occurs. At the coseismic stage, the inner wedge segment of the subduction megathrust behaves in velocity weakening manner, whereas the outer wedge segment behaves velocity strengthening due to its unconsolidated character (Wang and Hu, 2006). As a result, the state of stress in the outer and inner wedge are different. The outer wedge acts as a backstop, and little or no internal deformation takes place. Slip thus localizes at the basal decollement. The inner wedge, on the other hand, is pushed in the critical state and deforms internally (see figure 18 Wang and Hu, 2006).

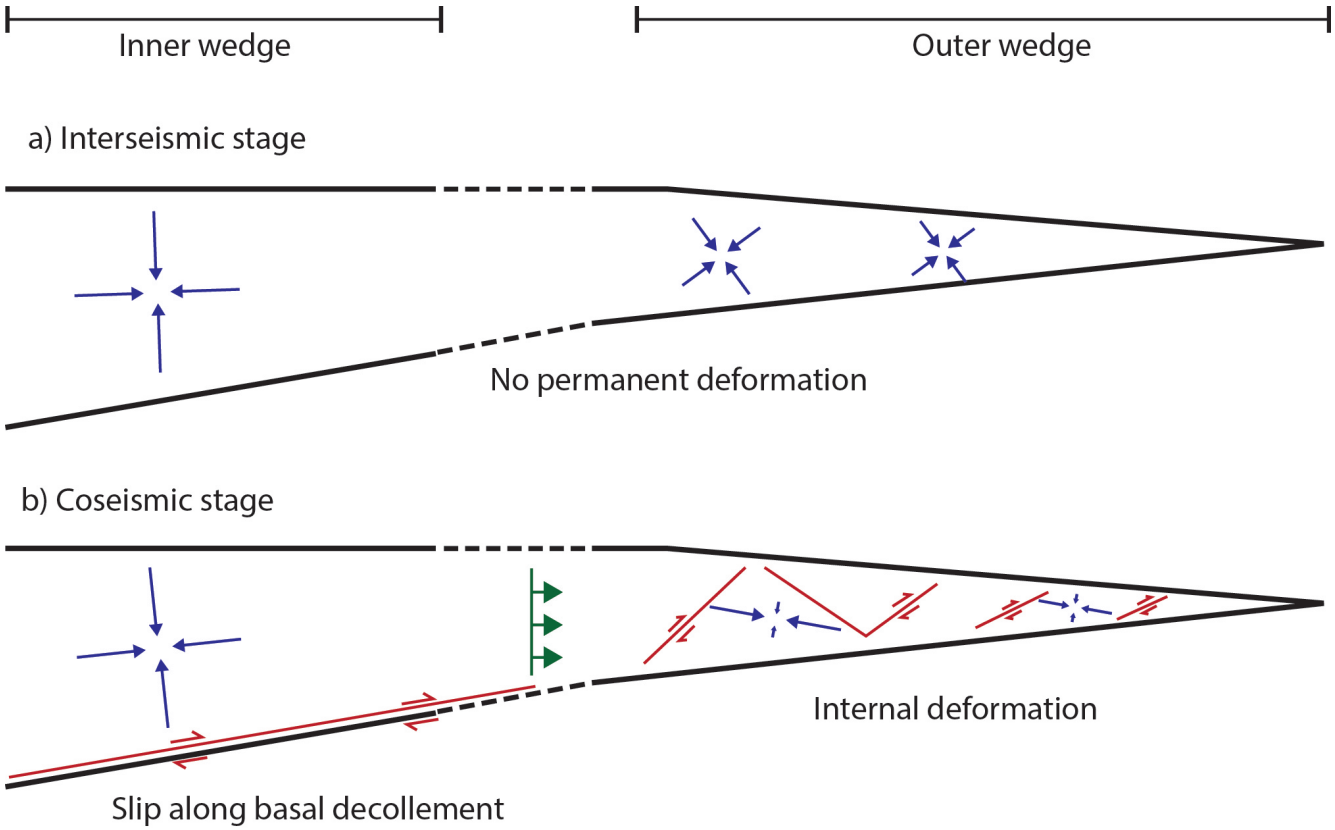

Figure 18: Conceptual illustration of dynamic wedge theory, modified after Wang and Hu (2006). A distinction is made between the inner wedge, where almost no permanent deformation accumulates, and the outer wedge, where thrust faults develop. (a) during the interseismic stage, no permanent deformation occurs in the models of this study. (b) During the coseismic stage, deformation in the inner wedge occurs by slip along the basal decollement, whereas deformation in the outer wedge is characterized by internal deformation. Blue arrows indicate the state of stress, red arrows indicate slip, and the green line indicates the location of the hypothetical backstop. Note that in the dynamic wedge theory (Wang and Hu, 2006) also stress solutions for the postseismic stage are formulated and that slip along the basal decollement, in the outer wedge, occurs during the interseismic stage. Models in this study do not show deformation in the interseismic stage.

In terms of geometry the models in this study show a similar distinction with an inner wedge which shows little or no internal deformation, and an outer wedge where most of the permanent deformation is localized (see figure 15). During the coseismic phase, slip occurs at the subduction

megathrust overlain by the inner wedge. The outer wedge section of the megathrust fault is more or less locked during this stage and splay faults or frontal thrusts develop above the decollement. The wedge of models in this study consist entirely of unconsolidated material. Therefore a distinction between outer wedge and inner wedge can not be made, based on the degree of consolidation and the resulting velocity weakening effects. A distinction, however, can be made, based on part of the wedge which is pushed in the critical state during the event, and part of the wedge which is not. The inner part of the wedge which is not pushed in the critical state acts as a backstop for the outer wedge (see figure 18).

Wedge segmentation is also believed to be controlled by the ratio between frictional strength at the basal decollement and and the internal frictional strength of the wedge (Lohrmann et al., 2003). Decreasing this ratio allows for a smaller critical taper. When applied to the models in this study, the wedges of all models can be subdivided in an outer part with internal deformation and where the critical taper is relatively steep, and an inner wedge with no or little internal deformation and a small taper angle. This suggests a small ratio between internal frictional strength and strength of the basal decollement in the outer wedge, and a large ratio in the inner wedge section allowing sliding over the basal decollement rather than internal deformation at that section. Lohrmann et al. (2003) suggest an increase of bulk strength due to fault rotation and associated plastic hardening as a possible mechanism for an increased ratio. This, however, does not apply to our models, since the inner wedge has (almost) no internal deformation due to the initial set-up (e.g. angle of the wedge). Another possible mechanism mentioned by Lohrmann et al. (2003) is weakening of the basal shear zone by a deformation-dependent process. This process was, however not observed by ring-shear experiments performed in that study. Models performed by Lohrmann et al. (2003) do not involve stick-slip behaviour and therefore do not include rapid accelerations as seen in the models of this study. The high velocities produced during the slip events might cause weakening by a deformation-dependent process. This is further discussed deformation mechanisms section below.

Models with small loadpoint velocity show forward propagation of the basal decollement after a number of earthquake cycles. Once propagation has established, slip occurs at this section as well as during the following events. This could indicate that friction at the outer wedge section of the basal decollement is lower for models with smaller loadpoint velocities. This is consistent with the observation that those models produce larger slip velocities resulting in more reduction in friction during the coseismic stage. This is also in agreement with a numerical study on the effects of e.g. velocity weakening on deformation patterns in accretionary wedges (Ruh et al., 2014). Results of this study show that when velocity weakening is more difficult, less zones of strain localization develop. The same pattern is seen in the models of this study: When loadpoint velocity is increased, less zones of deformation develop in the outer wedge.

Exact stress solutions formulated by Wang and Hu (2006) apply to the inner and outer wedge. The state of stress in the transition between the two sections however remains unsolved. Especially in models with large slip velocities and displacements (Qtz-1 and Fsp-1), strain also localizes closer to the backstop, which is interpreted as the transition zone. Internal deformation requires that this section of the wedge is pushed into the compressible critical state during large slip velocities. These slip velocities are (almost) never reached in models Qtz-2 and Qtz-4 and therefore they lack strain localization near the backstop.

The initiation of thrust faults in analogue models has been studied by Dotare et al. (2016). By using high-resolution digital image correlation techniques, different stages in the formation of new thrust faults were identified: Stage 1: a number of weak shear bands form in front of an already existing thrust fault. The pre-existing thrust fault remains active. Stage 2: Strain localizes in one of the strain bands and a new thrust fault develops. The activity on the pre-existing thrust

fault decreases. Stage 3: only the new thrust fault is active. PIV-analysis of the models in this study show a similar onset of deformation, first by the formation of weak shear bands, without the presence of distinct thrust faults, and in a later stage the formation of the thrust fault. Decreasing activity of the already existing thrust faults, however, is not observed. In the study of Dotare et al. (2016), a constant loading velocity is applied on the accretionary wedge. Therefore, cyclic changes in stress (as described in the dynamic wedge theory) as a result of the loading mechanism are absent. The build-up and sudden release of stress in the models of this study is believed to result in the simultaneous (re-) activation of several faults to accommodate the total amount of slip required for the stress release.

Permanent deformation is compared to the natural prototype of the Nankai Trough, Japan (see figure 19). The Nankai Trough has been a site of intense study, including seismic reflection surveys and deep sea drilling projects, due to its long record of great eartquakes and resulting tsunamis (Moore et al., 2009). The Philippine Sea Plate is subducting beneath Southwest Japan at a rate of approximately 4-6.5 cm/year. Structural restoration of thrusts at the toe of the Nankai Trough has shown that more than 40 km of shortening of typically terrigenous sediments has taken place in the outer wedge (Moore et al., 2011). Model Qtz-1 has a total amount of shortening of 20 cm which corresponds to 30 km in nature if scaled correctly. The similarities between the model and natural prototype are striking. Both the model and natural prototype show the presence of splay faults, defining the boundary between an imbricated outer wedge and a less deformed section landward of the model. The less deformed inner part of the wedge shows less uplift and is interpreted as a forearc basin similar to the one indicated on the Nankai Trough seismic section (see figure 19B). Note that processes such as erosion, sedimentation, and isostasy are not accounted for in the model.

The overriding wedge in model Qtz-1 consists of quartz with a bulk modulus in the order of 1000 MPa. If scaled to the natural prototype, the bulk modulus should, however, be in the order of 0.1 Mpa. The transient deformation patterns seen in nature (Wang, 2007; Govers et al., 2018) and in previous analogue modelling studies (Rosenau et al., 2009; Corbi et al., 2013) are not seen in the models of this study. Permanent deformation geometries, after 20 cm of shortening, seen in the models of this study are, however, strikingly similar to the accretionary wedge geometry of the Nankai through (figure 19). This could indicate that transient elastic deformation does not have a major impact on the cumulative finite deformation of the accretionary wedge.

4.2.4 Deformation mechanisms

Deformation mechanisms under the experimental conditions of this study differ from those under the natural conditions due to the absence of high pressures, fluids, and a geothermal gradient. Even though the deformation mechanisms are different, similar permanent deformation geometries are produced (see figure 19). Here the deformation mechanisms at the basal decollement in the model are discussed and compared to deformation mechanisms in nature.

Granular materials exposed to shear flow under small normal loads (such that no breaking of grains occurs) show two opposite effects: packing density reduction due to dilatancy (Reynolds, 1886) on one hand, and gravity driven and shear driven reorientation of grains resulting in compaction (Wegner et al., 2014) on the other hand. A study on the effects of grain shape on dilatancy and packing of sheared granular materials by Wegner et al. (2014), shows that only when perfectly spherical materials are sheared, compaction takes place. Conversely, dilation takes place when non-spherical granular materials are sheared. Reorientation processes for grains with a large aspect ratio (length/diameter), however, compensate partly for a density reduction (Wegner

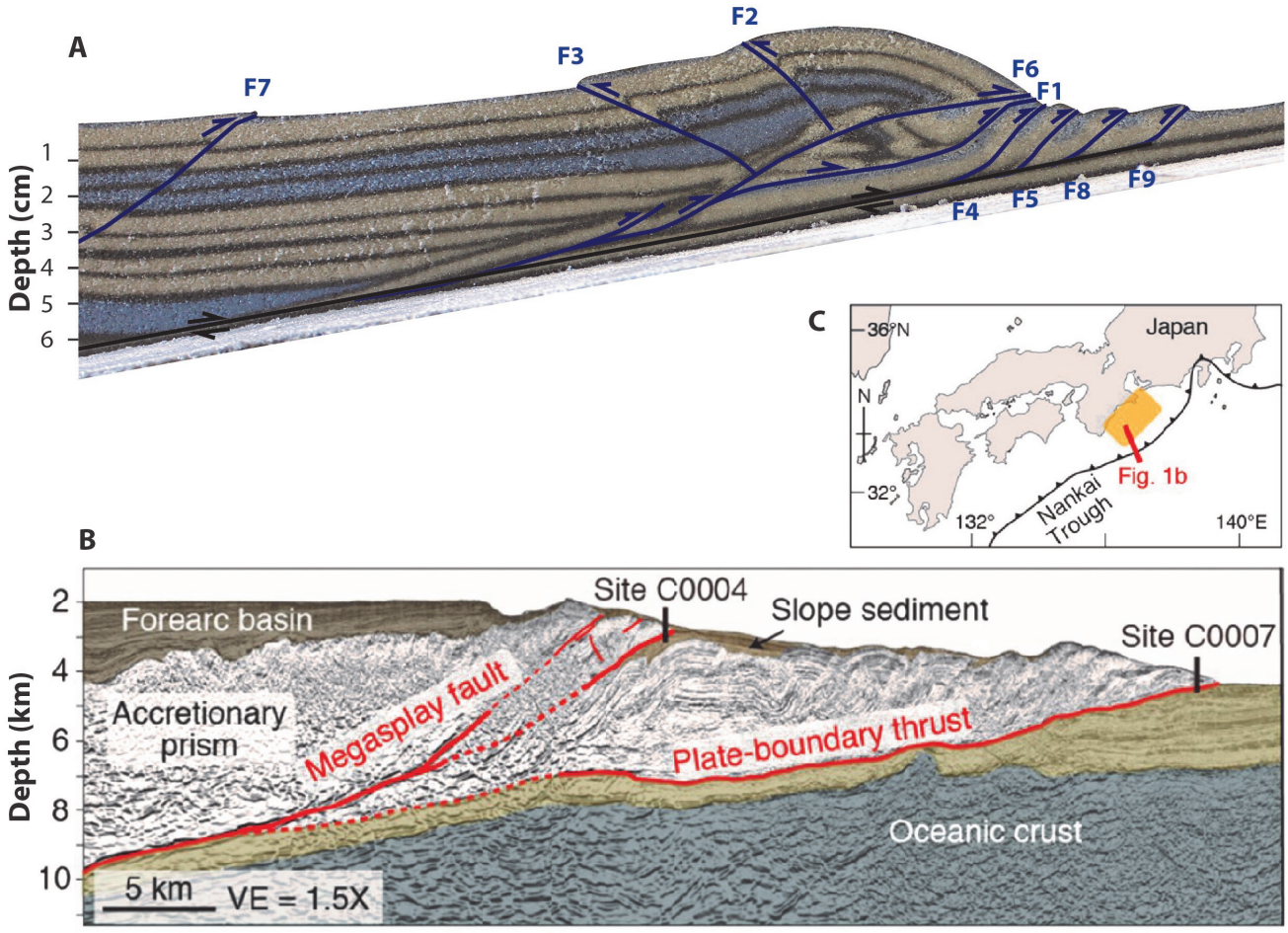

Figure 19: Comparison of permanent deformation in the accretionary prism of model Qtz-1 (A) and the the Nankai Trough for the coast of Japan (B). The seismic profile of the Nankai Trough shows locations of drilling sites (C0004 and C0007) and interpreted megasplay faults and the plate-boundary thrust (modified from Ujiie and Kimura (2014). The location of the seismic profile is shown on the map (C) (Ujiie and Kimura, 2014).

et al., 2014). Thompson and Grest (1991) established a relation between friction and dilatancy based on molecular-dynamics simulations of non-cohesive granular assemblies under shear. This study interpreted stick-slip behaviour as a consequence of repeated dilatancy and gravitational compaction and showed the importance of shear rate on the stability of sliding.

Both quartz and feldspar sand used in the subduction megathrust models have a non-spherical character. Their frictional behaviour (stick-slips) can thus be explained by dilation effects during shear. Velocity-weakening effects of feldspar sand in springslider experiments are larger. Feldspar and quartz sand show contradicting behaviour in springslider experiments and subduction zone megathrust models in terms of the size of friction drops. Experiments with quartz sand, produce larger friction drops in the springslider setup. In the subduction zone megathrust setup, on the other hand, feldspar wedges produce larger drops in loading force. To explain these differences, it is important to take both absolute friction and rate-and-state dependent decrease in friction into account.

An experimental study by Mair et al. (2002) shows the effects of angularity and grain size distribution on the frictional stability of fault gouges. More angular fault gouges enhance stable

sliding. This is consistent with springslider experiments in this study, since feldspar sand is more angular than quartz sand (Willingshofer et al., 2018). Experiments conducted by Mair et al. (2002), however, involve fault gouges confined between two solid steel plates and assume the presence of stress chains within the granular material. The experiments in this study always have one open boundary, and therefore the theory on stress chains might not apply. Frictional strength (Ikari et al., 2011) as well as basal surface roughness (Anthony and Marone, 2005) are also considered as important parameters in allowing frictional instabilities to occur. Faults with high surface roughness and high frictional strength are more prone to unstable behaviour. Feldspar shows higher frictional strength (Willingshofer et al., 2018) and higher basal surface roughness when used as basal decollement. This is consistent with larger instabilities in the subduction zone megathrust models with feldspar wedges. Angularity and frictional strength might cause competition in stable versus unstable sliding. The experimental setup might promote one or the other regime. A study of these effects is beyond the scope of this research but might be of interest.

Earthquakes in nature are more complex with respect to lab-scale earthquakes and are the result of a combination of physico-chemical processes operating at fault zones, which allow velocity-weakening, and the geometrical complexity of fault zones (Niemeijer et al., 2012). A detailed study on fault rocks in the Nankai accretionary wedge (Ujiie and Kimura, 2014) has shown that earthquake rupture can propagate to shallow depths by dynamic weakening. The weakening process is promoted by the presence of clay-rich fault gouges and occurs only during high slip rates (e.g. by thermal pressurization). During high slip rates, seismic slip can even occur in the initially velocity-strengthening regime. At low slip velocity, the fault only shows velocity-strengthening behaviour (Ujiie and Kimura, 2014). Although the mechanisms are different, it is believed that the models in this study also show velocity weakening at the wedge tip when large slip velocities are reached. A possible mechanism is the slip velocity dependence of the (a-b) value. This value might become more negative at higher slip velocities. Models with a small loadpoint velocity show larger coseismic slip velocities (see appendix D) and are believed to have lower basal friction during the slip. This is consistent with the geometry of the wedge (development of frontal thrusts rather than underthrusting; Malavieille, 2010). If the slip rate dependence additionally depends on the normal load, it could explain the segmentation of the wedge in an inner and outer part as suggested by Lohrmann et al. (2003). A larger reduction in strength ratio between the frictional strength at the basal decollement and the internal frictional strength of the wedge, would in that case occur in the inner wedge, whereas the outer wedge would show a smaller reduction in this ratio. Whether (a-b)-values are slip rate dependent under the experimental conditions remains a matter of speculation. The feldspar models show even higher slip velocities, but show underthrusting rather than frontal thrusting. Even though the velocity weakening effect might be larger for feldspar, producing larger friction drops, the average absolute basal friction might still be higher during slip, producing geometries, typical for high basal friction.

4.2.5 Limitations

A main advantage of analogue models is their respond under the exact same physics as the the natural prototype, if constructed correctly (Corbi et al., 2013). However, as mentioned before, there are a number of limitations concerning the monitoring techniques and material properties. First of all, the models in this study do not account for the presence of a temperature gradient, presence of fluids, and erosion or sedimentation. Numerical approaches (e.g. Van Dinther et al., 2013) are able to include these parameters in so-called seismo-thermo-mechanical models. In addition, the models in this study only focus on the upper $\sim$10 km and therefore do not consider viscous relaxation and

isostatic effects. Finally, the elastic moduli in the subduction megathrust models are not scaled to nature in order to keep frictional properties of the granular material unaffected.

However, the aim of this study is to understand the interplay of frictional behaviour and fault (re-)activation in the accretionary wedge. Simplified analogue models allow us to study these processes, given that limitations and simplifications are accounted for when interpreting the results.

Cameras used to monitor the experiments only allowed taking pre-seismic and postseismic images. Displacement fields obtained by PIV-analysis therefore only provide information on the total slip displacement of individual slips and do not give insights in the rupture dynamics of the model. The use of high-speed cameras could improve both the temporal and spatial monitoring resolution significantly. In addition, friction at the plexiglass boundaries causes shear during deformation, resulting in unrealistic deformation patterns near the boundaries of the model. This is problematic since monitoring of strain accumulation is only possible at the boundaries of the model. 3D imaging by high speed computer tomography could be used to overcome this problem.

4.3 Implications

The models in this study show the existence of a relation between frictional behaviour at the subduction megathrust fault and (1) the mean recurrence interval, size of earthquakes, and the variation in both, and consequently (2) the longer term deformation in the accretionary wedge. This is consistent with the dynamic Coulomb wedge theory (Wang and Hu, 2006) and previous analogue models (Rosenau et al., 2009). The geometry of the accretionary wedge may therefore be used to put constraints on the expected size of earthquakes in specific subduction zones. Simultaneously, the models in this study show that frictional behaviour varies over time. This implies that predictions of earthquake size and recurrence intervals based on the present seismic record are very uncertain for complex systems such as subduction zones.

Analysis of fault activity patterns shows the re-activation of the main splay fault and the alternating re-activation of frontal thrusts and backthrusts. Activation of these faults leads to vertical motions, which has implications for the generation of tsunamis (e.g. Van Zelst et al., 2019; Wendt et al., 2009). Splay faults are generally much steeper with respect to the subduction megathrust fault. Activity on splay faults is therefore believed to be important in the formation of tsunamis (van Zelst, 2020). Combined seismic cycle, dynamic rupture, and tsunami models shows that the activation of several splay faults leads to more surface displacements and consequently larger tsunami height (van Zelst et al., 2019). The alternating activity of frontal thrusts seen in the models of this study implies that tsunami height for a specific subduction zone might vary between individual earthquakes, depending on the number of faults which get reactivated.

4.4 Future research

As mentioned in the discussion, transient deformation patterns seen in nature (e.g. seaward motions of the overriding wedge) are not observed in the models of this study. This is e.g. a consequence of the high elastic bulk modulus of the granular materials used. Adding rubber grains to the wedge in future models, will improve the elastic response of the wedge. Secondly, observed slip sizes in the models of this study are at least one order of magnitude too large. This can simply be reduced by increasing the stiffness of the loading mechanism or by increasing the loadpoint velocity. This, however, also requires higher monitoring resolution.

For future studies, it is suggested to improve the elastic scaling of the model. This also requires the usage of a loadcell with a higher resolution, to observe smaller events. Additionally, high

speed cameras would allow to study the rupture propagation in the model. The required temporal resolution should be at least 10 Hz, in order to obtain several frames during one single event. Additional information on the state of stress in the accretionary wedge can be obtained by doing in-situ stress measurements (e.g. Nieuwland et al., 2000; Moulas et al., 2019). These techniques have proven to be successful in identifying changes of stress, associated with the formation of new thrust faults. It could therefore be used to link the formation of new faults to changes in the state of stress in the wedge and to subsequent variations in frictional behaviour. Finally, the slip rate dependence of the empirical constant (a-b) of quartz sand and feldspar sand at experimental conditions requires further investigation. By modifying the springslider experimental set-up (e.g. decreasing friction between the plexiglass box and basal decollement by using rollers) and by additional monitoring with high speed cameras and a velocity sensor, possible dynamic weakening mechanisms could be identified.

5 Conclusion

The interfaces between subduction plates and the associated overriding plate produce a large portion of the global seismic moment. The instrumental seismic record, however, shows large variations in behaviour between different subduction zones, varying from aseismic slip to very large earthquakes. Our knowledge on how frictional behaviour at the seismogenic zone and deformation in the overriding accretionary wedge are related, lacks due to a number of constraints, including the absence of direct observations on the seismogenic zone and the absence of a significantly long instrumental seismic record. Analogue modelling has proven to be a successful method in studying the relation between frictional behaviour at the plate interface and accretionary wedge geometries. In this study, analogue modelling is used to study the upper ~ 10 km of the subduction interface, and the accretionary wedge above it. The aim of this study is to better understand how rate and state friction affects the short term seismic cycle ($< 10^2$ years) and subsequently the deformation at tectonic time scales ($> 10^5$ years), and conversely how fault (re-) activation affects frictional behaviour at the subduction zone megathrust.

From the results in this study, we can conclude the following: (1) Frictional behaviour at the basal decollement is affected by loadpoint velocity. Force drop, slip size and recurrence time are inversely related to the loadpoint velocity. This short term difference in slip behaviour consequently affects the large scale permanent deformation in the accretionary wedge. Frontal thrusting is favourable at low loadpoint velocity, whereas underthrusting is more likely at high loadpoint velocity. (2) Frictional behaviour at the basal decollement as well as permanent deformation in the accretionary wedge are material dependent. Models consisting of a feldspar wedge show relatively large slips with respect to quartz models, indicating large velocity weakening effects. Permanent deformation patters of feldspar models are however indicative of high basal friction. (3) At the monitoring resolution in this study, no direct relation between individual fault activation and change in frictional behaviour is found. Ongoing accretion of material however seems to affect basal friction and size of the events over longer time scales. (4) 1D coseismic surface displacements of the models show fault re-activation of the main splay faults during every event. Frontal thrusts and backthrusts show alternating activity.

The results of this study have implications on hazard predictions for subduction zones. The relation between frictional behaviour and large scale deformation implicates that the geometry of the accretionary wedge may be used to put constraints on the expected size of earthquakes in specific subduction zones. The alternating activity of frontal thrusts seen in the models of this

study implies that tsunami height for a specific subduction zone might vary between individual earthquakes, depending on the number of faults which get reactivated.

To improve modelling results, it is recommended to use materials which are elastically better scaled to nature, and to include visco-elastic materials to account for viscous relaxation and isostatic responses. Monitoring can be improved by raising the temporal resolution of cameras in order to study the rupture dynamics of the model. Alternatively, high speed computer tomography could be used to obtain 3D subsequent deformation patterns.

6 Acknowledgements

I would like to thank Dr. Ernst Willingshofer and Dr. André Niemeijer for their supervision during my thesis. I would also like to thank them for their enthusiasm and the opportunity they gave me to present my work to a broader audience. Furthermore I would like to thank Marcel Arts for his technical support with building the experimental set-up. I would also like to thank Antoine Auzemery, Ylona van Dinther, Taco Broerse, and Suzanne Hangx for their ideas and suggestions during the thesis. Finally I would like to thank Manon Peek, Mark Willemse, and Siel Hoornaert for reviewing my thesis and the corresponding presentations.

References

Anthony, J. L. and Marone, C. (2005). Influence of particle characteristics on granular friction. *Journal of Geophysical Research: Solid Earth*, 110(B8).

Beeler, N., Hickman, S., and Wong, T.-f. (2001). Earthquake stress drop and laboratory-inferred interseismic strength recovery. *Journal of Geophysical Research: Solid Earth*, 106(B12):30701–30713.

Beer, M., Kougioumtzoglou, I. A., Patelli, E., and Au, S.-K. (2015). *Encyclopedia of earthquake engineering*. Springer.

Bookhagen, B., Echtler, H. P., Melnick, D., Strecker, M. R., and Spencer, J. Q. (2006). Using uplifted holocene beach berms for paleoseismic analysis on the santa maría island, south-central chile. *Geophysical Research Letters*, 33(15).

Brace, W. and Byerlee, J. (1966). Stick-slip as a mechanism for earthquakes. *Science*, 153(3739):990–992.

Brizzi, S., Sandri, L., Funiciello, F., Corbi, F., Piromallo, C., and Heuret, A. (2018). Multivariate statistical analysis to investigate the subduction zone parameters favoring the occurrence of giant megathrust earthquakes. *Tectonophysics*, 728:92–103.

Brizzi, S., van Zelst, I., Funiciello, F., Corbi, F., and van Dinther, Y. (2020). How sediment thickness influences subduction dynamics and seismicity. *Journal of Geophysical Research: Solid Earth*, 125(8):e2019JB018964.

Brun, J.-P. (1999). Narrow rifts versus wide rifts: inferences for the mechanics of rifting from laboratory experiments. *Philosophical Transactions of the Royal Society of London. Series A: Mathematical, Physical and Engineering Sciences*, 357(1753):695–712.

Brun, J.-P. (2002). Deformation of the continental lithosphere: Insights from brittle-ductile models. *Geological Society, London, Special Publications*, 200(1):355–370.

Burg, J.-P. (2016). Driving mechanisms of thrust systems, dynamics of accretionary, orogenic wedge.

Byerlee, J. (1978). Friction of rocks. In *Rock friction and earthquake prediction*, pages 615–626. Springer.

Corbi, F., Funiciello, F., Moroni, M., Van Dinther, Y., Mai, P. M., Dalguer, L., and Faccenna, C. (2013). The seismic cycle at subduction thrusts: 1. insights from laboratory models. *Journal of Geophysical Research: Solid Earth*, 118(4):1483–1501.

Coulomb, C. (1776). Essai sur une application des rèles des maximis et minimis a quelques problems de statique. *Memoires Acad. Royale des Sciences*, 7.

Dahlen, F. (1984). Noncohesive critical coulomb wedges: An exact solution. *Journal of Geophysical Research: Solid Earth*, 89(B12):10125–10133.

Dahlen, F. (1990). Critical taper model of fold-and-thrust belts and accretionary wedges. *Annual Review of Earth and Planetary Sciences*, 18(1):55–99.

Dahlen, F., Suppe, J., and Davis, D. (1984). Mechanics of fold-and-thrust belts and accretionary wedges: Cohesive coulomb theory. *Journal of Geophysical Research: Solid Earth*, 89(B12):10087–10101.

Davis, D., Suppe, J., and Dahlen, F. (1983). Mechanics of fold-and-thrust belts and accretionary wedges. *Journal of Geophysical Research: Solid Earth*, 88(B2):1153–1172.

Dieterich, J. H. (1972). Time-dependent friction in rocks. *Journal of Geophysical Research*, 77(20):3690–3697.

Dotare, T., Yamada, Y., Adam, J., Hori, T., and Sakaguchi, H. (2016). Initiation of a thrust fault revealed by analog experiments. *Tectonophysics*, 684:148–156.

Govers, R., Furlong, K. P., Van de Wiel, L., Herman, M., and Broerse, T. (2018). The geodetic signature of the earthquake cycle at subduction zones: Model constraints on the deep processes. *Reviews of Geophysics*, 56(1):6–49.

Hamada, Y., Sakaguchi, A., Tanikawa, W., Yamaguchi, A., Kameda, J., and Kimura, G. (2015). Estimation of slip rate and fault displacement during shallow earthquake rupture in the nankai subduction zone. *Earth, Planets and Space*, 67(1):39.

He, C., Wong, T.-f., and Beeler, N. M. (2003). Scaling of stress drop with recurrence interval and loading velocity for laboratory-derived fault strength relations. *Journal of Geophysical Research: Solid Earth*, 108(B1).

Hubbert, M. K. (1937). Theory of scale models as applied to the study of geologic structures. *Bulletin of the Geological Society of America*, 48(10):1459–1520.

Ikari, M. J., Marone, C., and Saffer, D. M. (2011). On the relation between fault strength and frictional stability. *Geology*, 39(1):83–86.

Jaeger, J., Cook, N., and Zimmerman, R. (1979). Rock mechanics. *Fundamentals of Rock Mechanics*.

Klinkmüller, M., Schreurs, G., Rosenau, M., and Kemnitz, H. (2016). Properties of granular analogue model materials: A community wide survey. *Tectonophysics*, 684:23–38.

Kodaira, S., Takahashi, N., Nakanishi, A., Miura, S., and Kaneda, Y. (2000). Subducted seamount imaged in the rupture zone of the 1946 nankaido earthquake. *Science*, 289(5476):104–106.

Krantz, R. W. (1991). Measurements of friction coefficients and cohesion for faulting and fault reactivation in laboratory models using sand and sand mixtures. *Tectonophysics*, 188(1-2):203–207.

Lohrmann, J., Kukowski, N., Adam, J., and Oncken, O. (2003). The impact of analogue material properties on the geometry, kinematics, and dynamics of convergent sand wedges. *Journal of Structural Geology*, 25(10):1691–1711.

Mair, K., Frye, K. M., and Marone, C. (2002). Influence of grain characteristics on the friction of granular shear zones. *Journal of Geophysical Research: Solid Earth*, 107(B10):ECV–4.

Malavieille, J. (2010). Impact of erosion, sedimentation, and structural heritage on the structure and kinematics of orogenic wedges: Analog models and case studies. *Gsa Today*, 20(1):4–10.

Marone, C., Raleigh, C. B., and Scholz, C. (1990). Frictional behavior and constitutive modeling of simulated fault gouge. *Journal of Geophysical Research: Solid Earth*, 95(B5):7007–7025.

Marone, C. and Saffer, D. M. (2007). Fault friction and the upper transition from seismic to aseismic faulting. *The seismogenic zone of subduction thrust faults*, pages 346–369.

Marone, C. and Scholz, C. (1988). The depth of seismic faulting and the upper transition from stable to unstable slip regimes. *Geophysical Research Letters*, 15(6):621–624.

McCaffrey, R. (2008). Global frequency of magnitude 9 earthquakes. *Geology*, 36(3):263–266.

Mohr, O. (1900). Welche umstände bedingen die elastizitätsgrenze und den bruch eines materials. *Zeitschrift des Vereins Deutscher Ingenieure*, 46(1524-1530):1572–1577.

Moore, G., Park, J., Bangs, N., Gulick, S., Tobin, H., Nakamura, Y., Sato, S., Tsuji, T., Yoro, T., Tanaka, H., et al. (2009). Structural and seismic stratigraphic framework of the nantroseize stage 1 transect. In *Proc. IODP— Volume*, volume 314, page 2.

Moore, G. F., Saffer, D., Studer, M., and Pisani, P. C. (2011). Structural restoration of thrusts at the toe of the nankai trough accretionary prism off shikoku island, japan: Implications for dewatering processes. *Geochemistry, Geophysics, Geosystems*, 12(5).

Moulas, E., Sokoutis, D., and Willingshofer, E. (2019). Pressure build-up and stress variations within the earth's crust in the light of analogue models. *Scientific reports*, 9(1):1–8.

Niemeijer, A., Di Toro, G., Griffith, W. A., Bistacchi, A., Smith, S. A., and Nielsen, S. (2012). Inferring earthquake physics and chemistry using an integrated field and laboratory approach. *Journal of Structural Geology*, 39:2–36.

Niemeijer, A. and Spiers, C. (2006). Velocity dependence of strength and healing behaviour in simulated phyllosilicate-bearing fault gouge. *Tectonophysics*, 427(1-4):231–253.

Nieuwland, D. A., Urai, J. L., and Knoop, M. (2000). In-situ stress measurements in model experiments of tectonic faulting. In *Aspects of Tectonic Faulting*, pages 155–166. Springer.

Pacheco, J. F. and Sykes, L. R. (1992). Seismic moment catalog of large shallow earthquakes, 1900 to 1989. *Bulletin of the Seismological Society of America*, 82(3):1306–1349.

Pacheco, J. F., Sykes, L. R., and Scholz, C. H. (1993). Nature of seismic coupling along simple plate boundaries of the subduction type. *Journal of Geophysical Research: Solid Earth*, 98(B8):14133–14159.

Platt, J., Leggett, J., Young, J., Raza, H., and Alam, S. (1985). Large-scale sediment underplating in the makran accretionary prism, southwest pakistan. *Geology*, 13(7):507–511.

Reid, H. F. (1910). The mechanics of the earthquake. *The California Earthquake of April 18, 1906, Report of the State Earthquake Investigation Commission*.

Reynolds, O. (1886). Experiments showing dilatancy, a property of granular material, possibly connected with gravitation. *Proc. R. Inst. GB*, 11(354363):12.

Rosenau, M., Corbi, F., and Dominguez, S. (2017). Analogue earthquakes and seismic cycles: experimental modelling across timescales.

Rosenau, M., Corbi, F., Dominguez, S., Rudolf, M., Ritter, M. C., and Pipping, E. (2016). Supplement to" analogue earthquakes and seismic cycles: Experimental modelling across timescales".

Rosenau, M., Lohrmann, J., and Oncken, O. (2009). Shocks in a box: An analogue model of subduction earthquake cycles with application to seismotectonic forearc evolution. *Journal of Geophysical Research: Solid Earth*, 114(B1).

Rosenau, M., Nerlich, R., Brune, S., and Oncken, O. (2010). Experimental insights into the scaling and variability of local tsunamis triggered by giant subduction megathrust earthquakes. *Journal of Geophysical Research: Solid Earth*, 115(B9).

Ruh, J. B., Gerya, T., and Burg, J.-P. (2014). 3d effects of strain vs. velocity weakening on deformation patterns in accretionary wedges. *Tectonophysics*, 615:122–141.

Satake, K. and Atwater, B. F. (2007). Long-term perspectives on giant earthquakes and tsunamis at subduction zones. *Annu. Rev. Earth Planet. Sci.*, 35:349–374.

Scholz, C. H. (1990). Earthquakes as chaos. *Nature*, 348(6298):197–198.

Scholz, C. H. (1998). Earthquakes and friction laws. *Nature*, 391(6662):37–42.

Scholz, C. H. (2019). *The Mechanics of Earthquakes and Faulting*. Cambridge University Press, 3 edition.

Schwartz, S. Y. and Rokosky, J. M. (2007). Slow slip events and seismic tremor at circum-pacific subduction zones. *Reviews of Geophysics*, 45(3).

Shimazaki, K. and Nakata, T. (1980). Time-predictable recurrence model for large earthquakes. *Geophysical Research Letters*, 7(4):279–282.

Stesky, R., Brace, W., Riley, D., and Robin, P.-Y. (1974). Friction in faulted rock at high temperature and pressure. *Tectonophysics*, 23(1-2):177–203.

Thielicke, W. and Stamhuis, E. (2014). Pivlab – towards user-friendly, affordable and accurate digital particle image velocimetry in matlab. journal of open research software 2(1):e30.

Thompson, P. A. and Grest, G. S. (1991). Granular flow: friction and the dilatancy transition. *Physical Review Letters*, 67(13):1751.

Ujiie, K. and Kimura, G. (2014). Earthquake faulting in subduction zones: insights from fault rocks in accretionary prisms. *Progress in Earth and Planetary Science*, 1(1):7.

Van Dinther, Y., Gerya, T., Dalguer, L., Mai, P. M., Morra, G., and Giardini, D. (2013). The seismic cycle at subduction thrusts: Insights from seismo-thermo-mechanical models. *Journal of Geophysical Research: Solid Earth*, 118(12):6183–6202.

van Zelst, I. (2020). *Tsunamigenic earthquakes from tectonics to dynamic rupture*. PhD thesis, ETH Zurich.

Van Zelst, I., Wollherr, S., Gabriel, A.-A., Madden, E. H., and van Dinther, Y. (2019). Modeling megathrust earthquakes across scales: One-way coupling from geodynamics and seismic cycles to dynamic rupture. *Journal of Geophysical Research: Solid Earth*, 124(11):11414–11446.

van Zelst, I., Wollherr, S., Gabriel, A.-A., and van Dinther, Y. (2019). Complex splay fault rupture and its effect on seafloor displacements. In *Geophysical Research Abstracts*, volume 21.

Wang, K. (2007). Elastic and viscoelastic models of crustal deformation in subduction earthquake cycles. *The seismogenic zone of subduction thrust faults*, pages 540–575.

Wang, K. and Hu, Y. (2006). Accretionary prisms in subduction earthquake cycles: The theory of dynamic coulomb wedge. *Journal of Geophysical Research: Solid Earth*, 111(B6).

Wegner, S., Stannarius, R., Boese, A., Rose, G., Szabo, B., Somfai, E., and Börzsönyi, T. (2014). Effects of grain shape on packing and dilatancy of sheared granular materials. *Soft Matter*, 10(28):5157–5167.

Wendt, J., Oglesby, D. D., and Geist, E. L. (2009). Tsunamis and splay fault dynamics. *Geophysical Research Letters*, 36(15).

Willingshofer, E., Sokoutis, D., and Burg, J.-P. (2005). Lithospheric-scale analogue modelling of collision zones with a pre-existing weak zone. *Geological Society, London, Special Publications*, 243(1):277–294.

Willingshofer, E., Sokoutis, D., Kleinhans, M., Beekmann, F., Schönebeck, J.-M., Warsitzka, M., Marra, W., Braat, L., Baar, A., and Kleinhans, M. (2018). Ring-shear test data of plastic sand, a new rock analogue material used for experimental earth science applications at utrecht university.

7 Appendix

A Results parametric study springslider experiments

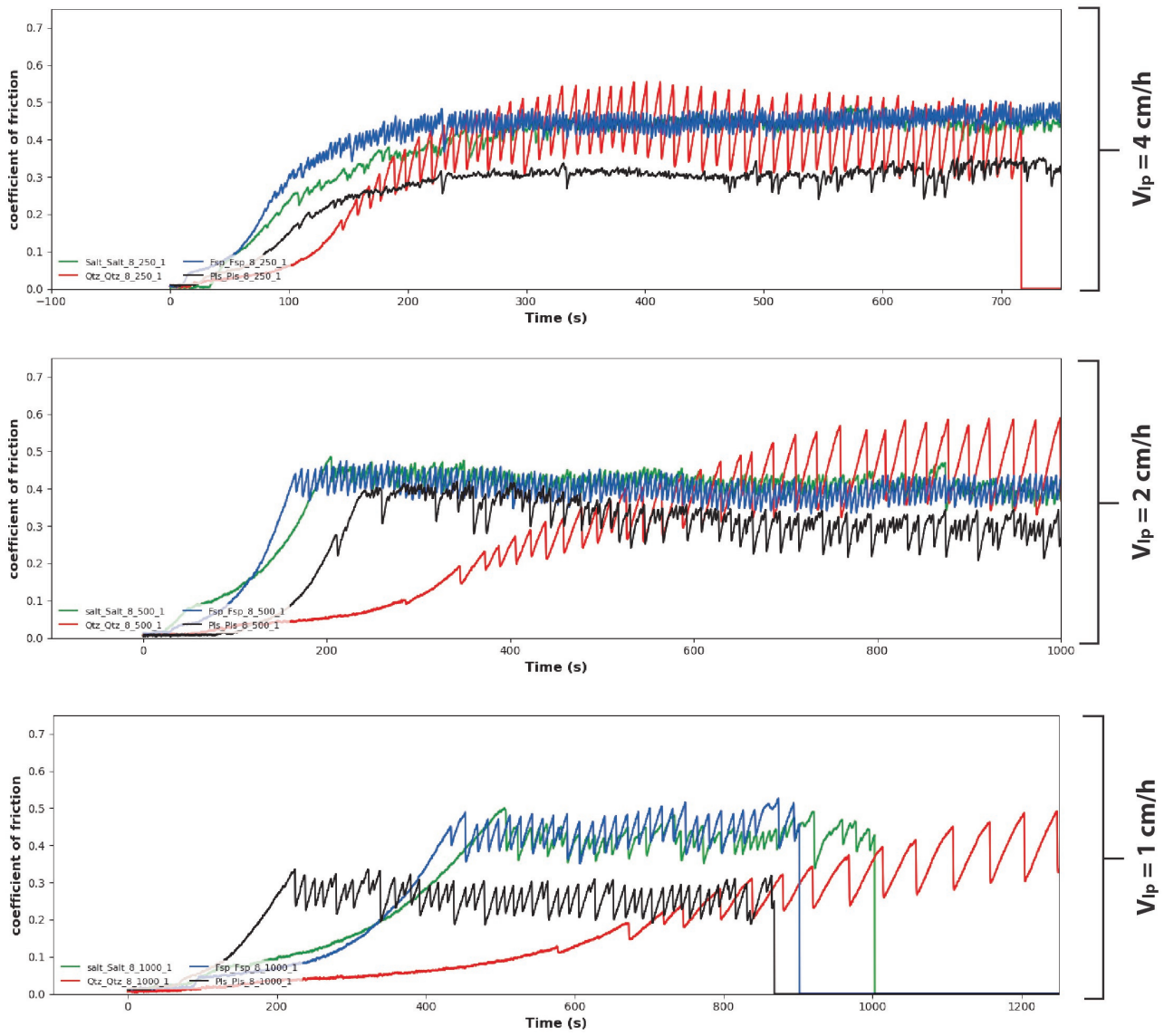

Figure 20: Frictional behaviour in springslider experiments with basal decollement consisting of unconsolidated granular material. The material at the decollement is the same as in the plexiglass box. Loadpoint velocity and type of material are varied (red = quartz sand, blue = feldspar sand, black = plastic sand, and green = granular salt.

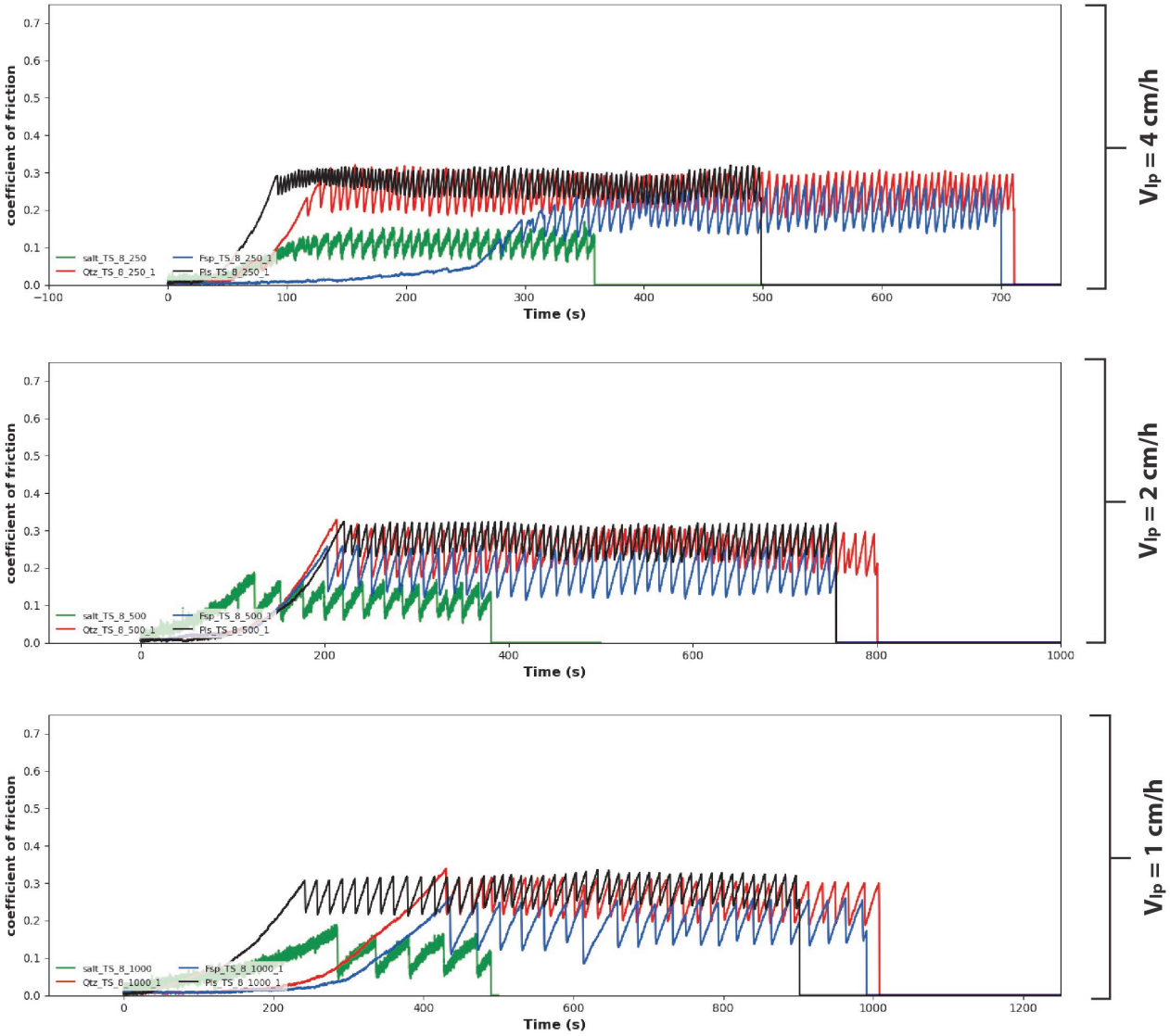

Figure 21: Frictional behaviour in springslider experiments with basal decollement consisting plastic sheet. Loadpoint velocity and type of material are varied (red = quartz sand, blue = feldspar sand, black = plastic sand, and green = granular salt.

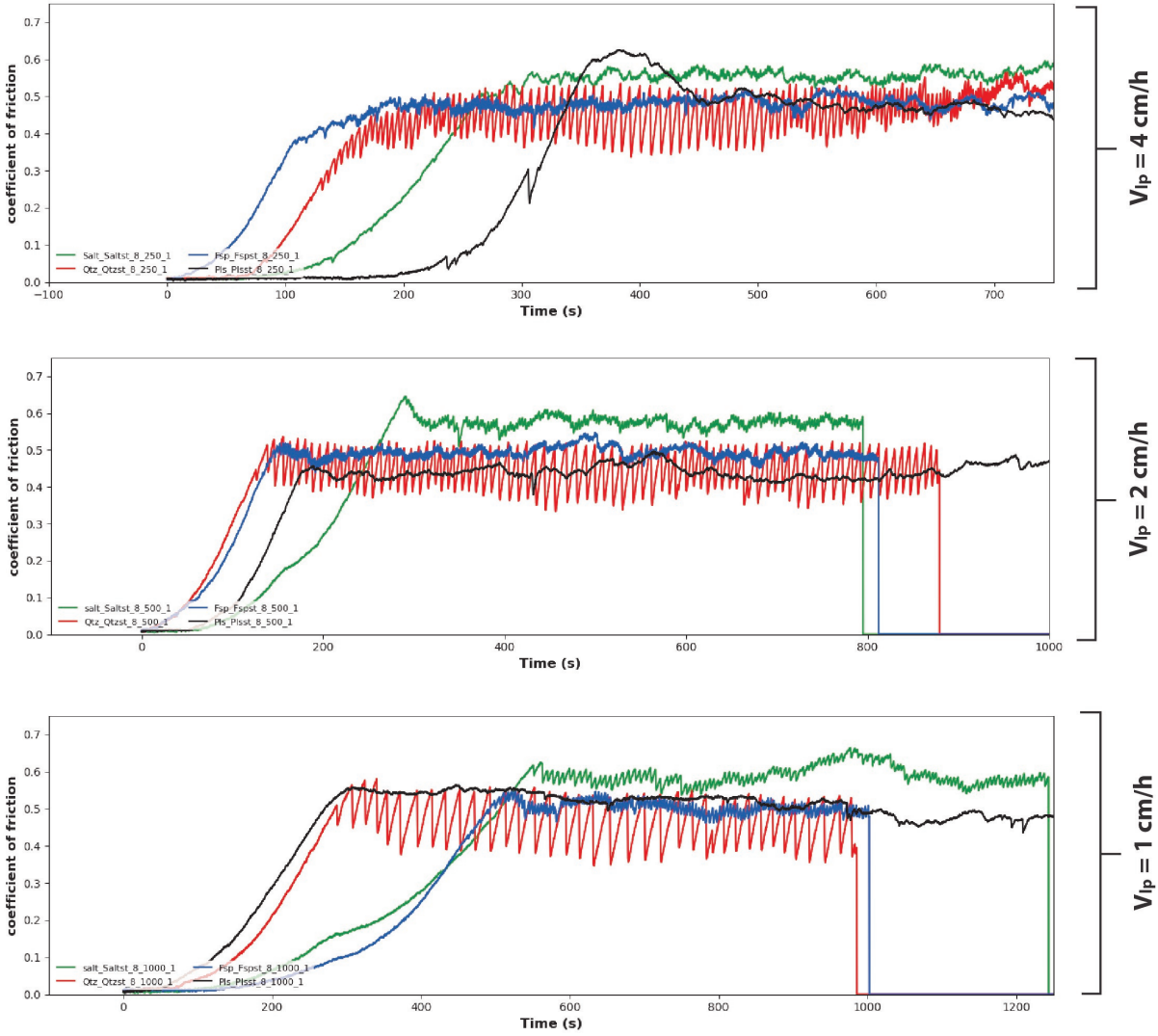

Figure 22: Frictional behaviour in springslider experiments with basal decollement consisting of granular material glued to a plastic sheet. The glued material at the decollement is the same material as in the plexiglass box. Loadpoint velocity and type of material are varied (red = quartz sand, blue = feldspar sand, black = plastic sand, and green = granular salt.

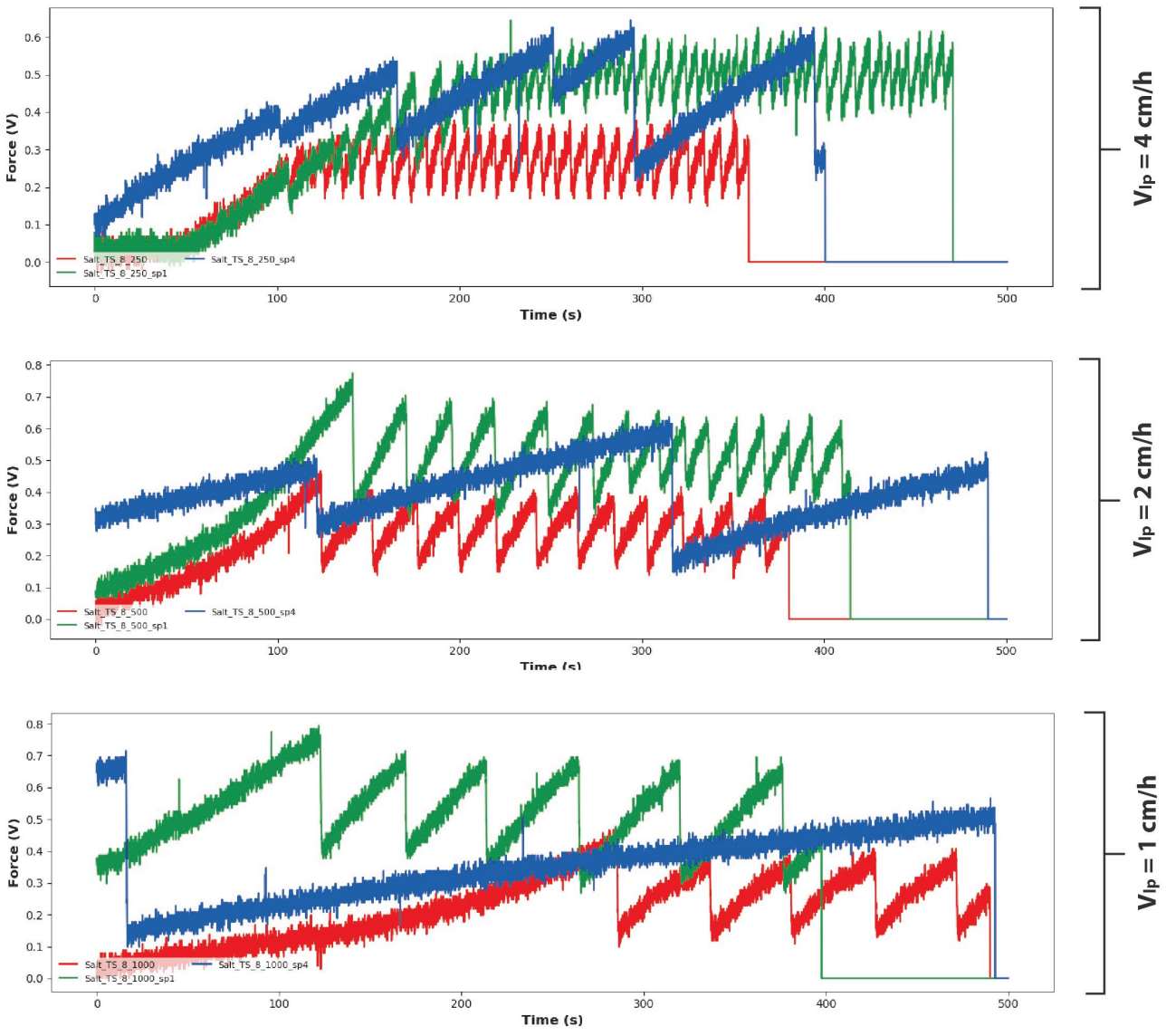

Figure 23: Frictional behaviour of granular salt in springslider experiments with basal decollement consisting of plastic sheet. Loadpoint velocity and spring constant are varied: blue = small spring constant, green = intermediate spring constant, red = large spring constant. Note that the vertical axis shows the loading force in volt (output of loadcell).

B Force vs Time

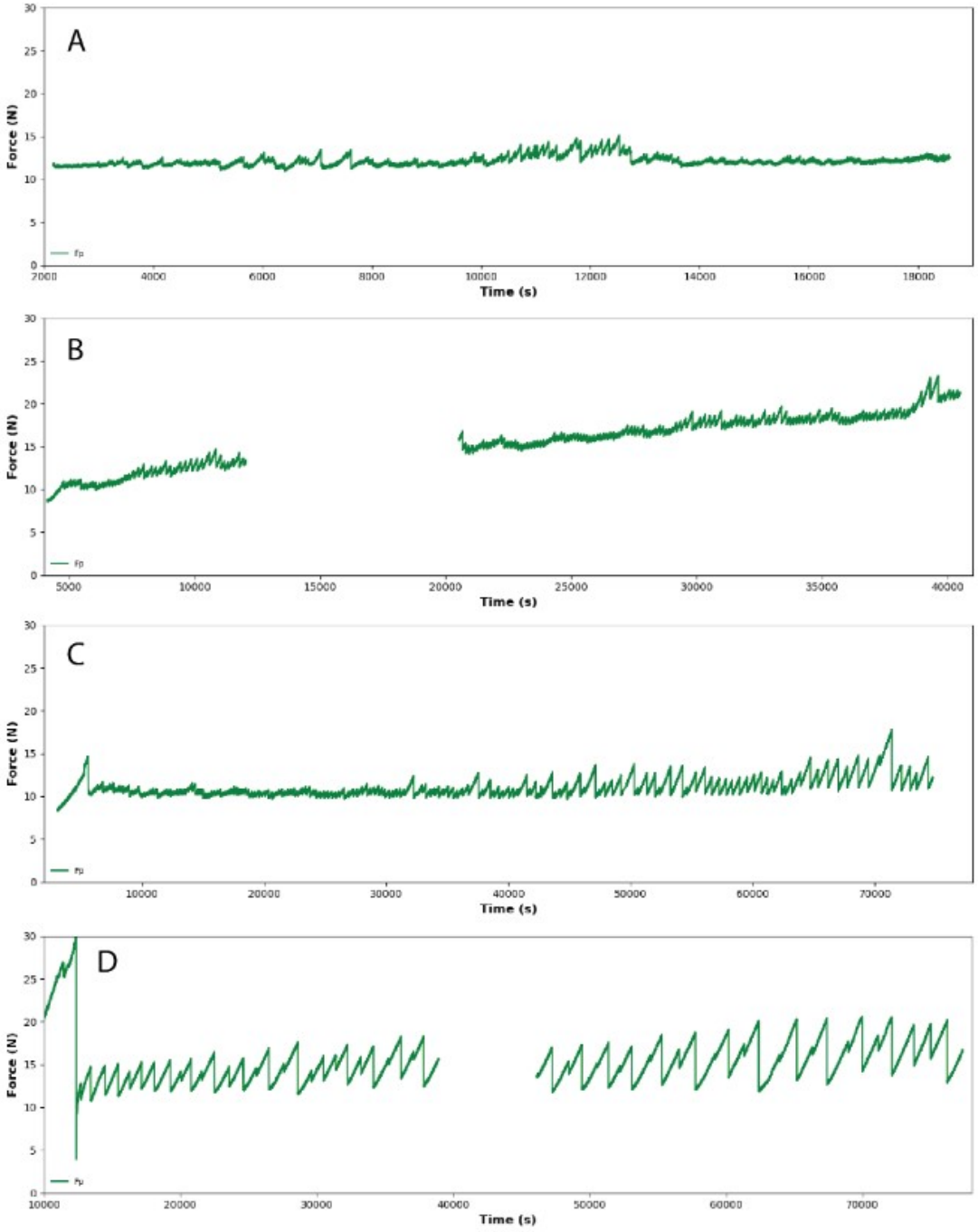

Figure 24: loading force calculated from load cell output signal for (A) granular material = quartz, loadpoint velocity = 4 cm/hr, (B) granular material = quartz, loadpoint velocity = 2 cm/hr, (C) granular material = quartz, loadpoint velocity = 1 cm/hr, and (D) granular material = feldspar, loadpoint velocity = 1 cm/hr. Note the different scales of the horizontal axes

C Displacement vs Time

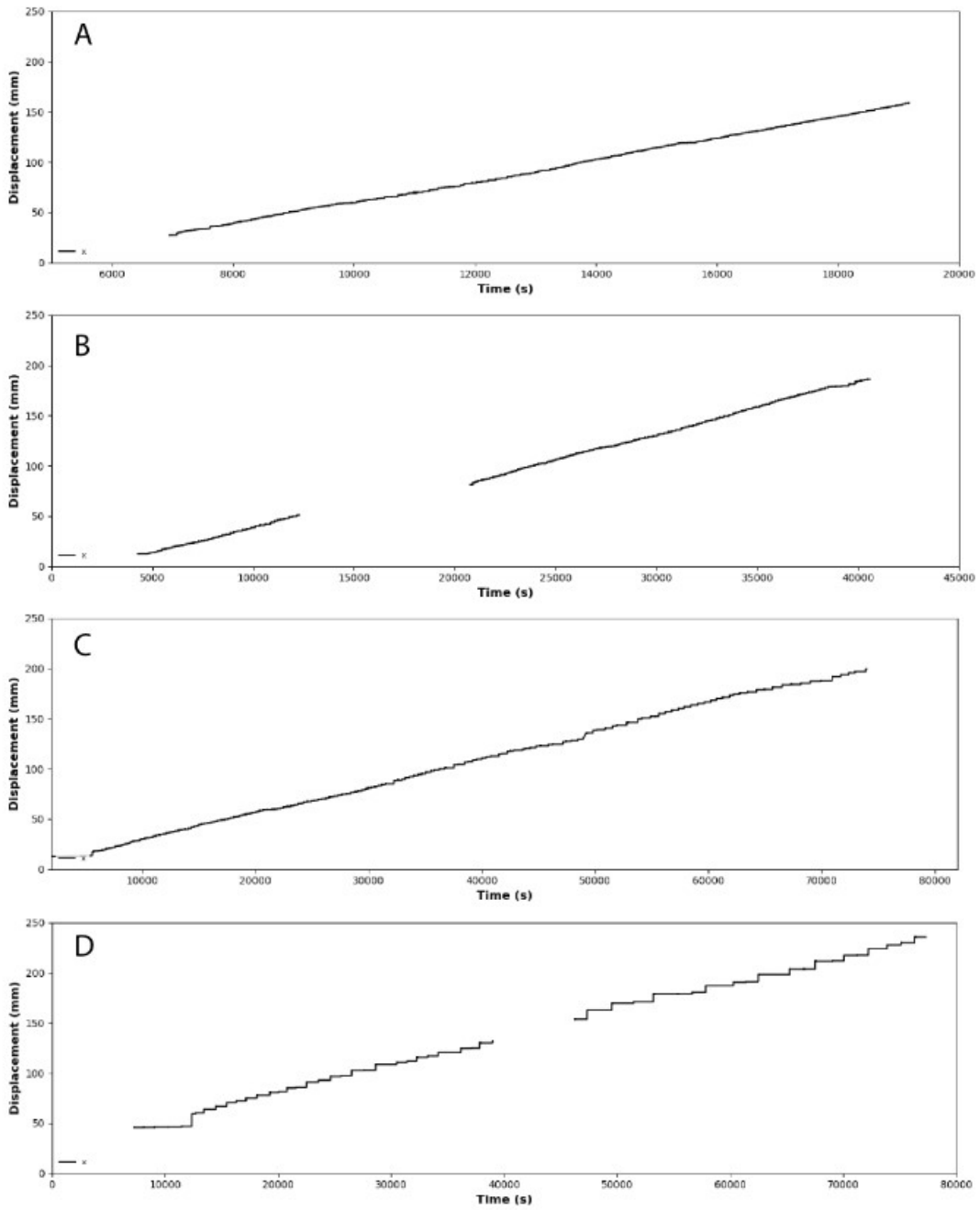

Figure 25: Accumulative displacement of the downgoing plate, calculated from velocity meter for (A) granular material = quartz, loadpoint velocity = 4 cm/hr, (B) granular material = quartz, loadpoint velocity = 2 cm/hr, (C) granular material = quartz, loadpoint velocity = 1 cm/hr, and (D) granular material = feldspar, loadpoint velocity = 1 cm/hr. Note the different scales of the horizontal axes

D Velocity vs Time

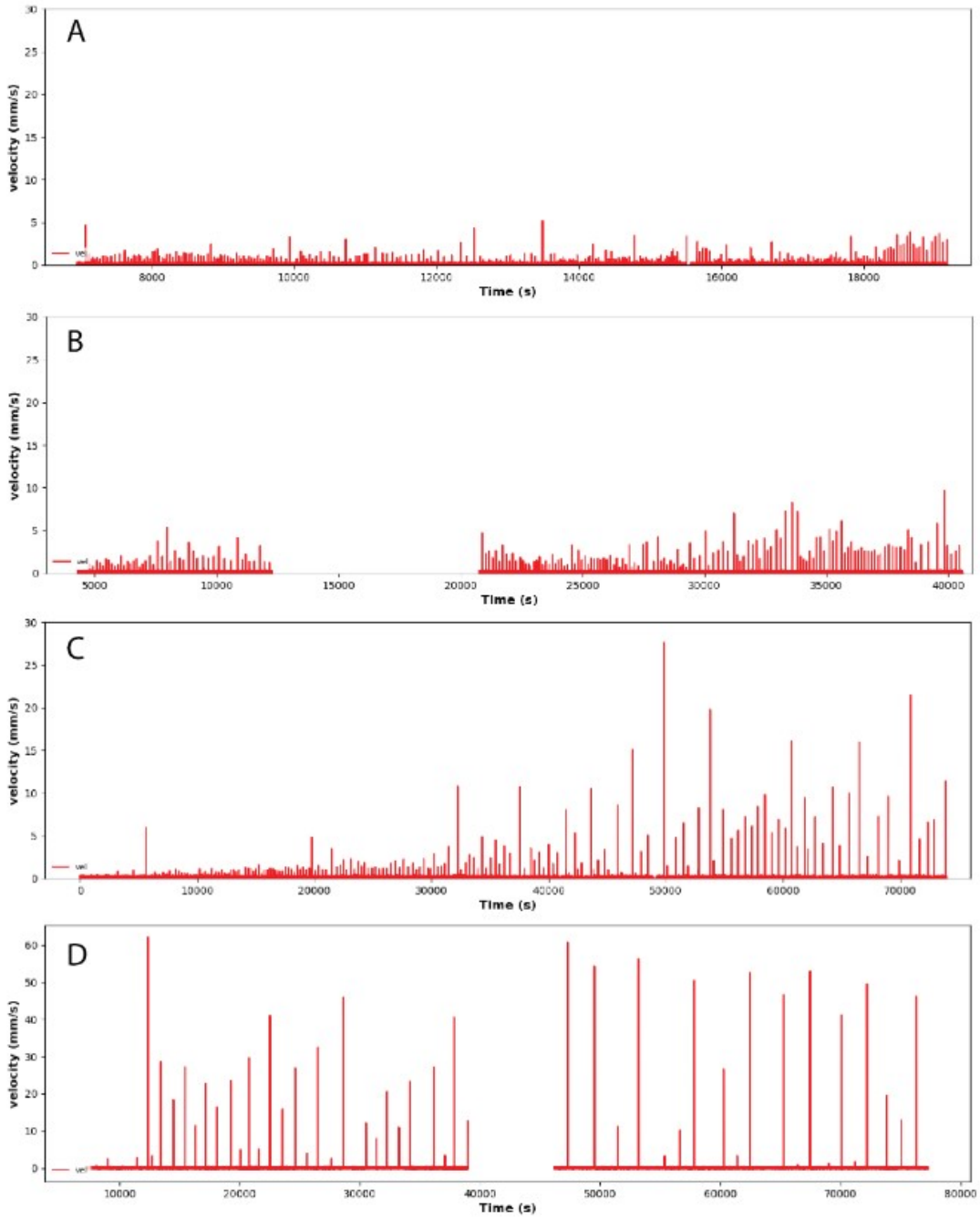

Figure 26: Velocity of the downgoing plate, calculated as time derivative from accumulative displacement, for (A) granular material = quartz, loadpoint velocity = 4 cm/hr, (B) granular material = quartz, loadpoint velocity = 2 cm/hr, (C) granular material = quartz, loadpoint velocity = 1 cm/hr, and (D) granular material = feldspar, loadpoint velocity = 1 cm/hr. Note the different scales of the horizontal axes

E Permanent deformation

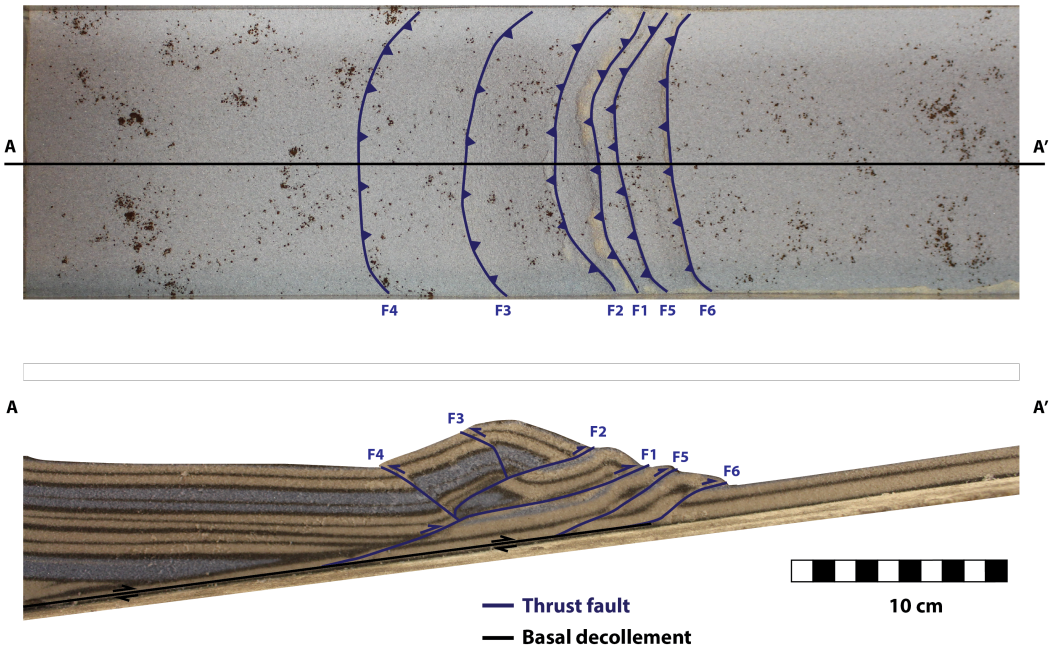

Figure 27: final permanent deformation in model Qtz-4. The upper and lower figure show final permanent deformation in top view and cross-section respectively.

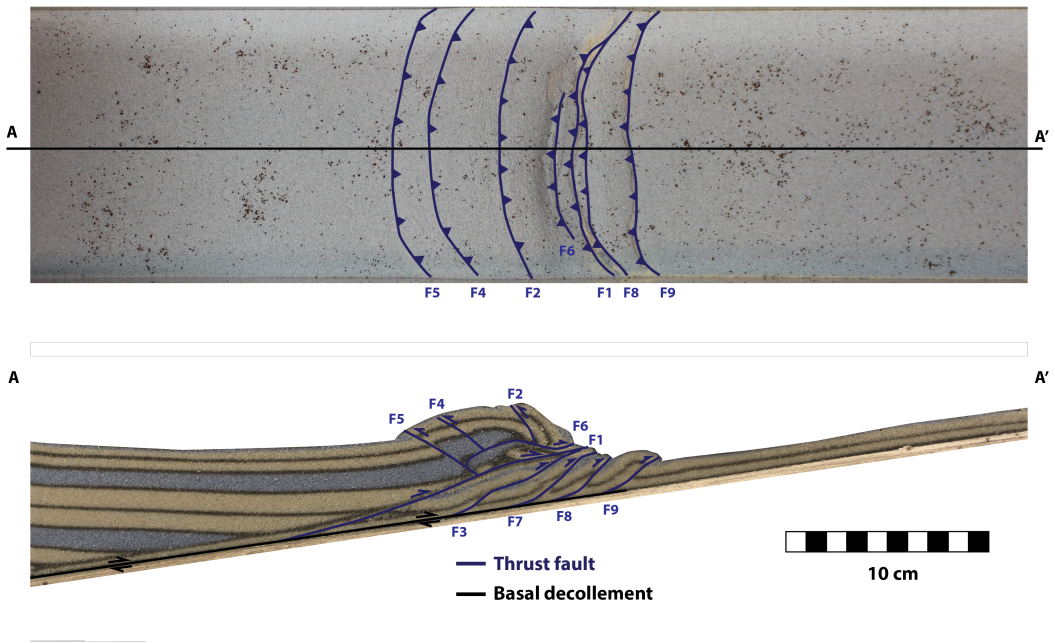

Figure 28: final permanent deformation in model Qtz-2. The upper and lower figure show final permanent deformation in top view and cross-section respectively.

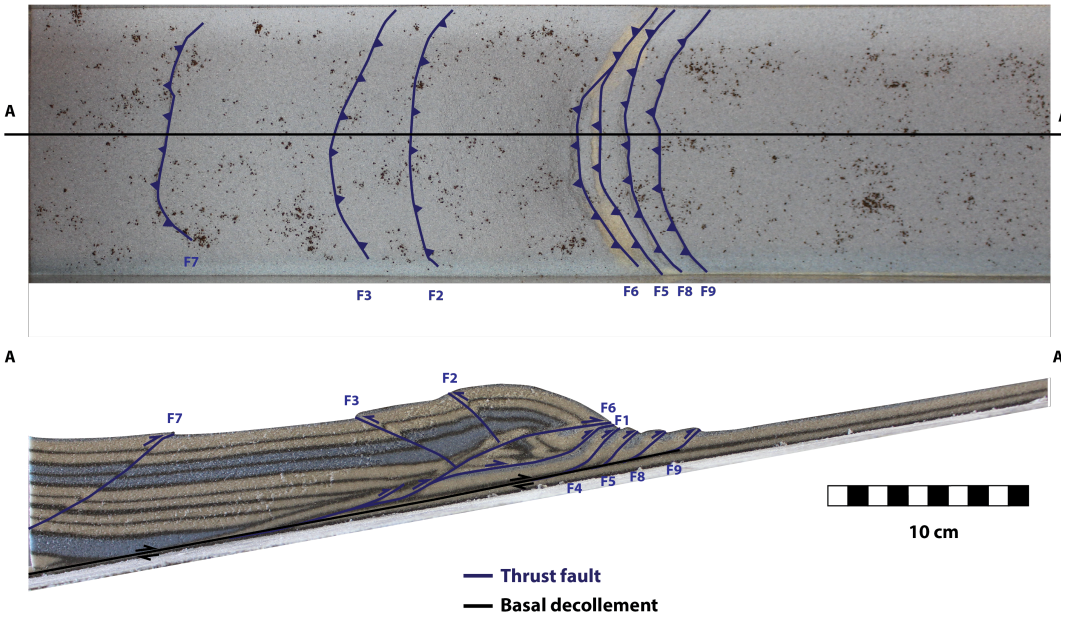

Figure 29: final permanent deformation in model Qtz-1. The upper and lower figure show final permanent deformation in top view and cross-section respectively.

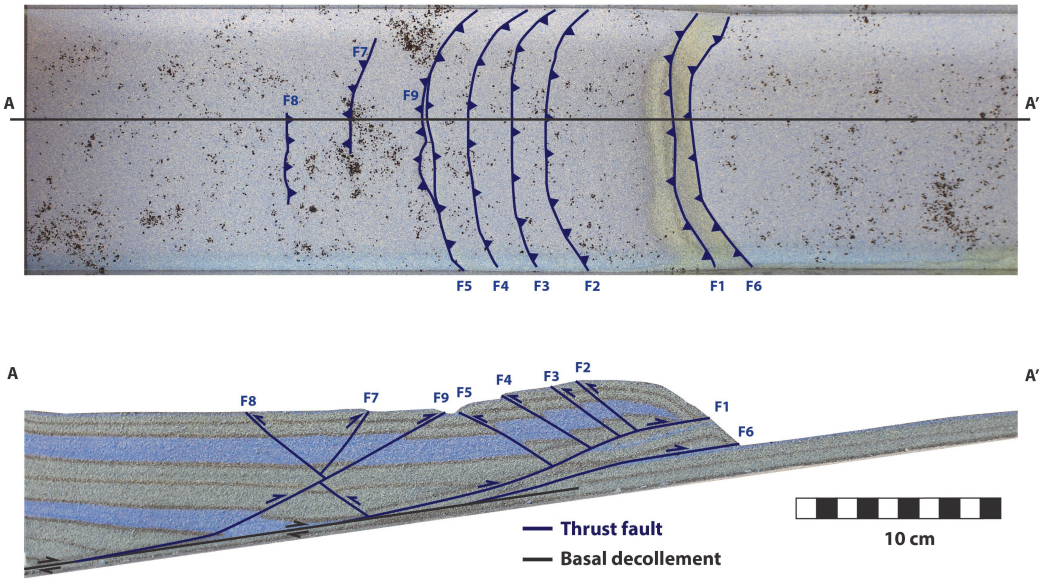

Figure 30: final permanent deformation in model Fsp-1. The upper and lower figure show final permanent deformation in top view and cross-section respectively.

F PIV analysis top view photographs

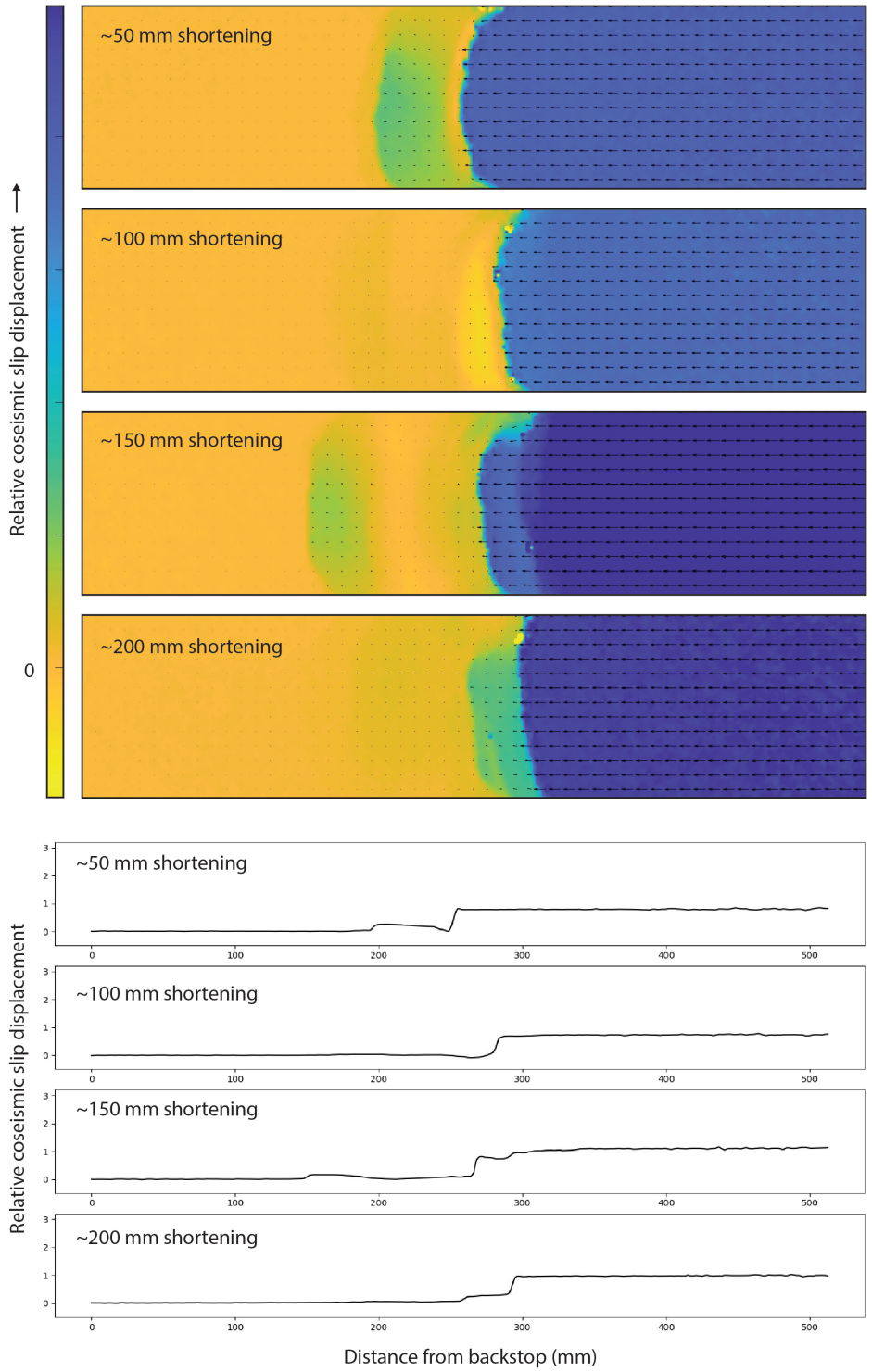

Figure 31: Top view PIV analysis of model Qtz-4. Coloured images show 2D relative coseismic slip displacements at 50, 100, 150, and 200 mm shortening. The graphs show corresponding 1D coseismic slip displacements, at a section running from left to right over the top view images

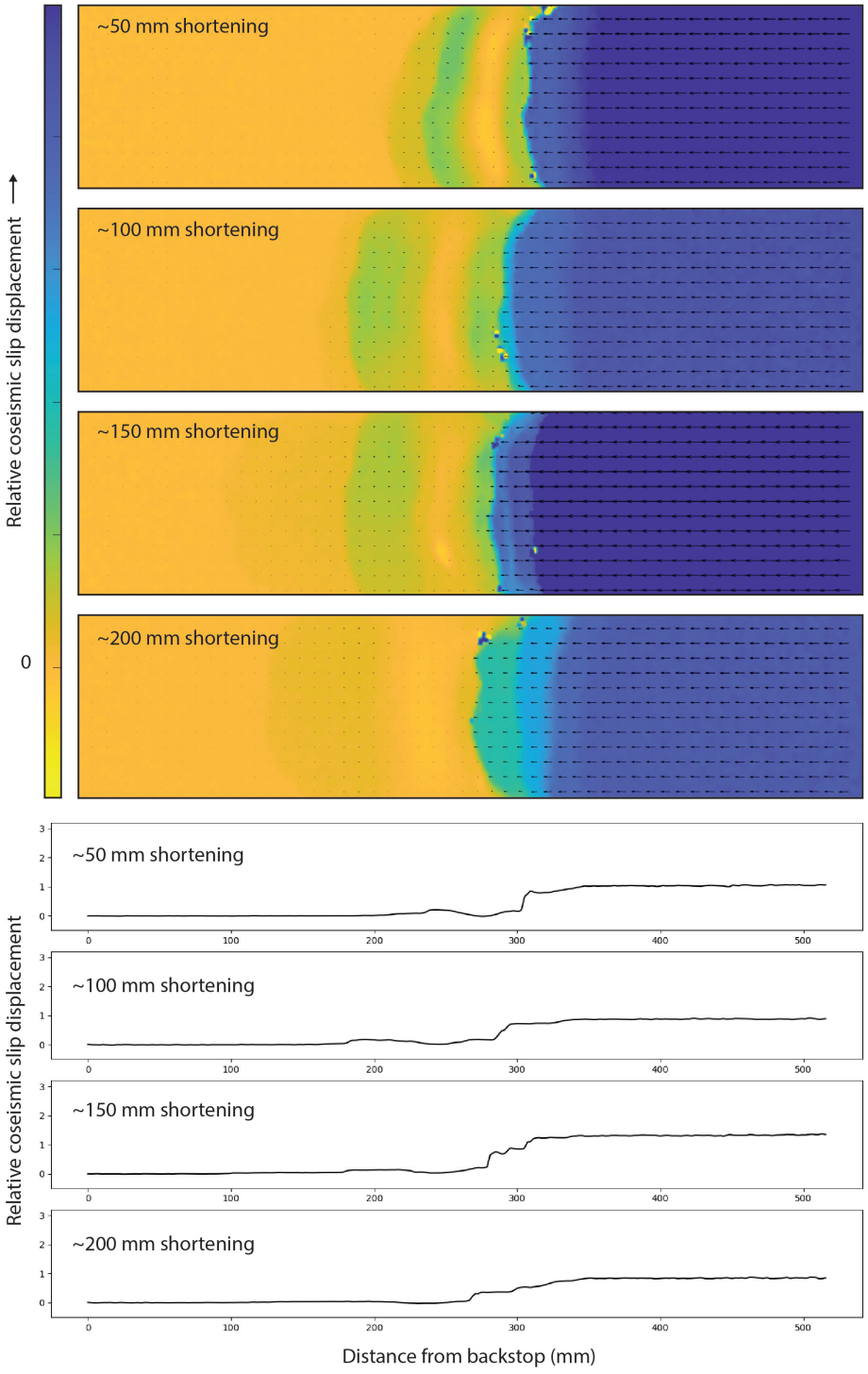

Figure 32: Top view PIV analysis of model Qtz-2. Coloured images show 2D relative coseismic slip displacements at 50, 100, 150, and 200 mm shortening. The graphs show corresponding 1D coseismic slip displacements, at a section running from left to right over the top view images

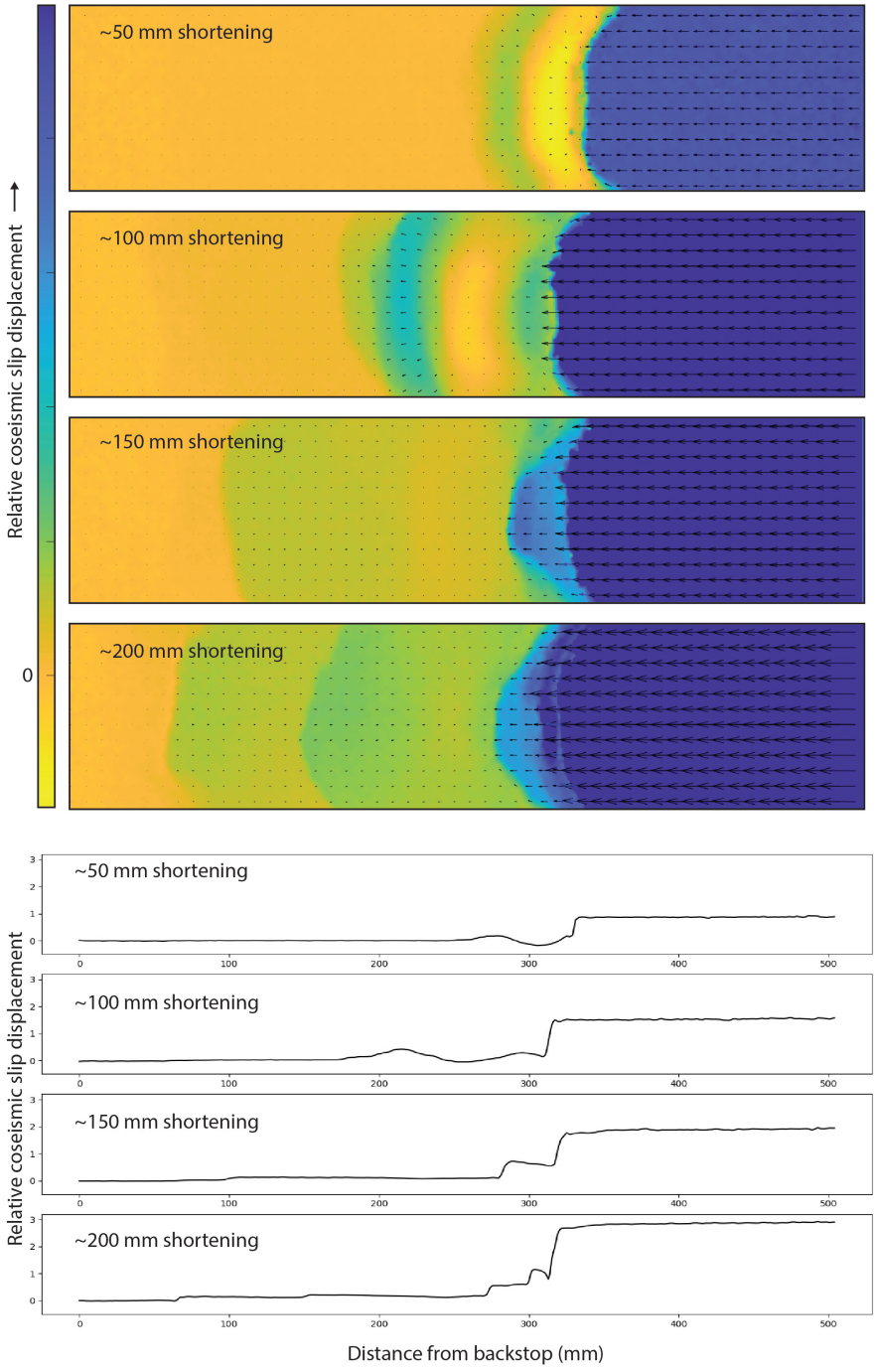

Figure 33: Top view PIV analysis of model Qtz-1. Coloured images show 2D relative coseismic slip displacements at 50, 100, 150, and 200 mm shortening. The graphs show corresponding 1D coseismic slip displacements, at a section running from left to right over the top view images

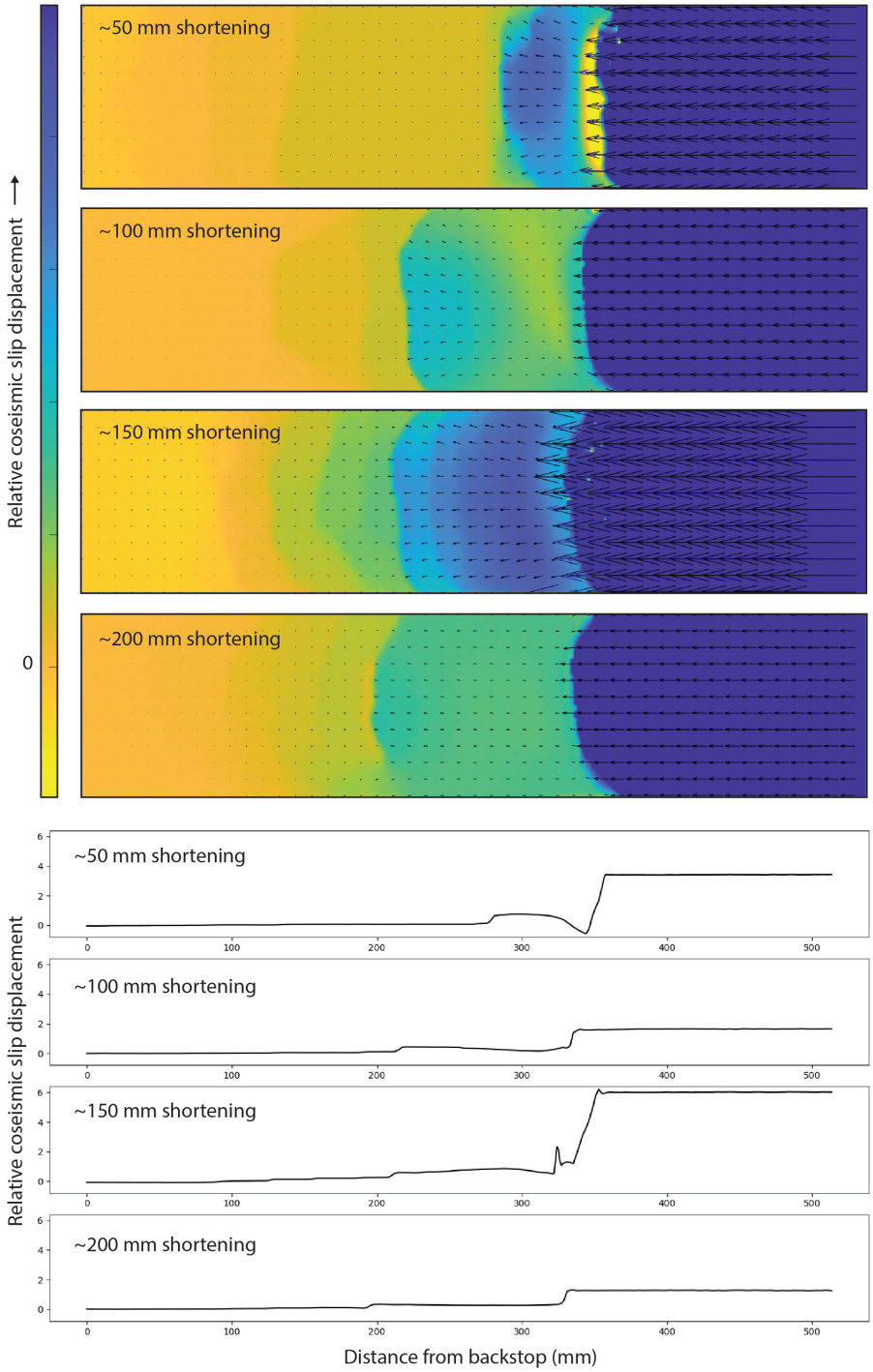

Figure 34: Top view PIV analysis of model Fsp-1. Coloured images show 2D relative coseismic slip displacements at 50, 100, 150, and 200 mm shortening. The graphs show corresponding 1D coseismic slip displacements, at a section running from left to right over the top view images

G 1D-coseismic slip displacement

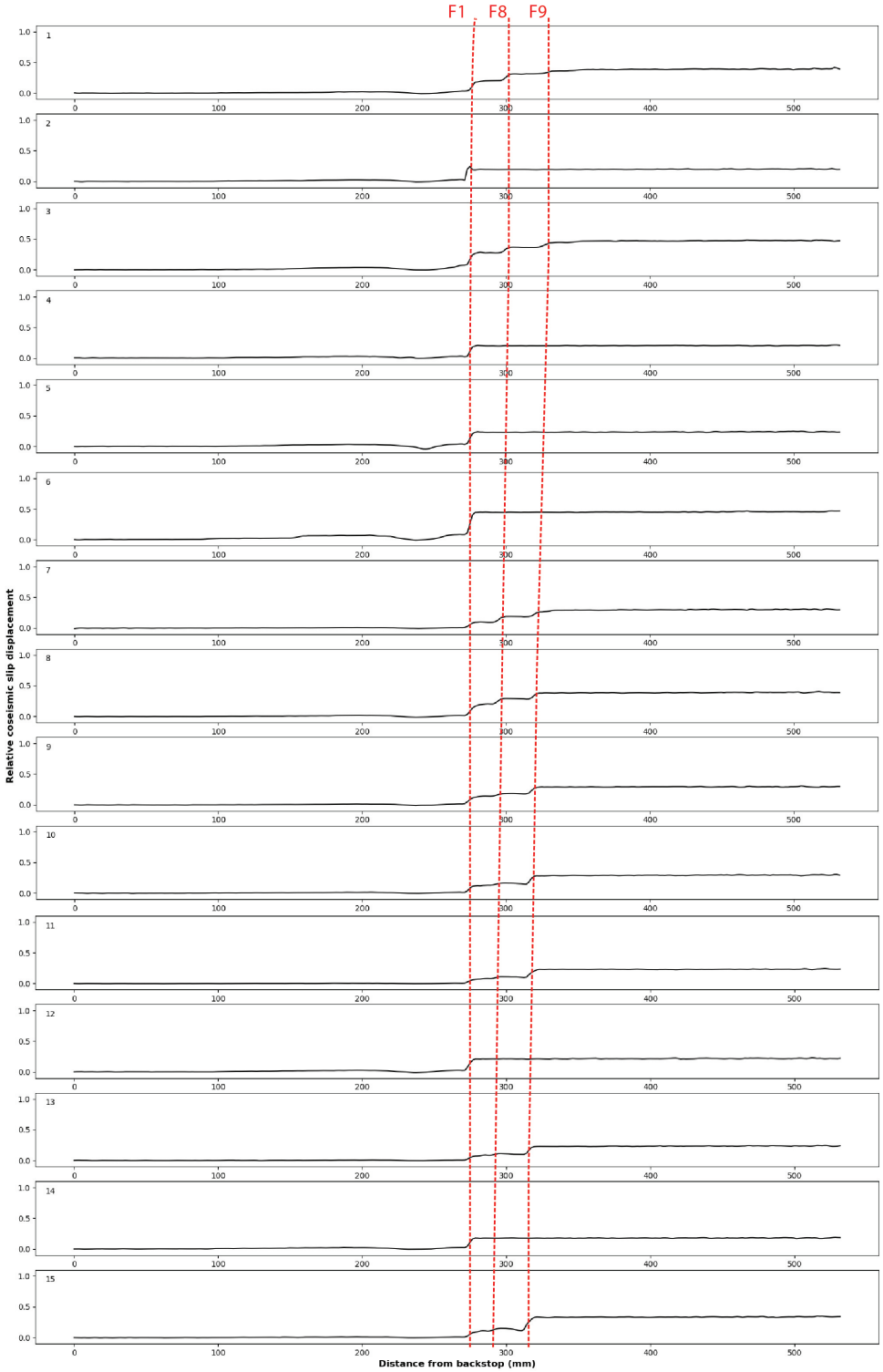

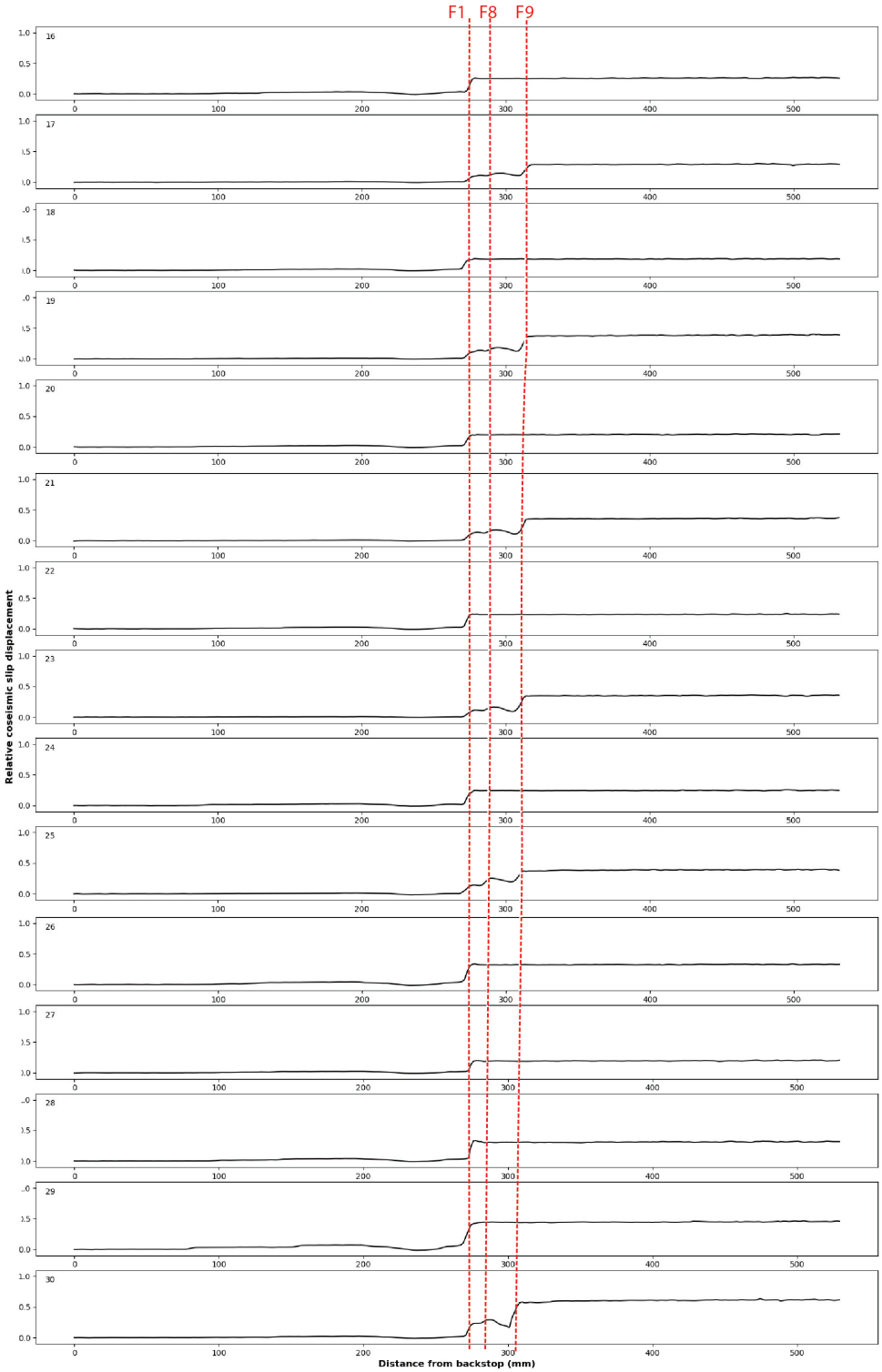
F1
F8
F9
16
17
18
19
20
21
22
23
24
25
26
27
28
29
30
Relative coseismic slip displacement
Distance from backstop (mm)

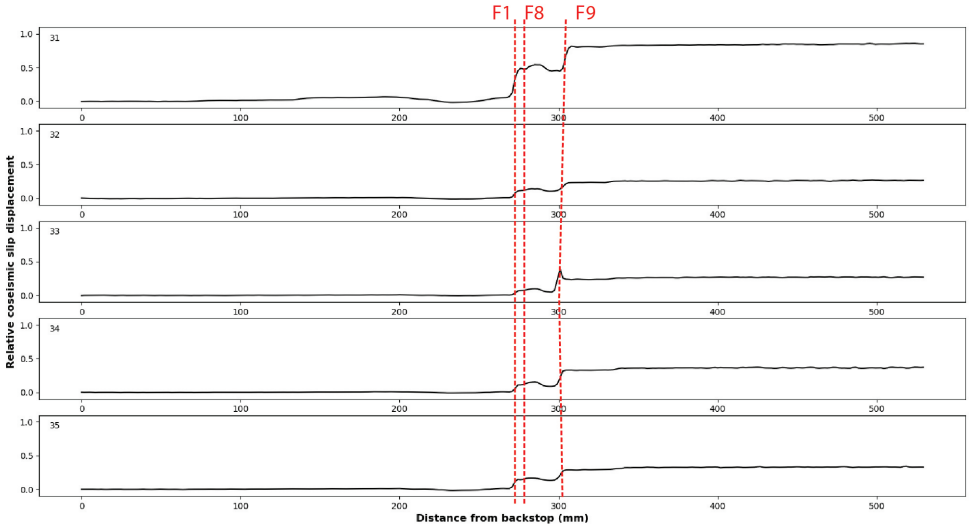

Figure 35: 1D-coseismic slip displacements for 35 individual slips in model Qtz-2. Slips are numbered (see top left of every graph). Slip displacement is relative and indicates locations of strain accumulation. Red dotted lines show the interpreted faults associated with strain localization during individual slips

H Loadcell calibration

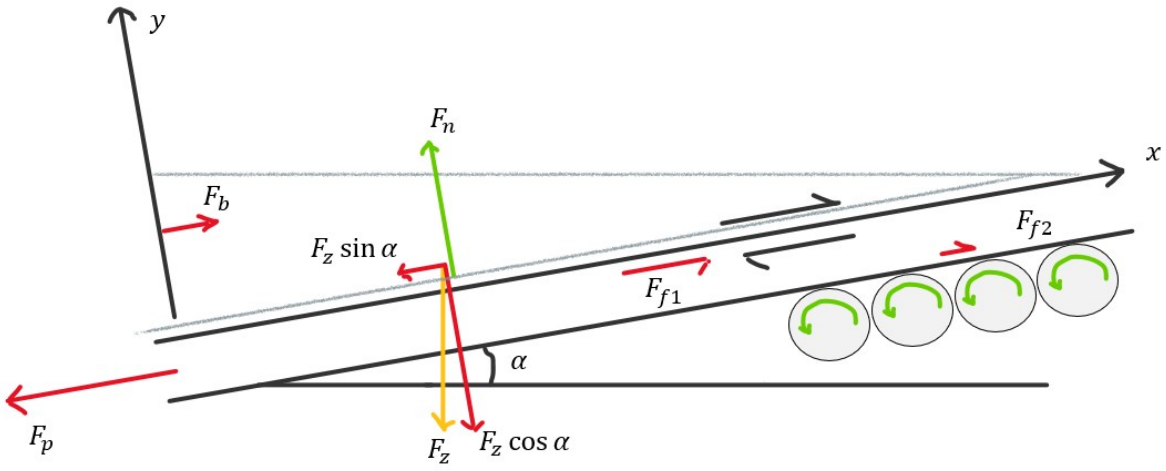

Figure 36: Forces acting in the subduction zone megathrust model.

The forces acting on the downgoing plate of the subduction zone megathrust model are shown in figure 36. Two different situations can be considered:

Situation 1: No pulling force is exerted on the downgoing plate. Gravity acts on the wedge and the downgoing plate and results in a force in the negative x-direction. Friction at the subduction interface is much larger than at the roller interface ($F_{f1} >> F_{f2}$). As a result, the wedge and the downgoing plate form one body. The backstop prevents this body from moving:

$$F_b = -F_z \sin\alpha \tag{34}$$

Situation 2: A pulling force is exerted on the downgoing plate. If we assume no acceleration (periods between slips), the sum of all forces must equal zero:

$$F_p - F_{f1} - F_{f2} - F_b + F_z \sin\alpha = 0 \tag{35}$$

Assuming $F_{f2} \approx 0$, gives:

$$F_p \approx F_{f1} \tag{36}$$

The (static) macroscopic friction coefficient is then given by:

$$\mu = \frac{F_p}{F_n} = \frac{F_p}{-F_z \cos\alpha} \tag{37}$$

Where F_z can be obtained from the material properties of the wedge and its geometry, and F_p can be obtained from the load cell (see appendix I.

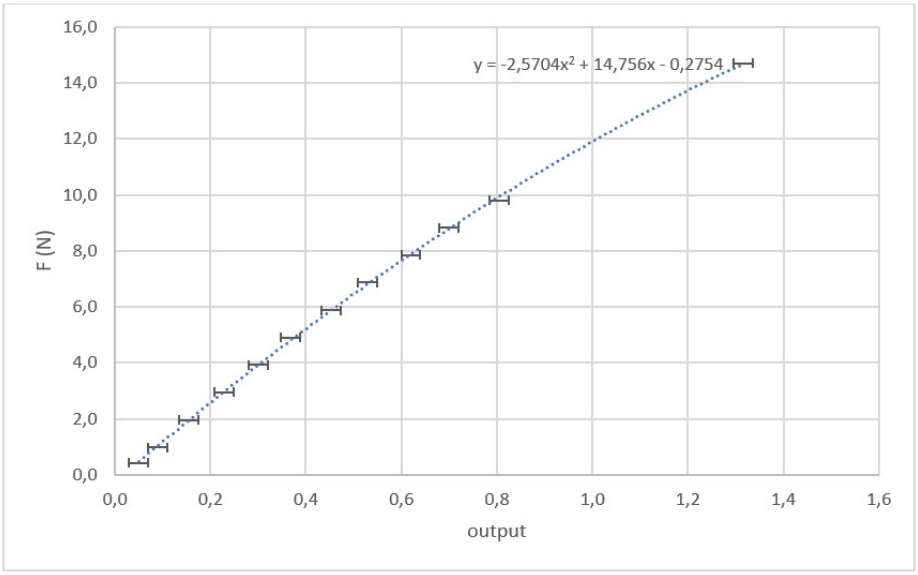

Figure 37: Calibration loadcell for non-linear fit.

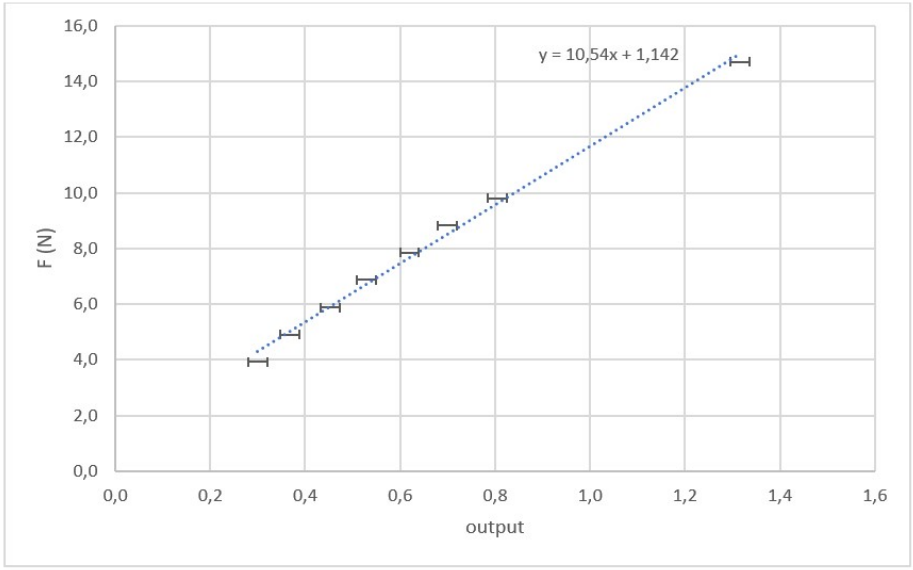

Figure 38: Calibration loadcell for linear fit. Note that values at low forces are not taken into account.

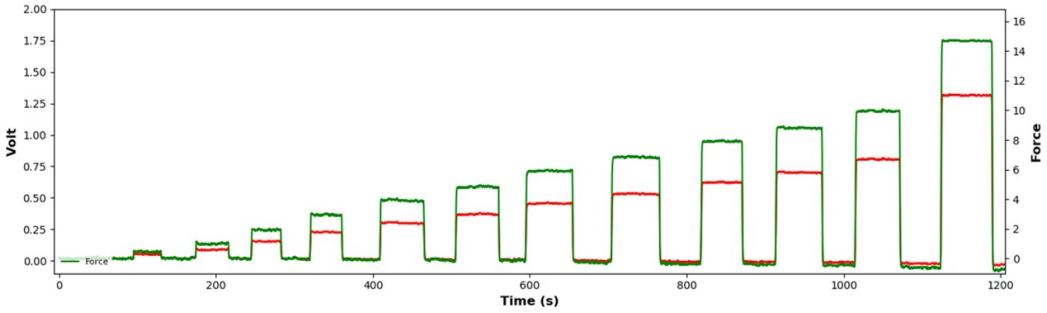

Figure 39: Calibration loadcell if a linear relation between voltage en pulling force is applied.

I Spring constant

The spring constants of different springs are calculated based on Hooke's law (1660), which states that the applied force F_p equals the change in length x, multiplied by the spring constant k:

$$F_p = kx \tag{38}$$

For spring 1 and spring 2, a range of known forces is applied and and plotted against the resulting lingth increase (see figure 23.

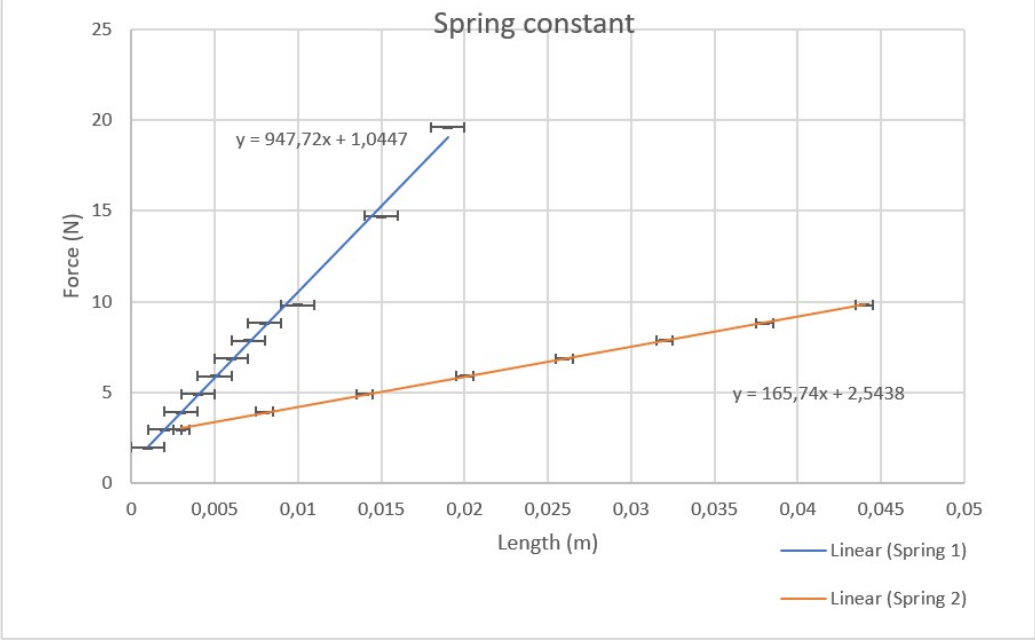

Figure 40: Calibration of spring constant for springs used in subduction zone megathrust models

The total spring constant for our model is determined by the number of springs placed in parallel and their spring constants:

$$k_{eff} = k_1 + k_2 + k_3..... \tag{39}$$

In the models of this study k_{eff} is given by:

$$k_{eff} = 1 \cdot k_1 + 4 \cdot k_2 = 1637.7 N/m \tag{40}$$

The load cell which measures the loading force, is only connected to spring 1. The total loading force can however be calculated by:

$$F_p = F_{loadcell} \cdot (k_{eff}/k_1) \tag{41}$$